Title: Heterozygous expression of a *Kcnt1* gain-of-function variant has differential effects on SST- and PV-expressing cortical GABAergic neurons.

Amy N. Shore[1,2], Keyong Li[1], Mona Safari[1,3], Alshaima'a M. Qunies[4,5], Brittany D. Spitznagel[6,7,8], C. David Weaver[6,7,8], Kyle A. Emmitte[4], Wayne N. Frankel[9,10], and Matthew C. Weston[1,2,3,11*]

[1]Fralin Biomedical Research Institute at Virginia Tech Carilion, Center for Neurobiology Research, Roanoke, VA, USA.

[2]Department of Neurological Sciences, University of Vermont, Burlington, VT, USA.

[3]Translational Biology, Medicine, and Health Graduate Program, Fralin Biomedical Research Institute at Virginia Tech Carilion, Roanoke, VA, USA.

[4]Department of Pharmaceutical Sciences, UNT System College of Pharmacy, University of North Texas Health Science Center, Fort Worth, TX, USA.

[5]School of Biomedical Sciences, University of North Texas Health Science Center, Fort Worth, TX, USA.

[6]Department of Pharmacology, Vanderbilt University, Nashville, TN, USA.

[7]Vanderbilt Institute of Chemical Biology, Vanderbilt University, Nashville, TN, USA.

[8]Department of Chemistry, Vanderbilt University, Nashville, TN, USA.

[9]Institute for Genomic Medicine, Columbia University, New York, NY, USA.

[10]Department of Neurology, Columbia University, New York, NY, USA.

[11]School of Neuroscience, Virginia Tech, Blacksburg, VA, USA.

*Lead contact and correspondence: mcweston7c@vt.edu

Conflict of interest statement: The authors declare no competing financial interests.

ABSTRACT

More than twenty recurrent missense gain-of-function (GOF) mutations have been identified in the sodium-activated potassium (K_{Na}) channel gene *KCNT1* in patients with severe developmental and epileptic encephalopathies (DEEs), most of which are resistant to current therapies. Defining the neuron types most vulnerable to KCNT1 GOF will advance our understanding of disease mechanisms and provide refined targets for precision therapy efforts. Here, we assessed the effects of heterozygous expression of a *Kcnt1* GOF variant (Y777H) on K_{Na} currents and neuronal physiology among cortical glutamatergic and GABAergic neurons in mice, including those expressing vasoactive intestinal polypeptide (VIP), somatostatin (SST), and parvalbumin (PV), to identify and model the pathogenic mechanisms of autosomal dominant *KCNT1* GOF variants in DEEs. Although the *Kcnt1*-Y777H variant had no effects on glutamatergic or VIP neuron function, it increased subthreshold K_{Na} currents in both SST and PV neurons but with opposite effects on neuronal output; SST neurons became hypoexcitable with a higher rheobase current and lower action potential (AP) firing frequency, whereas PV neurons became hyperexcitable with a lower rheobase current and higher AP firing frequency. Further neurophysiological and computational modeling experiments showed that the differential effects of the Y777H variant on SST and PV neurons are not likely due to inherent differences in these neuron types, but to an increased persistent sodium current in PV, but not SST, neurons. The Y777H variant also increased excitatory input onto, and chemical and electrical synaptic connectivity between, SST neurons. Together, these data suggest differential pathogenic mechanisms, both direct and compensatory, contribute to disease phenotypes, and provide a salient example of how a pathogenic ion channel variant can cause opposite functional effects in closely related neuron subtypes due to interactions with other ionic conductances.

Keywords: epilepsy; DEE; ADNFLE; KCNT1 channel; Slack; K_{Na} current; potassium channel; GOF variant; glutamatergic; GABAergic; SST; PV; VIP; electrophysiology

49 **INTRODUCTION**

50 Heterozygous missense variants have been identified in the sodium-gated potassium channel
51 gene *KCNT1* in more than 200 individuals exhibiting a wide spectrum of developmental and epileptic
52 encephalopathies (DEEs), with the majority being classified as either epilepsy of infancy with migrating
53 focal seizures (EIMFS) or autosomal dominant or sporadic sleep-related hypermotor epilepsy (ADSHE)
54 (Barcia et al., 2012; Bonardi et al., 2021; Heron et al., 2012). Each of these epilepsy syndromes result in
55 early-onset, frequent seizures that are largely pharmacoresistant and often accompanied by a range of
56 cognitive, psychiatric, and motor impairments. Thus, there is a critical need for a better understanding
57 of how heterozygous expression of these *KCNT1* variants in the developing brain alters neuronal
58 physiology and network behavior to lead to such devastating neurodevelopmental disorders.

59 *KCNT1* encodes a tetrameric potassium channel that is widely expressed in both glutamatergic
60 and GABAergic neurons of the brain, particularly those of the cerebellum, striatum, thalamus,
61 hippocampus, and cortex (Berg et al., 2007; Bhattacharjee et al., 2002; Gertler et al., 2022; Rizzi et al.,
62 2016). Although its precise role in normal physiology is not well understood, at least in some neuronal
63 types, KCNT1 is activated by a persistent inward sodium leak (Na_P) current at rest, where it has a
64 proposed role in fine tuning neuronal excitability by countering the effects of the Na_P current across
65 subthreshold voltages (Budelli et al., 2009; Hage & Salkoff, 2012). Consistent with this role, loss-of-
66 function (LOF) studies using mouse models lacking KCNT1, and the associated sodium-activated
67 potassium (K_{Na}) current, have shown enhanced AP firing across multiple neuron types (Evely et al., 2017;
68 Liu et al., 2022; Lu et al., 2015; Martinez-Espinosa et al., 2015; Reijntjes et al., 2019; Zhang et al., 2022).
69 Characterizations of pathogenic DEE-associated *KCNT1* variants in heterologous cells found that nearly
70 all cause gain-of-function (GOF) effects on the channel, increasing the associated K_{Na} current (Hinckley et
71 al., 2023; Kim et al., 2014; McTague et al., 2018; Milligan et al., 2014; Tang et al., 2016). Based on LOF
72 studies, this would be expected to reduce neuronal excitability; however, it is difficult to predict the

73 effects of these GOF variants on AP generation in neurons, particularly among neuronal subtypes, *a*
74 *priori*.
75 To address this knowledge gap, we previously generated and characterized a mouse model
76 expressing a human ADNFLE-associated *KCNT1* GOF variant (Y796H, or Y777H in mice) (Shore et al.,
77 2020). Although heterozygous expression of the *KCNT1*-Y796H variant is sufficient to cause severe
78 childhood epilepsy in humans, we only observed rare behavioral seizures in heterozygous *Kcnt1*-Y777H
79 mice [see Discussion-(Shore et al., 2020)]; however, we identified hyperexcitable, hypersynchronous
80 cortical networks and frequent, early-onset seizures in homozygous *Kcnt1*-Y777H mice. As a potential
81 underlying mechanism of these network alterations, we demonstrated that homozygous *Kcnt1*-Y777H
82 expression increases subthreshold K_{Na} currents and reduces excitability in GABAergic neuron
83 populations, particularly in those classified as non-fast spiking (NFS), but it does not alter glutamatergic
84 neuron excitability. We further observed evidence of homeostatic compensation and network
85 remodeling downstream of K_{Na} current increases during development, including increased excitatory
86 input onto glutamatergic and NFS GABAergic neurons, and enhanced homotypic synaptic connectivity.
87 Although these findings provide a strong mechanistic basis for understanding how KCNT1 GOF disrupts
88 neuronal physiology and network behavior to lead to seizure disorders, key issues remain unresolved.
89 First, considering the heterozygous nature of *KCNT1* GOF variants in the overwhelming majority of
90 *KCNT1*-related DEE patients, it is crucial to determine whether heterozygous *Kcnt1*-Y777H expression
91 results in similar neuronal impairments and network alterations to those with homozygous expression.
92 Second, more recent studies, using both *in silico* modeling and additional construct-valid mouse models,
93 have similarly identified impairments in GABAergic neuron excitability downstream of KCNT1 GOF
94 (Gertler et al., 2022; Kuchenbuch et al., 2021; Wu et al., 2024), indicating impaired inhibition as a shared
95 pathogenic mechanism in *KCNT1*-related DEEs; however, precisely which GABAergic subtypes are most
96 impacted, and how, remains unknown.

97 Here, we assessed the effects of heterozygous *Kcnt1*-Y777H expression on K_{Na} currents and
98 neuronal physiology among cortical glutamatergic and GABAergic neurons, including those expressing
99 vasoactive intestinal polypeptide (VIP), somatostatin (SST), and parvalbumin (PV). Initial assessments of
100 cortical neuron populations with heterozygous Y777H expression showed strikingly similar effects on K_{Na}
101 currents and AP generation to those with homozygous expression, although not surprisingly, these
102 effects were lesser in magnitude. Across all cortical neuron types examined, the heterozygous *Kcnt1*-
103 Y777H variant caused a range of effects on neuronal excitability and action potential (AP) generation,
104 from no change (glutamatergic and VIP GABAergic) to decreased excitability (SST GABAergic) to
105 increased excitability (PV GABAergic). Neuron types that showed no change had K_{Na} currents that were
106 only significantly increased at suprathreshold voltages and exhibited a steeper voltage dependence of
107 activation. Interestingly, both SST and PV neurons showed similar increases in K_{Na} currents across
108 subthreshold voltages, however, only PV neurons had additional increases in the persistent Na^+ current,
109 which modeling experiments indicated was sufficient to overcome the effects of KCNT1 GOF and cause
110 an overall increase in AP generation. SST neurons also showed an increase in excitatory input, and in
111 homotypic electrical and chemical coupling. Taken together, these data provide further evidence of the
112 enhanced vulnerability of GABAergic neurons, particularly those expressing SST and PV, to KCNT1 GOF.
113 Moreover, these data show that heterozygous expression of a single *KCNT1* GOF variant can result in a
114 complex array of neuron type-dependent effects, both direct and indirect, each potential contributors to
115 the neural circuit pathology underlying *KCNT1*-related DEEs.
116
117 **RESULTS**
118 **Heterozygous *Kcnt1*-Y777H expression alters the shape and frequency of APs in NFS GABAergic**
119 **neurons.**

120 We previously identified frequent, early-onset seizures in mice with homozygous expression of
121 the *Kcnt1* GOF variant Y777H (hereafter referred to as YH-HOM), and as a potential underlying
122 pathological mechanism, we demonstrated that homozygous *Kcnt1*-Y777H expression drastically impairs
123 action potential (AP) shape and generation in non-fast spiking (NFS) GABAergic cortical neurons, with
124 lesser effects on fast spiking (FS) GABAergic, and no significant effects on glutamatergic, cortical neurons
125 (Shore et al., 2020). Considering that patients with *KCNT1*-associated epilepsy are predominantly
126 heterozygous for *KCNT1* GOF variants, it is crucial to determine whether heterozygous expression of
127 these variants, which likely leads to the formation of heteromeric channels consisting of WT and mutant
128 subunits, results in similar neuronal impairments. To assess neuron subtype-specific effects of
129 heterozygous KCNT1 GOF on membrane properties and AP firing, we isolated and cultured cortical
130 neurons from pups with heterozygous Kcnt1-Y777H expression (hereafter referred to as YH-HET), and
131 their WT littermates, at postnatal day 0 (P0). After infecting the cultured neurons with AAV-*CaMKII*-GFP
132 to facilitate glutamatergic neuron identification, we performed whole-cell, current-clamp analysis
133 between 13 and 17 days *in vitro* (DIV). Moreover, to compare to homozygous KCNT1 GOF effects
134 observed previously, the recorded neurons were classified as glutamatergic, FS GABAergic, or NFS
135 GABAergic, based on GFP expression, AP parameters, and evoked synaptic responses (see Methods).
136 Current-clamp recordings from YH-HET and WT glutamatergic neurons showed no significant
137 differences in any membrane or AP shape property measured (Fig. $1A_1$ and Supplemental Table 1),
138 similar to observations from the homozygous KCNT1 GOF studies. Accordingly, AP firing frequencies
139 across increasing current steps in YH-HET glutamatergic neurons were not altered compared with those
140 of WT (Fig. $1B_1$). For FS GABAergic neurons, we previously showed that homozygous Y777H expression
141 increases the rheobase—the minimal amount of current necessary to induce an AP—and reduces the AP
142 firing frequency. Heterozygous Y777H expression did not alter the rheobase, or any other passive or
143 active membrane property of FS GABAergic neurons (Fig. $1A_2$ and Supplemental Table 1). Although YH-

144 HET FS GABAergic neurons appeared to fire fewer APs than their WT counterparts, particularly at higher
145 current steps, this effect was not significant (Fig. $1B_2$). Lastly, we previously showed that homozygous
146 Y777H expression has the strongest effects in NFS GABAergic neurons, showing a decrease in input
147 resistance, accompanied by an increase in rheobase and a reduction in AP firing frequency. YH-HOM NFS
148 GABAergic neurons also have narrower AP half-widths and larger afterhyperpolarizations (AHPs) than
149 those of WT. Although heterozygous Y777H expression in NFS GABAergic neurons did not cause a
150 significant decrease in input resistance (WT: 171 ± 16; YH-HET: 146 ± 14, p=0.19), it did increase the
151 rheobase and reduce the AP firing frequency, particularly at lower current steps, relative to those of WT
152 (Fig. $1A_3$ and $1B_3$). YH-HET NFS GABAergic neurons also had narrower APs, larger AHPs, and more
153 depolarized AP thresholds than those of WT (Supplemental Table 1). Together, these data demonstrate
154 that the neurophysiological effects on cortical neurons with monoallelic expression of the *Kcnt1*-Y777H
155 variant, expressing channels with mutant and WT subunits, are similar to those with biallelic expression,
156 expressing only mutant subunits, with both causing the strongest impairments in NFS GABAergic
157 neurons.
158
159 **Heterozygous *Kcnt1*-Y777H expression increases subthreshold K_{Na} currents in NFS GABAergic neurons.**
160 Previously, we showed that homozygous *Kcnt1*-Y777H expression in GABAergic cortical neurons
161 increases the K_{Na} current across subthreshold voltages, an effect that is particularly evident in NFS
162 GABAergic neurons; conversely, in glutamatergic cortical neurons with homozygous expression of the
163 same variant, increases in K_{Na} currents are only apparent at depolarized voltages (> +30 mV) (Shore et al.,
164 2020). To assess the effects of heterozygous Y777H expression on KCNT1 channel function, we
165 measured the associated K_{Na} current in each cortical neuron subtype. We recorded K_{Na} currents by
166 applying voltage steps to voltage-clamped neurons and comparing the delayed outward current before
167 and after the addition of the voltage-gated sodium channel inhibitor TTX (Fig. $2A_{1\text{-}3}$). As reported

168 previously, there were K_{Na} currents in all three WT neuron subtypes, beginning around -10 mV and
169 increasing with depolarization (Fig. $2A_{1-3}$ and $2B_{1-3}$), whereas at more negative potentials, the TTX-
170 sensitive current was net inward (Fig. $2C_{1-3}$) due to the counteracting persistent Na^+ current.
171 In glutamatergic and NFS GABAergic YH-HET neurons, the overall K_{Na} current was increased
172 relative to those of WT, as measured by a significant effect of genotype using a linear model (Fig. $2B_{1,3}$).
173 Importantly, in each of these neuron subtypes, heterozygous Y777H expression increased K_{Na} currents
174 with distinct, voltage-dependent patterns that appeared strikingly similar to those reported with
175 homozygous expression. For instance, we previously showed that, across negative potentials, YH-HOM
176 and WT glutamatergic neuron K_{Na} currents are indistinguishable, whereas at more positive potentials (>
177 +30 mV), the Y777H variant causes significant increases in K_{Na} currents. Similar voltage-dependent
178 effects were observed in YH-HET glutamatergic neurons (Fig. $2B_1$ and $2C_1$), although pairwise
179 comparisons showed that K_{Na} current increases at positive potentials in the YH-HET glutamatergic
180 neurons were not significant. Conversely, we previously demonstrated broad increases in K_{Na} currents
181 across negative potentials, with significant increases from -60 to +10 mV, in YH-HOM NFS GABAergic
182 neurons compared with those of WT, with lesser effects across positive potentials. Similar voltage-
183 dependent increases were observed in YH-HET NFS GABAergic neurons, with pairwise comparisons
184 showing significant K_{Na} current increases at -70, -60, -50, and -20 mV (Fig. $2B_3$ and $2C_3$). For both
185 glutamatergic and NFS GABAergic neurons, the magnitudes of the K_{Na} current increases in YH-HET
186 neurons were intermediate to those of WT and YH-HOM neurons (Supplemental Fig. 2-1),
187 demonstrating a gene dose-dependent effect of the *Kcnt1*-Y777H variant on K_{Na} current increases and
188 validating a GOF effect of the heterozygous Y777H variant on channel function. Lastly, although previous
189 studies showed that homozygous Y777H expression increases K_{Na} current at several negative voltage
190 steps (-50, -40, and -10 mV) in FS GABAergic neurons, heterozygous expression of the same variant in FS

191 GABAergic neurons caused no significant differences in K_{Na} currents compared with those of WT (Fig. $2B_2$
192 and $2C_2$).
193
194 **Heterozygous *Kcnt1*-Y777H expression does not alter synaptic connectivity or the excitation-inhibition**
195 **balance.**
196 In addition to alterations in the intrinsic passive and active membrane properties of cortical
197 neurons with homozygous Y777H expression, we previously showed evidence of altered synaptic
198 connectivity and activity, leading to hypersynchronous, hyperexcitable YH-HOM networks; more
199 specifically, we found an increase in homotypic coupling between glutamatergic [excitatory–excitatory
200 (E–E)] and GABAergic [inhibitory–inhibitory (I–I)] neuron pairs, and an increase in the frequency of
201 spontaneous excitatory postsynaptic currents (sEPSCs), accompanied by an increase in the E/I ratio,
202 onto YH-HOM glutamatergic cortical neurons (Shore et al., 2020). First, to determine whether there are
203 similar changes in synaptic connectivity in YH-HET networks, we performed paired recordings of
204 glutamatergic (excitatory, E) and GABAergic (inhibitory, I) neurons and alternatively stimulated each
205 neuron at 0.1 Hz to test baseline connection probability and strength at the four possible motifs (E–E, I–
206 E, E–I, and I–I). Connection probability was not altered in YH-HET networks at any of the motifs tested
207 (Fig. $3A_{1\text{-}4}$, left bar graphs), and the amplitudes of the evoked postsynaptic currents (ePSCs) between
208 connected neurons were not different between genotypes for any of the four connection types (Fig. $3A_{1\text{-}}$
209 $_{4}$, right bar graphs), indicating grossly normal synaptic interactions among glutamatergic and GABAergic
210 neurons in YH-HET networks. Next, to assess potential alterations in synaptic activity, we recorded
211 spontaneous postsynaptic currents (sEPSCs and sIPSCs) onto voltage-clamped glutamatergic and
212 GABAergic neurons. Unlike the observation of an increase in sEPSC frequency onto YH-HOM
213 glutamatergic neurons, there was no difference in sEPSC, or sIPSC, frequency onto YH-HET glutamatergic
214 neurons (Fig. $3B_1$). Furthermore, although we previously found no alterations in sPSC frequency onto

215 YH-HOM GABAergic neurons, sEPSC and sIPSC frequencies were both slightly reduced onto YH-HET
216 GABAergic neurons (Fig. $3B_2$). Finally, to assess the net effect of altered sPSC activity onto YH-HET
217 neurons, we calculated the E/I ratio, based on the relative frequency and size of the sPSCs, and found no
218 difference in the E/I ratio onto either YH-HET neuron type (Fig. $3B_3$). Thus, although heterozygous Y777H
219 expression resulted in similar K_{Na} current increases and neuronal physiology effects to those found with
220 homozygous Y777H expression, the broad effects on synaptic connectivity and activity found in YH-HOM
221 networks were absent in YH-HET networks, which likely results in the observed reduction in seizure
222 incidence in heterozygous, relative to homozygous, mice.
223
224 **Heterozygous *Kcnt1*-Y777H expression differentially affects the intrinsic excitability of SST- and PV-**
225 **expressing GABAergic neurons.**
226 Next, we sought to determine which GABAergic subtypes are most impacted by heterozygous
227 Kcnt1-Y777H expression. About 80–90% of cortical GABAergic neurons fall into three, largely non-
228 overlapping populations that can be identified by their expression of unique markers: the Ca^{2+}-binding
229 protein parvalbumin (PV; ~40%) and the neuropeptides somatostatin (SST; ~30%) and vasoactive
230 intestinal polypeptide (VIP; ~15%) (Rudy et al., 2011; Tremblay et al., 2016). The majority of PV-
231 expressing neurons have been characterized as FS, and VIP-expressing as NFS, whereas SST-expressing
232 neurons, although largely thought to show NFS firing properties, also contain a population that exhibits
233 a FS-like phenotype (Large et al., 2016; Ma et al., 2006). *KCNT1* is expressed at higher levels in both
234 human and mouse cortical GABAergic neurons expressing PV and SST, than in those expressing VIP
235 (Gertler et al., 2022; Shore et al., 2020). Based on the expression profile of KCNT1, and our findings that
236 homozygous and heterozygous expression of the *Kcnt1* GOF variant strongly reduced the excitability
237 GABAergic neurons with NFS firing properties, we hypothesized that the SST-expressing neurons are the
238 most vulnerable to the effects of KCNT1 GOF. To test this hypothesis, we crossed PV-, SST-, and VIP-Cre

239 mouse lines to the *Kcnt1*-Y777H mouse line and cultured neurons from the cortices of WT and YH-HET
240 littermate progeny (Fig. 4A and Supplemental Fig. 4-1A). We infected the cultured neurons with AAV-
241 *CaMKII*-GFP, to mark glutamatergic neurons, and AAV-*hSyn*-DIO-mCherry, to mark Cre recombinase-
242 expressing GABAergic neurons, and performed whole-cell, patch-clamp electrophysiology at DIV 13–17
243 on GFP^-/$mCherry^+$ neurons from each group.

244 First, we measured the intrinsic membrane properties and AP shape parameters of the three
245 GABAergic subtypes from the WT control groups to verify that they accurately reflected
246 electrophysiological behaviors of these subtypes from previous *ex vivo* recordings (Taniguchi et al.,
247 2011). As expected, the VIP neurons showed a relatively large input resistance, small rheobase, wide AP
248 half-width, small AHP, and low firing rate (Supplemental Fig. 4-1B and 4-1C, purple); in contrast, PV
249 neurons showed a small input resistance, large rheobase, narrow AP half-width, large AHP, and high
250 firing rate (Supplemental Fig. 4-1B and 4-1C, orange). For SST neurons, the values measured for input
251 resistance, rheobase, AP half-width, AHP, and firing rate were all intermediate to those of VIP and PV
252 neurons (Supplemental Fig. 4-1B and 4-1C, blue). Moreover, as reported previously, SST neurons
253 showed the most hyperpolarized AP threshold of the three groups. Together, these data demonstrate
254 the ability of cortical GABAergic neuron subtypes to retain their characteristic *ex vivo* passive and active
255 membrane properties *in vitro*.

256 Next, we assessed the effects of the Y777H variant on the passive and active membrane
257 properties of each GABAergic subtype. Current-clamp recordings from YH-HET VIP neurons revealed no
258 significant effect of the variant on any of the membrane or AP properties measured (Fig. $4B_1$).
259 Conversely, YH-HET SST neurons showed a strong decrease in input resistance, with an accompanying
260 increase in rheobase current, relative to those of WT SST neurons (Fig. $4B_2$), similar to the hypoexcitable
261 membrane phenotype observed in the YH-HET NFS neurons, without altering AP shape parameters. YH-
262 HET SST neurons also showed a reduction in the membrane time constant and an increase in membrane

263 capacitance, which was accompanied by an increase in soma size (Supplemental Table 4 and
264 Supplemental Fig. 4-2), compared with those of WT SST neurons. Unexpectedly, YH-HET PV neurons
265 exhibited a decrease in the rheobase current compared with that of WT (Fig. $4B_3$), and an increase in AP
266 amplitude (Supplemental Table 4), suggesting the Y777H variant increases PV neuron excitability.
267 Next, we measured AP firing frequency with incremental, 500-ms current steps in each of the
268 three GABAergic subtypes. WT neurons showed AP firing frequencies similar to those reported
269 previously from *ex vivo* recordings of neurons from the three Cre lines (Taniguchi et al., 2011), with VIP
270 showing the lowest maximal firing frequency, PV the highest, and SST intermediate between VIP and PV
271 (Fig. $4C_{1\text{-}3}$ and Supplemental Table 4). Consistent with a lack of any effects on membrane and AP shape
272 properties, the AP firing frequencies across increasing current steps were indistinguishable between WT
273 and YH-HET VIP neurons (Fig. $4C_1$). As expected, based on their hypoexcitable membrane properties, the
274 YH-HET SST neurons fired fewer APs across all current steps relative to WT SST neurons (Fig. $4C_2$). In
275 contrast to SST neurons, but consistent with their decreased rheobase current, YH-HET PV neurons fired
276 more APs across all current steps relative to their WT counterparts (Fig. $4C_3$). Notably, although these
277 experiments were performed at room temperature (~22°C), and increasing temperatures to 35°C
278 altered multiple neuronal physiology parameters (Supplemental Fig. 4-3A), both WT and YH-HET PV
279 neurons responded similarly to increased temperature (Supplemental Fig. 4-3B), suggesting that the
280 observed phenotypes are not temperature dependent. Together, these data showed that, as
281 hypothesized, KCNT1 GOF indeed strongly reduces the excitability of SST neurons, but unexpectedly, it
282 also causes a hyperexcitable effect in PV neurons; thus, the same ion channel mutation can lead to
283 opposite effects on excitability in the two largest GABAergic neuron subtypes.
284
285 **The Y777H variant increases KCNT1-mediated currents across subthreshold voltages in SST- and PV-**
286 **expressing GABAergic neurons.**

287 Are the observed differential effects of KCNT1 GOF on GABAergic neuronal physiology due to
288 distinct patterns of K_{Na} current increases among GABAergic neuron subtypes? To answer this question,
289 we first recorded K_{Na} currents from GABAergic neurons cultured and labeled as described above, by
290 applying voltage steps to voltage-clamped neurons and comparing the delayed outward current before
291 and after the addition of TTX (Supplemental Fig. 5-1A_{1-3}). In all three subtypes, for both WT and YH-HET
292 neurons, we observed K_{Na} currents beginning around -10 mV and increasing with depolarization
293 (Supplemental Fig. 5-1B_{1-3}). For YH-HET VIP neurons, pairwise comparisons to assess voltage-dependent
294 differences showed that their K_{Na} currents were not different from those of WT at any voltage step
295 (Supplemental Fig. 5-1B_1 and 5-1C_1). On the other hand, YH-HET SST neurons showed significant
296 increases in K_{Na} currents compared with those of WT across multiple subthreshold voltage steps,
297 including -60, -50, and -40 mV (Supplemental Fig. 5-1B_2 and 5-1C_2), similar to those observed in NFS
298 GABAergic neurons with both heterozygous (Fig. 2) and homozygous expression of the Y777H variant
299 (Shore et al., 2020), indicating a direct current-to-phenotype relationship in YH-HET SST neurons.
300 Somewhat unexpectedly, pairwise comparisons showed that K_{Na} currents were not different between
301 YH-HET and WT PV neurons at any voltage step (Supplemental Fig. 5-1B_3 and 5-1C_3).
302 The lack of an increase in TTX-sensitive currents in PV neurons, despite alterations in rheobase,
303 AP amplitude, and AP firing frequency, suggests that either a TTX-insensitive Na^+ source activates KCNT1,
304 or that compensatory alterations in an opposing current mask an increase in K_{Na} and lead to the changes
305 in AP firing. In past studies, the lack of selective KCNT1-specific inhibitors necessitated the use of indirect
306 methods, such as TTX application or Na^+ replacement, to estimate the magnitude of K_{Na}. However, more
307 recently, we identified and validated a small-molecule, selective KCNT1 channel inhibitor termed
308 VU0606170, or VU170 (Spitznagel et al., 2020). To further validate the specificity of this small molecule,
309 we applied voltage steps to voltage-clamped neurons lacking KCNT1 and KCNT2 channels, isolated and
310 cultured from *Kcnt1*$^{-/-}$; *Kcnt2*$^{-/-}$ double knockout mice (Martinez-Espinosa et al., 2015), and we compared

311 the delayed outward current before and after the addition of either 10 µM VU170 or 0.5 µM TTX. This
312 analysis indicated a non-specific outward VU-sensitive current that started around -10 mV and peaked
313 at +50 mV (~1 nA peak current compared with ~3 nA in WT neurons), which was not present using TTX
314 subtraction (Supplemental Fig. 5-2A). Across negative potentials, there was an inward TTX-sensitive
315 current, which again is likely due to the persistent Na^+ current, whereas there was little to no outward
316 VU-sensitive current (Supplemental Fig. 5-2B), validating the utility of VU170 in isolating K_{Na} currents
317 across this voltage range.

318 To better assess KCNT1-mediated currents in GABAergic subpopulations and disentangle
319 potential confounds of using TTX, particularly across negative potentials, we applied the same voltage
320 step protocol as in the TTX subtraction experiments but applied 10 µM VU170 instead. In all three WT
321 GABAergic neuron subtypes, subtraction of the VU170 trace from the control trace revealed nA-sized
322 outward currents at depolarized potentials, and in YH-HET neurons, the overall VU170-sensitive current
323 was increased relative to those of WT, as measured by a significant effect of genotype using a linear
324 model (Fig. $5A_{1-3}$ and $5B_{1-3}$). Pairwise comparisons at each voltage step showed voltage-dependent
325 differences in current increases among the YH-HET neuron subtypes. For YH-HET VIP neurons, a
326 significant increase in the VU170 current was only observed at +50 mV (Fig. $5B_1$), whereas subthreshold
327 currents were indistinguishable from those of WT (Fig. $5C_1$). Previously, we similarly observed K_{Na}
328 current increases only at more positive potentials in YH-HOM glutamatergic neurons, and like YH-HET
329 VIP neurons, their membrane and AP properties were unaltered by expression of the YH variant (Shore
330 et al., 2020). Conversely, in YH-HET SST neurons, significant increases occurred at more negative voltage
331 steps, from -60 to -30 mV (Fig. $5C_2$). These changes were similar to those observed with TTX treatment,
332 but slightly larger, possibly due to the lack of the counteracting effect of the persistent Na^+ current,
333 which is also blocked by TTX. In contrast to the TTX results, YH-HET PV neurons showed an increase in
334 VU170-sensitive currents, with significant increases from -70 to -50 mV (Fig. $5C_3$). Taken together, these

335 data identify distinct patterns of K_{Na} current increases among GABAergic subtypes, and for VIP and SST
336 neurons, these current increases are consistent with the observed effects of KCNT1 GOF on neuronal
337 physiology. On the other hand, PV neurons showed subthreshold-specific K_{Na} current increases that
338 were highly similar to, and overlapping with, those of SST neurons; thus, differential K_{Na} current
339 increases alone likely do not account for the opposite effects of KCNT1 GOF on physiology observed in
340 these two neuron types.
341
342 **Compartmental models of KCNT1 GOF in SST, but not PV, neurons are consistent with experimental**
343 **data.**
344 The VU170-subtraction experiments showed that YH-HET SST and PV neurons have similar
345 subthreshold increases in KCNT1-mediated currents, even though they exhibited opposing effects on
346 neuron excitability and AP generation, and that YH-HET VIP neurons have suprathreshold increases in
347 KCNT1-mediated currents with no effects on neuron physiology. Because GABAergic subtypes exhibit
348 varying morphologies and express unique repertoires of ion channels, which are known to give rise to
349 their characteristic membrane and AP firing properties, we hypothesized that at least some of the
350 observed differential effects of KCNT1 GOF, in particular the opposite effects in SST and PV neurons, are
351 due to these inherent, neuron-type-dependent differences. To test this hypothesis, we simulated the
352 effect of KCNT1 GOF in compartmental models of these three cortical neuron types. We used a KCNT1
353 conductance with the Na^+ dependence constrained by prior studies in neurons (EC_{50} = 40 mM, slope 3.5;
354 see Materials and Methods) and the voltage dependence based on the activation curves from our own
355 experimental data of the VU170-sensitive current in each subtype (Fig. 6A). The kinetics of the model
356 current were set by measuring the onset time course of the VU170-sensitive current in outside-out
357 membrane patches of each neuron type (Fig. 6B and 6C). This conductance was inserted into
358 compartmental models of 10 neurons per subtype, representing a variety of morphological and

359 electrical properties of each subtype (Markram et al., 2015). Because the Y796H variant was previously
360 shown to increase the Na^+ sensitivity of the channel, we modeled the GOF effect by reducing the EC_{50} for
361 Na^+ activation to two levels (35 mM and 30 mM), which resulted in moderate K_{Na} current increases
362 above WT levels (Fig. 6D).

363 Consistent with our experimental data, introducing KCNT1 GOF at the lower level (EC_{50} = 35 mM)
364 into model VIP neurons did not alter their AP firing rate, input resistance, or rheobase, whereas at the
365 higher level (EC_{50} = 30 mM), there were small changes in input resistance (40 mM: 266.5 ± 28.2; 30 mM:
366 264.8 ± 28.0, p=0.012) and rheobase (40 mM: 78.7 ± 11.6; 30 mM: 80.4 ± 11.1, p=0.014), but these
367 changes were not sufficient to affect the AP firing rate (Fig. $6E_1$ and $6E_2$, Supplemental Table 6, and
368 Supplemental Fig. 6-2A). On the other hand, model SST neurons with KCNT1 GOF at both levels fired
369 fewer APs per current step as the GOF was increased, and showed significantly reduced input
370 resistances, higher rheobases, and lower AP firing rates (Fig. $6F_1$ and $6F_2$, Supplemental Table 6), results
371 that agree with our experimental observations. In contrast to experimental data, but similar to model
372 SST neurons, model PV neurons responded to KCNT1 GOF with decreased input resistance, increased
373 rheobase, and a reduced AP firing rate (Fig. $6G_1$ and $6G_2$ and Supplemental Table 6), although the
374 magnitude of these effects were smaller than those in model SST neurons (Supplemental Fig. 6-2A).
375 These data suggest that the increased excitability observed in YH-HET PV neurons is not simply due to an
376 intrinsic property of this GABAergic subtype, but instead results from an indirect mechanism (e.g. a
377 compensatory response like an increase in Na^+ channels) or depends on a feature of KCNT1 function not
378 captured by the model.

379 Lastly, we hypothesized that the lack of GOF effects on VIP and glutamatergic neuron physiology
380 is due to the altered kinetics of their KCNT1 channel activation curves, in particular their right shifted V_{50}
381 and decreased slope, relative to those of SST or PV neurons (Fig. 6A). To test this hypothesis, we
382 performed simulations in which the activation curve parameters (V_{50} and slope) measured in SST

383 neurons were inserted into VIP and glutamatergic neurons, with the Na^+ EC_{50} set to 30 mM to simulate
384 KCNT1 GOF (Supplemental Fig. 6-1A_1 and 6-1B_1, blue traces). Inserting KCNT1 channels with SST kinetics
385 into VIP and glutamatergic neurons indeed enhanced the GOF effects on input resistance and rheobase,
386 and importantly, resulted in a significantly decreased AP firing rate relative to control neurons for both
387 neuron types (Supplemental Fig. 6-1A_2 and 6-1B_2, Supplemental Table 6, and Supplemental Fig. 6-2B).
388 This model-based evidence suggests that the relative sensitivity of SST and PV neurons, and resistance of
389 VIP and glutamatergic neurons, to KCNT1 GOF is due to the differences in voltage dependence of the K_{Na}
390 current in each subtype.
391
392 **The persistent Na^+ current is increased by the *Kcnt1*-Y777H variant in PV, but not SST, neurons.**
393 The modeling results suggest that a subthreshold increase in the K_{Na} current alone is not
394 sufficient to account for the alterations in PV neuron excitability. Moreover, the finding of an increase in
395 the KCNT1-mediated current in YH-HET PV neurons when measured with VU170, but not TTX, isolation
396 suggests there may be a compensatory upregulation of an opposing current that masks the increase in
397 K_{Na} and leads to the unexplained increase in AP firing. The persistent Na^+ current (I_{NaP}) is active on the
398 same time scale as K_{Na} and was previously shown to provide the Na^+ source for K_{Na} (Hage & Salkoff,
399 2012); therefore, we hypothesized that KCNT1 GOF causes an increase in I_{NaP} in PV neurons that
400 enhances their excitability. To test this hypothesis, we measured I_{NaP} in SST and PV neurons by applying
401 TTX during slow voltage ramp protocols (20 mV/s) designed to isolate I_{NaP} from both the transient Na^+
402 current and the K_{Na} current (Supplemental Fig. 7-1).
403 In SST neurons, I_{NaP} did not differ between WT and YH-HET neurons, either in the shape of the
404 response (Fig. 7A and 7B), or the peak amplitude (Fig. 7B). In PV neurons, however, the peak amplitude
405 of I_{NaP} was significantly increased by the Y777H variant (Fig. 7C and 7D). To examine whether this
406 increase in I_{NaP} could account for the increase in AP firing observed in PV neurons, we again simulated

407 the effect of KCNT1 GOF (Na^+ EC_{50} = 35 mM) on PV neuron activity, but this time included an increase in
408 I_{NaP} in the compartmental models. Indeed, an increase in I_{NaP} conductance, similar to what was seen in
409 the experimental results (2-fold), was sufficient to increase the number of APs fired in response to
410 increasing current steps (Fig. 7E and 7F and Supplemental Table 6), even in the face of the higher level of
411 KCNT1 GOF (30 mM; Supplemental Table 6 and Supplemental Fig. 7-2). Also, like the experimental data,
412 the rheobase current was decreased (Fig. 7F and Supplemental Fig. 7-2) and the AP height was increased
413 (80.4 ± 0.7 vs. 82.1 ± 0.8 mV). These results suggest that the differential effects on AP firing in SST and
414 PV neurons can be accounted for by the absence or presence of a secondary increase in I_{NaP}.
415
416 **YH-HET SST neurons show increased chemical and electrical coupling and receive increased excitatory**
417 **input.**
418 We previously showed that homozygous expression of the Y777H variant increased connections
419 between GABAergic neurons (Shore et al., 2020), but heterozygous expression did not (Fig. 3). Because
420 heterozygous Y777H variant expression caused the strongest excitability impairments in SST neurons,
421 we hypothesized that alterations in synaptic connectivity and activity may be more likely to occur in this
422 neuronal population. To test this hypothesis, we recorded from pairs of WT or YH-HET SST neurons as
423 described above to measure connection probability and strength. Indeed, similar to the increase
424 observed in I–I connections in YH-HOM networks, we found an increase in homotypic synaptic
425 connections of SST neurons in YH-HET networks (30/40 connections) relative to those in WT (15/40
426 connections; Fig. 8A). The amplitudes of the evoked postsynaptic currents (ePSCs) between connected
427 SST neurons were not significantly different between the YH-HET and WT groups (Fig. 8B).
428 There are two main types of synaptic coupling between neurons: chemical, which is mediated by
429 neurotransmitter release, and electrical, which is mediated by gap junctions. To test for alterations in
430 each type of synaptic coupling due to expression of the *Kcnt1* variant, we recorded from 20 pairs of WT

431 or YH-HET SST neurons in close proximity (< 100 µm apart). Under current-clamp conditions, we injected
432 a series of hyperpolarizing and depolarizing current steps into one neuron and assessed whether the
433 current induced a simultaneous voltage deflection in the paired, non-injected neuron (Fig.8C_1; 100-pA-
434 evoked response). We then evoked a train of APs in one neuron and assessed the AP-induced voltage
435 changes in the paired, non-injected neuron (Fig. 8C_1; AP-evoked response). SST pairs were considered to
436 be chemically coupled if the AP trains in one neuron induced corresponding IPSCs, without inducing
437 voltage deflections in response to the current steps, onto the paired neuron (Fig. 8C_1; top panels). SST
438 pairs were considered to be electrically coupled if the current steps injected into one neuron induced
439 simultaneous voltage deflections in the paired neuron (Fig. 8C_1; bottom panel, left). Electrically coupled
440 SST neurons also frequently showed AP-evoked spikelets onto paired neurons due to low-pass filtering
441 (Fig. 8C_1; bottom panel, right), which results in a greater attenuation of the high frequency portion
442 (spike), than the low frequency portion (AHP), of an action potential as it passes through an electrical
443 synapse.

444 Of the 20 WT SST neuron pairs tested, 12 were coupled, and the majority (9/12) of those were
445 one-way chemical connections (Fig. 8C_2). Of the 20 YH-HET SST neuron pairs tested, 17 were coupled,
446 and the majority (13/17) of those were two-way, or bidirectionally, connected (Fig. 8C_2). Of the 3
447 bidirectionally connected WT SST neuron pairs, 2 were chemical and 1 was electrical, whereas of the 13
448 bidirectionally connected YH-HET SST neuron pairs, 7 were chemical and 6 were electrical (Fig. 8C_2).
449 Thus, these data suggest that heterozygous Y777H expression increases reciprocal connectivity among
450 SST neurons, of both the chemical and electrical sort.

451 Finally, although we previously found no alterations in the sEPSC frequency onto the total
452 population of YH-HOM GABAergic neurons, there was an increase in the sEPSC frequency onto those
453 with an NFS phenotype (Shore et al., 2020), suggesting there may be a compensatory increase in
454 excitatory drive onto NFS YH-HOM GABAergic neurons to offset the effects of their decreased

455 membrane excitability. To assess whether there is a similar increase in sEPSC frequency onto SST-
456 expressing YH-HET neurons, which showed a similar decrease in membrane excitability to that of NFS
457 YH-HOM GABAergic neurons, we recorded sEPSCs onto voltage-clamped WT and YH-HET SST neurons.
458 Indeed, there was an increase in sEPSC frequency onto YH-HET SST neurons compared with that of WT
459 (Fig. 8D), suggesting a compensatory increase in excitatory drive onto the most impaired GABAergic
460 subtype.
461
462 **Acute cortical slice recordings confirm the reduced intrinsic excitability of YH-HET SST neurons.**
463 Of the three GABAergic neuron populations assessed, SST-expressing neurons showed the
464 strongest impairments, both direct and indirect, downstream of the heterozygous Y777H variant.
465 Importantly, the observed effects on YH-HET SST neuron physiology were consistent with those that
466 would be expected, based on YH-HET SST subthreshold K_{Na} current increases (Supplemental Fig. $5C_2$, and
467 Fig. $5C_2$), and predicted, based on SST KCNT1 GOF neuron modeling data (Fig. $6F_1$ and $6F_2$). Thus, to test
468 whether the most significant physiological alterations identified in cortical neuron cultures are also
469 present in an experimental preparation with a more organized network, we crossed YH HET mice with
470 homozygous GIN (GFP-expressing Inhibitory Neurons) mice, which express GFP in a subpopulation of
471 SST-expressing neurons of the hippocampus and cortex (Ma et al., 2006; Oliva et al., 2000), and
472 performed electrophysiological recordings in acute brain slices from WT and YH-HET progeny.
473 First, we assessed the effects of the heterozygous Y777H variant on the passive and active
474 membrane properties by performing whole-cell, current-clamp recordings of layer 2/3, GFP-expressing
475 neurons in motor and somatosensory cortical regions of slices prepared from P21–P30 mice (Fig. 9A).
476 Incremental current injections to elicit APs demonstrated a strong impairment in AP generation
477 downstream of the heterozygous Y777H variant, as the YH-HET GFP-expressing neurons fired fewer APs
478 across all current steps than the WT GFP-expressing neurons, similar to that observed in the YH-HET SST

479 cultured neurons. (Fig. 9B and 9C). Although YH-HET GFP-expressing neurons in slice did not show a
480 significant decrease in input resistance relative to those from WT, they did show a large increase in
481 rheobase current, without alterations in AP shape (Fig. 9D). Thus, we confirmed the main
482 electrophysiological finding from culture—the reduced excitability of YH-HET SST neurons—in acute
483 slices from YH-HET juvenile mice.
484

485 **DISCUSSION**

486 More than a decade ago, autosomal dominant mutations were identified in the sodium-gated
487 potassium channel *KCNT1* in multiple patients with severe, childhood epilepsy syndromes (Barcia et al.,
488 2012; Heron et al., 2012). *KCNT1*-related epilepsy patients suffer not only with frequent, early-onset
489 seizures, but also with cognitive impairments, movement disorders, and sometimes additional
490 behavioral and/or psychiatric problems (Bonardi et al., 2021). Unfortunately, after over 10 years of
491 research efforts, *KCNT1*-related epilepsies remain highly refractory to current anti-seizure medications
492 (Bonardi et al., 2021); thus, a better understanding of the pathological mechanisms underlying *KCNT1*-
493 related epilepsies—from mutated gene to altered K^+ current to altered neuronal physiology to altered
494 neural network to seizure—is imperative for advancing therapeutic strategies to improve seizure control
495 and enhance patient quality of life.
496

497 **Heterozygous vs. homozygous *KCNT1* GOF variant effects**

498 Despite the heterozygous nature of *KCNT1* GOF variants in the overwhelming majority of *KCNT1*-
499 related DEE patients, research efforts, including our own, have largely focused on homozygous GOF
500 variant effects on channel function and neuronal physiology (Gertler et al., 2019; Kim et al., 2014;
501 McTague et al., 2018; Mikati et al., 2015; Milligan et al., 2014; Quraishi et al., 2019; Shore et al., 2020;
502 Tang et al., 2016). Heterozygous *KCNT1* GOF variant expression likely results in the formation of

503 heteromeric KCNT1 channels, consisting of both WT and mutant subunits, whose characteristics and
504 kinetics may differ from those of homomeric KCNT1 channels; thus, it is critical to distinguish between
505 GOF variant effects in heteromeric and homomeric KCNT1 channels to identify the pathogenic
506 mechanisms of *KCNT1* GOF variants in DEEs. Recent work in heterologous cells has shown that KCNT1
507 GOF heteromeric channels, with WT and mutant subunits, exhibit K_{Na} current increases that lie between
508 those of WT and KCNT1 GOF homomeric channels (Cole et al., 2021; Dilena et al., 2018; Rizzo et al.,
509 2016). Furthermore, other recent studies have similarly shown that heterozygous *Kcnt1* GOF variant
510 expression in neurons causes effects on K_{Na} current and excitability that are intermediate to those of WT
511 and homozygous variant-expressing neurons (Gertler et al., 2022; Wu et al., 2024).
512 Here, we assessed the effects of heterozygous expression of *Kcnt1*-Y777H on K_{Na} currents,
513 neuronal physiology, and synaptic connectivity among cortical neuron subtypes in mice, and compared
514 the effects to those observed previously with homozygous expression of the same variant (Shore et al.,
515 2020). We found that the heterozygous YH variant caused similar effects on K_{Na} currents and neuronal
516 physiology to those caused by the homozygous YH variant, including subthreshold-specific increases in
517 K_{Na} current, altered AP shape, and impaired AP firing of NFS GABAergic neurons, but with magnitudes
518 intermediate to those of WT and YH-HOM neurons. At the network and whole-animal level, we
519 previously showed that homozygous expression of the YH variant in mice increases homotypic synaptic
520 connectivity (E–E and I–I) and the E/I ratio, resulting in hypersynchronous, hyperexcitable YH-HOM
521 cortical networks and frequent seizures. Here, we found no evidence of similar network alterations in
522 YH-HET cortical networks, which likely explains the infrequent seizures observed in the heterozygous YH
523 mouse model, and together with the YH-HOM data, indicate a strong relationship between network
524 abnormalities and seizure propensity downstream of the YH variant. Furthermore, these data suggest
525 that heterozygous and homozygous *KCNT1* variant expression cause similar, gene-dose-dependent GOF
526 effects at the current and neuron level, but not at the network or whole-animal level.

527

528 **Neuron-type-dependent *KCNT1* GOF variant effects**

529 Prior work has illustrated the importance of cell context in delineating the functional effects of
530 ion channel variants on neuronal physiology. For instance, several studies using LOF channelopathy
531 models of both sodium and potassium channels have identified excitability effects on one neuron type
532 without effects on another (Hedrich et al., 2014; Soh et al., 2018; Tai et al., 2014; Yu et al., 2006). Other
533 studies have shown that the same ion channel variant can even cause opposite effects on excitability in
534 different neuron types (Makinson et al., 2016; Rush et al., 2006; Studtmann et al., 2022). Thus,
535 understanding how KCNT GOF alters networks to lead to hyperexcitability and seizures requires a
536 thorough evaluation of how the variant impacts each neuron type that participates in the network. With
537 this goal in mind, we assessed the effects of heterozygous *Kcnt1* GOF on K_{Na} currents and AP generation
538 among cortical glutamatergic neurons and all three major GABAergic neuron subtypes, including those
539 expressing VIP, SST, and PV.

540 Using two methods to isolate and measure the KCNT1-mediated current, VU170- and TTX-
541 subtraction, we observed voltage-dependent differences in current increases among the YH-HET neuron
542 types. YH-HET glutamatergic and VIP neurons showed KCNT1-mediated current increases across
543 suprathreshold voltages, whereas YH-HET SST and PV neurons had current increases across
544 subthreshold voltages. These neuron-type dependent effects of KCNT1 GOF on K_{Na} current increases are
545 similar to those observed previously in YH-HOM, glutamatergic and GABAergic neuron subpopulations
546 using TTX (Shore et al., 2020). Moreover, these results are similar to those reported in a recent study
547 using a different KCNT1 GOF mouse model (human R474H, mouse R455H), which showed K_{Na} current
548 increases selectively across positive potentials in glutamatergic, but across positive and negative
549 potentials in FS and NFS GABAergic, neurons (Wu et al., 2024). The mechanism underlying these neuron-
550 type-dependent KCNT1 GOF effects on K_{Na} current increases is unknown, however, we have observed

551 differences even in WT KCNT1 channel activation curves between glutamatergic and VIP neurons
552 (steeper slopes of activation) and SST and PV neurons (shallower slopes of activation), suggesting there
553 are factors affecting KCNT1 channel kinetics that are inherent to each neuron type (Fig. 6A). Future
554 studies should investigate these potential factors including (1) differential expression of alternative
555 KCNT1 splice forms, some of which are known to have different activation kinetics, (2) differential
556 expression of other channels such as KCNT2, which can form heteromers with KCNT1 and alter its
557 biophysical properties, and (3) differential expression and/or localization of, and/or coupling to, sodium
558 channels that act as the source of KCNT1 channel activation (Chen et al., 2009; Hage & Salkoff, 2012;
559 Joiner et al., 1998).

560 Consistent with the differential KCNT1 GOF effects on K_{Na} currents, we observed a range of
561 effects on membrane properties and AP generation among the cortical neuron populations. We
562 observed no effects on YH-HET glutamatergic and VIP neurons, whereas YH-HET SST neurons showed
563 reduced AP firing, with decreased input resistance and increased rheobase, and YH-HET PV neurons
564 showed increased AP firing, with decreased rheobase. As a complementary approach, we performed *in*
565 *silico* electrophysiology using our measured neuron-type-specific KCNT1 channel activation kinetics, with
566 and without GOF, for each neuron type. For glutamatergic and VIP neurons, the steeper slopes of
567 activation limited the effects of GOF on intrinsic excitability, whereas for SST neurons, the shallower
568 slope of activation decreased the input resistance, increased the rheobase, and impaired AP generation
569 downstream of KCNT1 GOF. Each of these modeling results are similar to those observed using *in vitro*
570 electrophysiology, indicating direct K_{Na} current-to-KCNT1 GOF phenotype relationships in these neuron
571 types.

572 Conversely, for PV neurons, unlike the experimental observation of increased YH-HET PV neuron
573 excitability, *in silico* electrophysiology predicted a slight reduction in PV neuron excitability downstream
574 of KCNT1 GOF. In support of this *in silico* prediction, in a different KCNT1 GOF mouse model,

575 heterozygous expression of the human L456F variant indeed reduced AP firing of PV neurons, without
576 altering any other membrane properties or AP parameters (Gertler et al., 2022). The opposite effect of
577 KCNT1 GOF on PV excitability between these two studies may simply result from variant-specific
578 alterations in KCNT1 channel kinetics; however, both GOF variants showed a similar lack of effect on
579 membrane properties and AP generation of glutamatergic neurons. Alternatively, the opposite effects
580 could be due to the different experimental conditions used in the two studies, including (1) different
581 preps and mouse ages (acute slices from P42–P60 mice vs. DIV 13–17 cultured neurons from P0 pups)
582 and (2) different brain regions (hippocampal vs. cortical). The idea of brain region-dependent effects of
583 ion channel variants is not unprecedented, as a recent study showed that a potassium channel GOF
584 variant causes opposite effects on excitability in the same neuron type from different brain regions
585 (hippocampal CA1 vs. cortical layer 2/3 pyramidal neurons), and this opposite effect was suggested to
586 be due to the compensatory upregulation of sodium channels in one neuron type but not the other
587 (Varghese et al., 2023). Taken together, these findings illustrate the importance of interrogating not only
588 multiple neuron types but also multiple brain regions to fully unravel the complexity underlying KCNT1
589 GOF-related neurodevelopmental disorders.
590

591 **Evidence of potential neuron and network compensatory responses to KCNT1 GOF**

592 In a healthy brain, there are multiple homeostatic compensation mechanisms to maintain
593 neuronal and network activity at their proper physiological levels (Davis, 2013; Debanne et al., 2019;
594 Debanne & Russier, 2019; Marder & Goaillard, 2006; Turrigiano, 2011, 2012; Yang & Prescott, 2023),
595 whereas in a brain with epilepsy-causing genetic mutations or injury, it is thought that failure of
596 homeostatic compensation can result in hypersynchronous, hyperexcitable networks and, ultimately,
597 seizures (Issa et al., 2023; Lignani et al., 2020; Staley, 2015). As YH-HET mice have only been observed to
598 have infrequent seizures and YH-HET networks appear largely intact, it is plausible that there are

599 adaptive or homeostatic mechanisms downstream of the YH variant that limit KCNT1 GOF effects largely
600 to those observed at the current and neuron level. These regulatory mechanisms may include
601 alterations in ion currents and/or synaptic input to restore proper AP shape or neuronal excitability, or
602 alterations in chemical and/or electrical connectivity to stabilize neural networks.

603 Neuronal excitability is regulated by the inward and outward flow of opposing currents through
604 sodium and potassium channels; thus, it is not surprising that mutations affecting these channels can
605 lead to compensatory up- or down-regulation of other ion channels or currents to maintain excitability
606 and proper neuron function. In this study, our *in silico* electrophysiology predictions of YH-HET PV
607 neuron excitability were opposite to those of our *in vitro* electrophysiology data; thus, we hypothesized
608 that there may be a compensatory increase in an ion current that counteracts the increased K_{Na} current
609 selectively in YH-HET PV neurons. Accordingly, we identified a subthreshold increase in the persistent
610 Na^+ current, across a similar voltage range to the increased K_{Na} current, in YH-HET PV, but not SST,
611 neurons. Furthermore, *in silico* approaches indicated that this increased I_{NaP} was sufficient to overcome
612 the effects of KCNT1 GOF and cause an overall increase in AP generation in YH-HET PV neurons, which
613 aligned with our experimental data. Similar compensatory mechanisms have been identified in other
614 models such as the downregulation of multiple potassium channels in a sodium channel (*Scn2a*) LOF
615 mouse model of epilepsy, resulting in neuronal hyperexcitability (Zhang et al., 2021), or the upregulation
616 of Na^+ currents in response to increased potassium channel activity in a developing Xenopus neural
617 circuit, resulting in restored intrinsic excitability and network stability (Pratt & Aizenman, 2007). Notably,
618 another KCNT1 GOF model (*Kcnt1*-R455H) showed upregulation of a sodium channel ($Na_v1.6$),
619 accompanied by an increase in transient and persistent sodium currents, in *Kcnt1*-R455H cortical
620 neurons, but the effects of Nav1.6 upregulation were not investigated (Wu et al., 2024).

621 In addition to the KCNT1 GOF current-mediated impairments in SST neuron excitability, we
622 identified several potential compensatory YH-HET SST synaptic and network alterations. For instance,

623 there was an increased frequency of sEPSCs onto YH-HET SST neurons, suggestive of a compensatory
624 increase in excitatory input to counteract their reduced intrinsic excitability and increase their AP firing,
625 as has been observed previously in hypoexcitable SST neurons in another epilepsy model (Halabisky et
626 al., 2010). There was also an increase in chemical and electrical coupling between YH-HET SST neurons.
627 Although SST neurons normally show a relatively low rate of homotypic chemical coupling, particularly
628 in the adult cortex, more than half of nearby SST neuron pairs are coupled electrically (Amitai et al.,
629 2002; Gibson et al., 1999, 2005; Hu & Agmon, 2015; Urban-Ciecko & Barth, 2016). This coupling is
630 thought to be important for fine tuning neural circuits by regulating such processes as synchronous AP
631 firing, synaptic integration, and network rhythmicity (Alcami & Pereda, 2019; Connors, 2017). The
632 observed increase in electrical coupling should not only contribute to the reduced intrinsic excitability
633 properties of individual YH-HET SST neurons, increasing their capacitance and decreasing their input
634 resistance, but may also act as a homeostatic mechanism to restore synchronicity and stability to YH-
635 HET SST networks (Lane et al., 2016; Parker et al., 2009).
636 Taken together, how might the YH-HET variant-induced alterations to SST and PV neurons, both
637 direct and adaptive, ultimately contribute to neural network behavior and seizure propensity in YH-HET
638 mice? The paucity of effects on synaptic activity and connectivity in YH-HET networks, relative to those
639 of YH-HOM, suggests that the current- and neuron-level effects of the YH-HET variant are below some
640 threshold required to induce broader network hyperexcitability and seizures. Moreover, as described
641 above, several of the proposed homeostatic mechanisms, such as increased excitatory input onto, and
642 connectivity between, SST neurons and increased I_{NaP} in PV neurons, should theoretically act to suppress
643 pathological network activity in YH HET mice. However, predicting the downstream effects of altered
644 SST and PV intrinsic excitability is not straightforward, particularly with the emerging appreciation of
645 both anti- and pro-epileptic roles for these neuron types in seizure initiation and maintenance (Dudok et
646 al., 2022; Magloire et al., 2019). Furthermore, studies using genetic mouse models of DEEs have

647 identified seemingly paradoxical, and sometimes ephemeral, roles of interneurons in disease
648 progression. For instance, in an *SCN8A* GOF DEE mouse model, increased I_{NaP} causes initial SST
649 hyperexcitability followed by depolarization block, and in parallel, chemogenetic activation of WT SST
650 neurons mimics these effects, leading to seizure generation (Wengert et al., 2021). Similarly, in a
651 *KCNQ2/3* LOF DEE model, PV-specific *Kcnq2/3* deletion causes early PV hyperexcitability that is thought
652 to increase seizure susceptibility via homeostatic potentiation of excitatory transmission (Soh et al.,
653 2018). Lastly, in an *Scn1a*$^{+/-}$ mouse model of Dravet syndrome, PV neurons are transiently hypoexcitable
654 during development, whereas later they show an increased firing rate, both interictally and at seizure
655 onset, and a decrease in synchrony in the transition to seizure (Favero et al., 2018; Tran et al., 2020).
656 These studies illustrate the challenges in connecting altered interneuron intrinsic excitability with
657 network behavioral outcomes not only because of the contradictory nature of some of these
658 connections but also because of the often transient nature of interneuron phenotypes during disease
659 progression. Thus, future studies should aim to assess neuron-type-specific effects of the YH variant at
660 different developmental time points in both YH-HET mice, with rare seizures, and YH-HOM mice, with
661 frequent seizures, to better understand the contributions of interneuron dysfunction to network
662 pathology and seizure generation in KCNT1 GOF-related epilepsy.
663
664 **Limitations and Conclusions**
665 The *in vitro* and *in silico* nature of this study are limitations. Although the cultured VIP, SST, and
666 PV neurons showed characteristic electrophysiological properties, it is unknown how much overlap
667 there is between the *in vitro* and *in vivo* populations. For instance, it is possible that our culture
668 conditions select for more mature neurons of each type or preferentially support the survival of
669 subpopulations; thus, we may be assessing KCNT1 GOF effects on a small portion of a given subtype.
670 However, an advantage of the *in vitro* prep is that the compensatory alterations we observe are not

671 likely consequences of seizure activity, which has been shown to alter interneuron properties in epilepsy
672 models. Furthermore, the *in silico* neurons we used to model each neuron type were designed to
673 accurately reflect the morphological and electrophysiological properties of each subtype, but they may
674 lack more detailed features of ion channels, such as post-translational modifications and subcellular
675 localizations, that can have important functional effects. Our KCNT1 model conductance is also
676 hampered by an incomplete understanding of the relationship between Na^+ influx, membrane voltage,
677 and channel gating in neurons.

678 Moreover, our K^+ current measures using *Kcnt1*$^{-/-}$; *Kcnt2*$^{-/-}$ double knockout neurons clearly
679 showed the presence of an outward VU170-sensitive current across positive potentials, indicating non-
680 specific activity of this small molecule, potentially to the ERG K^+ channel (Spitznagel et al., 2020). This
681 off-target effect of VU170 may contribute to the overall increase in outward K^+ currents seen in our
682 VU170- vs TTX-subtracted currents in all neuron types across positive potentials, and it limits the
683 interpretation of the VU170-sensitive K_{Na} current data within this range. Finally, although it is well
684 known that temperature changes can alter neuron physiology, the electrophysiological recordings in this
685 study were performed at room temperature rather than physiological temperature. In this study, we
686 further assessed the effect of temperature (22°C vs. 35°C) on rheobase, AP amplitude, and maximal AP
687 firing frequency among WT and YH-HET PV neurons and showed that both groups responded similarly.
688 Previously, we also showed that the effects of the homozygous YH variant on glutamatergic and NFS
689 GABAergic neuron excitability were highly similar between cultured recordings at room temperature
690 (~22°C) and slice recordings at 32°C. Taken together, these data suggest that the reported
691 neurophysiological phenotypes downstream of the YH variant are likely not temperature dependent.

692 Despite the potential limitations, this study provides three major findings that advance our
693 understanding of the relationship between ion channel function and disease. First, heterozygous *KCNT1*
694 expression causes changes in current flow and neuron excitability that are qualitatively similar to

695 homozygous expression, but of a lower magnitude; however, the synaptic activity and connectivity
696 changes are different, which likely leads to the discrepancy in seizure incidence. This finding suggests a
697 non-linear relationship between GOF, at the level of the ion channel current, and disease severity.
698 Second, the same *KCNT1* variant can produce opposite effects on neuron excitability in closely related
699 GABAergic neuron subtypes, and these opposite effects are likely due to compensation in one neuron
700 type (PV) that is absent in the other (SST). Previous studies have observed opposite effects on neuronal
701 excitability due to Na^+ channel variants, but the underlying mechanism, when explored, was proposed to
702 be intrinsic differences in ion channel expression, not compensation. Third, we observed increased
703 synaptic and gap junction connectivity among SST neurons, demonstrating that the effects of KCNT1
704 GOF extend to structural alterations as well. The effects of this increased connectivity, especially by gap
705 junctions, on neuronal excitability and network behavior offers an exciting avenue for future research.
706 Finally, it will be critical to determine whether these alterations downstream of KCNT1 GOF potentiate
707 or attenuate network pathology and seizure activity, thus providing a better understanding of disease
708 mechanisms and prompting novel therapeutic design.
709

710 **MATERIALS AND METHODS**

711 ***Mice***

712 Mice were bred, and mouse procedures were conducted, in compliance with the National Institutes of
713 Health (NIH) Guidelines for the Care and Use of Laboratory Animals and were approved by the
714 Institutional Animal Care and Use Committee at the University of Vermont (animal protocol numbers:
715 16-001, 19-034, and X9-022). Mice were maintained in ventilated cages at controlled temperature (22–
716 23°C), humidity ~60%, and 12-h light: 12-h dark cycles (lights on at 7:00 AM, off 7:00 PM). Mice had
717 access to regular chow and water, *ad libitum*. For all experiments, male and female littermates were

718 used for each genotype. The ages of the mice for each experiment are indicated in the following
719 relevant sections.
720
721 Mouse lines and strains used for these studies include: *Kcnt1*^{Y777H} knockin in the C57BL/6NJ (B6NJ) strain
722 (formal gene and allele symbol: *Kcnt1*$^{em1(Y777H)Frk}$), *Sst*-IRES-Cre (*Sst*$^{tm2.1(cre)Zjh}$/J; Jackson Labs stock:
723 013044), *Vip*-IRES-Cre (*Vip*$^{tm1(cre)Zjh}$/J; Jackson Labs stock: 010908), *Pvalb*-IRES-Cre (B6.129P2-
724 *Pvalb*$^{tm1(cre)Arbr}$/J; Jackson Lab stock: 017320), C57Bl/6J (Jackson Labs stock: 000664), and GIN (FVB-
725 Tg(GadGFP)45704Swn/J; Jackson Lab stock: 003718) mice.
726
727 *Kcnt1*^{Y777H} mice were genotyped using PCR amplification primers (*Kcnt1* forward primer: 5'-
728 CTAGGGCTGCAAACACAACA-3'; *Kcnt1* reverse primer: 5'-TCAAGCAGCAACACGATAGG-3') with standard
729 thermocycler amplification conditions, and the annealing temperature set at 58°C. Following
730 amplification, a restriction cut was performed with the enzyme *Nla*III to distinguish mutant (127 and 44
731 bp products after cut) from wildtype (WT) alleles (171 bp product). Progeny of the *Kcnt1*^{Y777H} mice
732 crossed to each Cre mouse line were genotyped for the presence of a *Cre* transgene using a forward
733 primer (5'-TCGCGATTATCT TCTATA TCTTCAG-3') and reverse primer (5'-GCTCGACCAGTTTAGTTACCC-3'),
734 resulting in a 455 bp product.
735
736 ***Primary Astrocyte Feeder Layer Culture***
737 Astrocyte feeder layers were generated to support the growth and maintenance of primary neurons.
738 Briefly, cortices were dissected from P0–P1 WT C57BL/6J mice (Jackson Labs stock: 000664) of either sex.
739 The cortices were incubated in 0.05% trypsin-EDTA (Gibco) for 15 min at 37°C in a Thermomixer
740 (Eppendorf) with gentle agitation (800 rpm). Then, the cortices were mechanically dissociated with a 1-
741 mL pipette tip, and the cells were plated into T-75 flasks containing filter-sterilized astrocyte media

742 [DMEM media supplemented with glutamine (Gibco), 10% fetal bovine serum (FBS, GE Healthcare), 1X
743 MITO+ Serum Extender (Corning), and 0.2X penicillin/streptomycin (Gibco)]. After the astrocytes
744 reached confluency, they were washed with PBS (Gibco) and incubated for 5 min in 0.05% trypsin-EDTA
745 at 37°C, washed, and then resuspended in astrocyte media. Astrocytes were added to 6-well plates
746 containing 25-mm coverslips precoated with coating mixture [0.7 mg/ml collagen I (Corning) and 0.1
747 mg/ml poly-D-lysine (Sigma) in 10 mM acetic acid].
748
749 ***Primary Cortical Neuron Culture***
750 For the primary neuron culture, the dorsomedial cortices from P0–P1 WT and *Kcnt1*$^{m/+}$ mice of both
751 sexes were dissected in cold HBSS (Gibco). The tissue was then digested with papain (Worthington) for
752 60–75 min and treated with inactivating solution (Worthington) for 10 min, both while shaking at 800
753 rpm at 37°C in a Thermomixer. The cells were then mechanically dissociated and counted. The
754 dissociated cells were added at 200,000 cells/well to 6-well plates containing astrocyte-coated
755 coverslips in filter-sterilized NBA plus [Neurobasal-A medium (Gibco) supplemented with 1X Glutamax
756 (Gibco), 1X B27 (Invitrogen), and 0.2X penicillin/streptomycin (Gibco)]. After plating (12-24 h),
757 approximately 4×10^{10} genome copies (GC) of AAV8-*CaMKII*-GFP (UNC Vector Core) were added to each
758 well. For experiments to assess KCNT1 effects on GABAergic subtypes, approximately 4×10^{10} genome
759 copies (GC) of AAV9-*hSyn*-DIO-mCherry (addgene) were also added to each well to mark Cre-expressing
760 neurons. Every 3–4 days, 20–40% of the media was replaced with fresh NBA plus.
761
762 ***Electrophysiology***
763 Whole-cell recordings were performed with patch-clamp amplifiers (MultiClamp 700B; Molecular
764 Devices) under the control of Clampex 10.3 or 10.5 (Molecular Devices, pClamp, RRID:SCR_011323).
765 Data were acquired at 20 kHz and low-pass filtered at 6 kHz. The series resistance was compensated at

766 70%, and only cells with series resistances maintained at less than 15 MΩ were analyzed. Patch
767 electrodes were pulled from 1.5-mm o.d. thin-walled glass capillaries (Sutter Instruments) in five stages
768 on a micropipette puller (model P-97; Sutter Instruments). Internal solution contained the following: 136
769 mM K-gluconate, 17.8 mM HEPES, 1 mM EGTA, 0.6 mM $MgCl_2$, 4 mM ATP, 0.3 mM GTP, 12 mM creatine
770 phosphate, and 50 U/ml phosphocreatine kinase. Alternatively, internal solution contained: 136 mm KCl,
771 17.8 mm HEPES, 1 mm EGTA, 0.6 mm MgCl2, 4 mm ATP, 0.3 mm GTP, 12 mm creatine phosphate, and
772 50 U/ml phosphocreatine kinase. The pipette resistance was between 2 and 4 MΩ. Standard
773 extracellular solution contained the following (in mM): 140 NaCl, 2.4 KCl, 10 HEPES, 10 glucose, 4 $MgCl_2$,
774 and 2 $CaCl_2$ (pH 7.3, 305 mOsm). All experiments were performed at room temperature (22–23°C), with
775 the exception of the current-clamp experiments to compare the effects of temperature on neuronal
776 physiology (Supplemental Figure 4-3). For these recordings, all current-clamp parameters were
777 measured first at room temperature, then the temperature of the external solution was heated to 35°C
778 using a ThermoClamp Inline Heater (ThermoClamp-3; AutoMate Scientific), and the measurements were
779 repeated. Whole-cell recordings were performed on cortical neurons from control and mutant groups in
780 parallel on the same day (day 13–17 *in vitro*). All experiments were performed by two independent
781 investigators blinded to the genotypes.
782
783 For current-clamp experiments, the intrinsic electrophysiological properties of neurons were tested by
784 injecting 500-ms square current pulses incrementing in 20 pA steps, starting at −100 pA. Resting
785 membrane potential (V_m) was calculated from a 50 ms average before current injection. The membrane
786 time constant (τ) was calculated from an exponential fit of current stimulus offset. Input resistance (R_{In})
787 was calculated from the steady state of the voltage responses to the hyperpolarizing current steps.
788 Membrane capacitance was calculated by dividing the time constant by the input resistance. Action
789 potentials (APs) were evoked with 0.5 s, 20 pA depolarizing current steps. Rheobase was defined as the

790 minimum current required to evoke an AP during the 500 ms of sustained somatic current injections. AP
791 threshold was defined as the membrane potential at the inflection point of the rising phase of the AP.
792 AP amplitude was defined as the difference in membrane potential between the AP peak and threshold,
793 and the afterhyperpolarization (AHP) was the difference between the AP threshold and the lowest V_m
794 value within 50 ms. The AP half-width was defined as the width of the AP at half-maximal amplitude. To
795 obtain the neuron's maximum firing frequency, depolarizing currents in 20-pA steps were injected until
796 the number of APs per stimulus reached a plateau phase. The membrane potential values were not
797 corrected for the liquid junction potential. GABAergic neurons were classified as fast spiking (FS) if their
798 maximum mean firing rate reached above 60 Hz and their AP half-widths increased by less than 25%
799 during 1 s of sustained firing (Avermann et al., 2012; Casale et al., 2015). All others were considered
800 non-fast spiking (NFS).
801
802 For voltage-clamp experiments to measure synaptic currents, neurons were held at -70 mV, except for
803 evoked IPSC measurements, for which neurons were held at 0 mV. AP-evoked EPSCs were triggered by a
804 2 ms somatic depolarization to 0 mV. The shape of the evoked response, the reversal potential and the
805 effect of receptor antagonists [10 µM NBQX (Tocris Bioscience) or 20 µM bicuculline (BIC, Tocris
806 Bioscience)] were analyzed to verify the glutamatergic or GABAergic identities of the currents. Neurons
807 were stimulated at 0.1 Hz in standard external solution to measure basal-evoked synaptic responses.
808 Electrophysiology data were analyzed offline with AxoGraph X software (AxoGraph Scientific,
809 RRID:SCR_014284). Spontaneous synaptic potentials were recorded in control solution with either NBQX
810 or bicuculline to isolate EPSCs or IPSCs, respectively. Data were filtered at 1 kHz and analyzed using
811 template-based miniature event detection algorithms implemented in the AxoGraph X. The threshold
812 for detection was set at three times the baseline SD from a template of 0.5 ms rise time and 3 ms decay.

813 The E/I ratio was calculated as the product of the sEPSC frequency and charge over the sum of the sEPSC
814 frequency and charge and the product of the sIPSC frequency and charge.
815
816 ***K_{Na} and KCNT1 Current Measurements***
817 For voltage-clamp experiments to measure the sodium-activated K^+ current or KCNT1-mediated current,
818 neurons were held at -70 mV and given 1 s voltage pulses in 10 mV steps over a range of -80 to +50 mV.
819 Recordings were obtained for each cell in standard extracellular solution or extracellular solution
820 containing 0.5 µM tetrodotoxin (TTX) or 10 µM VU170. TTX or VU170 was applied directly on the
821 recorded neuron with a custom-built fast flow perfusion system capable of complete solution exchange
822 in less than 1 s to minimize the time interval between control and drug recordings and current rundown.
823 Current traces from the TTX or VU170 solution were subtracted from the current traces obtained from
824 the standard solution. The difference current over the 100 ms at the end of the voltage pulse was
825 considered the steady state K_{Na} current. The same protocol was used for outside-out patch experiments.
826
827 ***I_{NaP} Current Measurements***
828 For voltage-clamp experiments to measure the persistent Na^+ current, neurons were held at -80 mV and
829 given a 5 s voltage ramp at 20 mV/s. The ramp was repeated every 10 s. Recordings were obtained for
830 each cell in standard extracellular solution or extracellular solution containing 0.5 µM TTX. TTX was
831 applied directly on the recorded neuron with a custom-built fast flow perfusion system capable of
832 complete solution exchange in less than 1 s to minimize the time interval between control and TTX
833 recordings. The first current trace after TTX application was subtracted from the averaged current traces
834 obtained from the standard solution. At this time point, the effect of TTX on the Na^+-activated K^+ current
835 is minimal, while the persistent Na^+ current is maximally inhibited. This allowed us to isolate the
836 persistent Na^+ current from K_{Na} and obtain a more accurate estimate of changes in I_{NaP}.

837

838 ***Neuron Modeling***

839 Model neurons (~10 per class) representing excitatory (Pyramidal Cell, PC), SST (Martinotti Cell, MC), PV
840 (Large Basket Cell, LBC), and (Bipolar Cell, BP) VIP neurons were downloaded from the EPFL/Blue Brain
841 project (https://bbp.epfl.ch/nmc-portal/downloads.html), and implemented in the NEURON
842 environment. Because no KCNT1-like conductance was present in the original models, a Hodgkin-Huxley
843 KCNT1 model conductance was created with both Na^+- and voltage-dependent gates and inserted into
844 the dendritic, somatic, and axonal compartments of model neurons (0.03 S/cm^2). The Na^+ dependence
845 was modeled after Bischoff et al. (EC_{50} = 40 mM, slope 3.5), and the voltage dependence was modeled
846 after our own experimental data (Fig. 5), corrected to account for the calculated liquid junction potential
847 in the experimental data. To verify that this approach reproduced experimental data, voltage step
848 protocols were run in NEURON with 10 mM and 0 mM internal Na^+. "K_{Na}" currents were obtained by
849 subtraction, and the amplitude and kinetics of the resulting currents were verified to be similar to
850 experimental values. To model the effects of KCNT1 GOF, the EC_{50} for Na^+ was decreased to either 35 or
851 30 mM, because the Y796H variant was previously shown to increase the Na^+ sensitivity of the channel.
852 These changes resulted in moderate increases in the current above WT levels (Fig. 6B), consistent with
853 the experimental data (Fig. 4 and Fig. 5). Modeling data was generated by running current clamp
854 protocols in NEURON for each of the model neurons and analyzed in the same way as experimental data.
855 For modeling the increase in I_{NaP}, the control I_{NaP} conductance was set to 0.001 times the conductance of
856 the transient Na^+ current in each compartment. This produced I_{NaP} currents approximately 1% of the
857 peak of the transient Na^+ current. KCNT1 GOF was modeled by decreasing the Na^+ EC_{50} to 30 mM and
858 the I_{NaP} increase was modeled by increasing its conductance 2-fold, in accordance with experimental
859 data.

860

861 ***Immunostaining, Imaging, and Quantification***

862 For live imaging of GABAergic subtypes *in vitro*, cortical neurons isolated and cultured from VIP-Cre, SST-
863 Cre, and PV-Cre pups, were infected with AAV-*CamKII*-GFP and AAV-*hSyn*-DIO-mCherry viruses at DIV 1
864 to mark glutamatergic and Cre-expressing, GABAergic neurons, respectively. Images were captured from
865 live cultures at DIV 14 (VIP-Cre and SST-Cre) or DIV 16 (PV-Cre) using an inverted Olympus IX73
866 epifluorescent microscope with an Olympus PlanFluor 10× objective lens and an Andor Zyla sCMOS 4.2
867 camera controlled by µManager 2.0-β software (Edelstein et al., 2014). The same acquisition parameters
868 were used for each image and each group.

869

870 For soma size measurements, DIV 16 cultured SST-Cre neurons on coverslips were washed three times
871 with prewarmed PBS, fixed with 4% paraformaldehyde in PBS for 30 min at room temperature, and then
872 washed again three times with PBS. The fixed neurons were then incubated in blocking buffer (10%
873 normal goat serum and 0.1% Triton-100 in 1X PBS) for 1 h at room temperature, followed by incubation
874 with a Neu-N primary antibody (Synaptic Systems 266-004) diluted in blocking buffer (1:500) overnight
875 at 4°C. The next day, the neurons were washed three times with PBS for 10–15 min, incubated with goat
876 anti-guinea pig, Alexa Fluor 647 secondary antibody (Invitrogen A21450) in blocking buffer (1:1000) for 1
877 h at room temperature, and washed again three times with PBS for 10–15 min. The coverslips were then
878 flipped and mounted on glass slides using Fluoromount G with DAPI. Images (1024 × 1024 pixels) of Neu-
879 N to mark all neurons, *CamKII*-GFP to mark glutamatergic neurons, and *hSyn*-DIO-mCherry to mark Cre-
880 expressing neurons, were obtained using a DeltaVision Restoration Microscopy System (Applied
881 Precision/GE Life Sciences) with an inverted Olympus IX70 microscope with a 20 × oil objective,
882 SoftWoRx software, and a CoolSNAP-HQ charge-coupled device digital camera (Photometrics). Image
883 exposure times and settings were kept the same between groups in a culture and were optimized to
884 ensure that there were no saturated pixels. To analyze soma size, regions of interest (ROIs) were drawn

885 around cell bodies using the mCherry channel with Fiji software (Schindelin et al., 2012), and then the
886 cell body areas were measured for each mCherry$^+$ neuron imaged.
887
888 ***Mouse cortex slice preparation***
889 Cortical slices were prepared from P21–P30 WT and *Kcnt1*-Y777H heterozygous pups, which were the
890 progeny of *Kcnt1*-Y777H heterozygous mice crossed to homozygous GIN mice (JAX stock #003718),
891 which express GFP in a subset of SST-positive neurons (Ma et al., 2006; Oliva et al., 2000), following a
892 modified protocol (Ting et al., 2014). Briefly, mice were deeply anesthetized with isoflurane and
893 transcardially perfused with 25–30 mL of ice-cold NMDG aCSF (in mM: 93 NMDG, 2.5 KCl, 1.2 NaH_2PO_4,
894 30 $NaHCO_3$, 20 HEPES, 25 D-glucose, 5 Na-ascorbate, 2 thiourea, 3 Na-pyruvate, 12 N-acetyl-L-cysteine,
895 10 $MgSO_4$, 0.5 $CaCl_2$, with pH adjusted to 7.3–7.4 with 10 N HCl) that was saturated with carbogen (95%
896 O_2, 5% CO_2 (pH 7.3–7.4). The mice were rapidly decapitated, and the heads were submerged in ice-cold
897 NMDG aCSF bubbled with carbogen. After extraction from the skull, the cortex was blocked and 250-µm
898 coronal sections were cut with a vibrating microslicer (Leica VT100S, Leica Biosystems) while submerged
899 in the same solution. Slices were first moved to NMDG aCSF at 32–34°C for a short-term recovery (≤ 15
900 min) before being transferred into HEPES-based holding aCSF (in mM: 92 NaCl, 2.5 KCl, 1.2 NaH_2PO_4, 30
901 $NaHCO_3$, 20 HEPES, 25 D-glucose, 5 Na-ascorbate, 2 thiourea, 3 Na-pyruvate, 12 N-acetyl-L-cysteine, 2
902 $MgSO_4$, 2 $CaCl_2$, bubbled with carbogen, with pH adjusted to 7.3–7.4 with KOH or HCl as necessary). The
903 slices were held in this solution until use.
904
905 ***Ex vivo slice electrophysiology***
906 For recording, the cortical slices were placed in a chamber mounted on a fluorescence microscope (Zeiss
907 Axio Examiner.D1) and perfused with normal Ringer's solution containing (in mM): 130 NaCl, 3 KCl, 2
908 $MgCl_2$, 2 $CaCl_2$, 1.25 NaH_2PO_4, 26 $NaHCO_3$, and 10 D-glucose, bubbled with carbogen. Patch electrodes

909 were pulled from 1.5-mm o.d. thin-walled glass capillaries (Garner Glass Company) in two stages on a
910 micropipette puller (model P-1000; Sutter Instruments). Electrophysiological recordings were obtained
911 from GFP-labeled neurons in layer 2/3 of either motor or somatosensory cortex using pClamp, an
912 MultiClamp 700B amplifier, and a Digidata 1440A analog-to-digital converter (Molecular Devices). Data
913 were acquired at 20 kHz and low-pass filtered at 10 kHz. Internal solution contained the following (in
914 mM): 17.5 KCl, 112.5 K-gluconate, 1.5 NaCl, 5 Na_2-phosphocreatine, 1 $MgCl_2$, 10 HEPES, 0.2 EGTA, 3 Mg-
915 ATP, 0.3 GTP-Tris (pH 7.2, with KOH). The pipette resistance was between 3 and 5 MΩ. All experiments
916 were performed at room temperature (22–23°C).
917
918 The intrinsic electrophysiological properties of neurons were tested using current-clamp recording
919 under whole-cell configuration by injecting 1 s square current pulses in 5-pA steps, starting at −30 pA. All
920 recordings were saved in the computer for off-line analysis using Clampfit 11.2 or Axograph X software.
921 The membrane time constant (τ) was calculated from an exponential fit of current stimulus offset. Input
922 resistance (R_{in}) was calculated from the steady state of the voltage responses to the hyperpolarizing
923 current steps. Membrane capacitance was calculated by dividing the time constant by the input
924 resistance. Action potential (AP) frequency was counted on each depolarizing current step and plotted
925 as a function of injection current. Rheobase was defined as the minimum current required to evoke an
926 AP during the 1 s of sustained somatic current injections. AP threshold was defined as the membrane
927 potential at the inflection point of the rising phase of the AP, and the afterhyperpolarization (AHP) was
928 the difference between the AP threshold and the lowest V_m value within 50 ms. The membrane
929 potential values were not corrected for the liquid junction potential.
930
931 ***Data Presentation and Statistical Analysis***

932 Prism 10 (GraphPad Prism, RRID:SCR_002798) was used to create all graphs. To test for statistical
933 significance for all whole cell electrophysiology experiments, we used generalized linear mixed models
934 (GLMM) in SPSS [28.0 Chicago, III (IBM, RRID:SCR_002865], which allows for within-subject correlations
935 and the specification of the most appropriate distribution for the data. Because neurons and animals
936 from the same culture or animal are not independent measurements, culture or litter was used as the
937 subject variable, and animals, neurons, and voltage steps were considered within-subject measurements.
938 All data distributions were assessed with the Shapiro-Wilk test. Datasets that were significantly different
939 from the normal distribution ($p < 0.05$) were fit with models using the gamma distribution and a log link
940 function, except for synaptic connection probability, which was fit with the binomial distribution and
941 probit link. Normal datasets were fit with models using a linear distribution and identity link. We used
942 the model-based estimator for the covariance matrix and goodness of fit was determined using the
943 corrected quasi likelihood under independence model criterion and by the visual assessment of
944 residuals. All values reported in the text, figures, and tables are estimated marginal means +/- standard
945 error, except where noted.
946
947 **Acknowledgements**
948 This work was supported by NIH/NINDS grants NS087095 (M.C.W.), NS110945 (M.C.W.), NS031348
949 (W.N.F.), R33NS109521 (C.D.W. and K.A.E.), and OD020351 (The Jackson Laboratory Center for Precision
950 Genetics). The authors would like to acknowledge the support of the Microscopy Imaging Center (RRID#
951 SCR_018821) and the Cellular & Molecular Core at the University of Vermont.
952
953 **Author Contributions:** Conceptualization, A.N.S., W.N.F., M.C.W.; Methodology, A.M.Q., B.D.S., K.A.E.,
954 C.D.W., Formal Analysis, A.N.S., M.C.W. K.L., M.S.; Investigation, A.N.S., M.C.W., K.L., M.S.; Writing-

955 Original Draft, A.N.S, M.C.W., Revising and Editing, A.N.S., M.C.W.; Supervision, K.A.E., C.D.W., W.N.F.,
956 M.C.W.; Funding Acquisition, W.N.F., M.C.W.
957
958 **FIGURE LEGENDS**
959 **Figure 1. Heterozygous *Kcnt1*-Y777H expression alters AP shape and generation in NFS GABAergic**
960 **neurons. (A_1-A_3)** On the left, representative responses to step currents are shown for glutamatergic, and
961 FS and NFS GABAergic, WT (black) and YH-HET (colors) neurons (top to bottom), illustrating the input
962 resistance (in response to a depolarizing step) and the rheobase (the first trace with an AP in response
963 to a hyperpolarizing step) for each neuron type. On the right, bar graphs show quantification and mean
964 ± SEM of the membrane properties and AP parameters for each neuron type for WT (grey) and YH-HET
965 (colors) groups, with individual neuron measurements overlaid in scatter plots. The p-values are shown
966 on each graph where $p < 0.05$. **(B_1-B_3)** Representative traces are shown at low, medium, and high
967 current steps for glutamatergic, and FS and NFS GABAergic, WT (black) and YH-HET (colors) neurons (left
968 to right). The line graphs below show the number of APs (mean ± SEM) per current injection step in WT
969 (black) and YH-HET (colors) neurons. Statistical significance was tested using Generalized Linear Mixed
970 Models, and p-values are shown on each graph where $p < 0.05$.
971
972 **Figure 2. Heterozygous *Kcnt1*-Y777H expression increases subthreshold K_{Na} currents in NFS GABAergic**
973 **neurons. (A_1-A_3)** Representative traces in control (top), 0.5 µM TTX (middle), and the difference current
974 (bottom) calculated by subtracting the membrane current response to voltage steps (-80 to +50 mV)
975 from a holding potential of -70 mV in TTX from the response in control external solution in glutamatergic,
976 and FS and NFS GABAergic, WT (black) and YH-HET (colors) neurons. To include all of the representative
977 traces in the figures, and prevent overlap of the traces, the large inward sodium currents were removed
978 from each set of traces using the masking tool in Adobe Illustrator. **(B_1-B_3)** Summary data shows the K_{Na}

979 current (mean ± SEM) for each voltage step in glutamatergic, and FS and NFS GABAergic, WT (black and
980 gray) and YH-HET (colors) neurons. The p-values are shown on each graph where $p < 0.05$, and the n
981 values are the number of neurons recorded for each group. **(C_1-C_3)** Plots of the K_{Na} current (mean ± SEM)
982 for each voltage step from -80 to 0 mV in WT (black and gray) and YH-HET (colors) neurons to illustrate
983 the values that are too small to be seen on the graphs in B_1-B_3. The shaded red area in C_3 indicates the
984 subthreshold voltage range with significantly higher K_{Na} currents (red voltages along x-axis indicate steps
985 where $p < 0.05$) in YH-HET relative to WT neurons. The p-values are shown on each graph where $p < 0.05$,
986 and the n values are the number of neurons recorded for each group. Statistical significance for I-V plots
987 was tested using Generalized Linear Mixed Models with genotype and voltage step as fixed effects
988 followed by pairwise comparisons at each level.
989
990 **Figure 3. Heterozygous *Kcnt1*-Y777H expression does not alter synaptic connectivity or the excitation-**
991 **inhibition balance. (A_1-A_4)** Evoked postsynaptic currents (PSCs) were recorded from neuron pairs
992 [glutamatergic (excitatory, E) and GABAergic (inhibitory, I)] by stimulating the neuron type indicated on
993 the left and recording the response in the neuron type indicated on the right (WT, gray; YH-HET E,
994 green; YH-HET I, red). Bar graphs below each recorded neuron pair schematic show summary data
995 (mean ± SEM) of the connection probability (left graph; numbers on bars represent connected pair
996 number/recorded pair number) and peak evoked PSC amplitude (right graph; dots represent individual
997 evoked responses) between each motif. **(B_1)** Bar graphs with overlaid individual neuron measurements
998 and mean ± SEM show the spontaneous EPSC (sEPSC) or IPSC (sIPSC) frequency onto E neurons (WT,
999 gray; YH-HET, green). **(B_2)** Bar graphs with overlaid individual neuron measurements and mean ± SEM
1000 show the sEPSC or sIPSC frequency onto I neurons (WT, gray; YH-HET, red). **(B_3)** Scatter plots show
1001 individual E/I ratio measurements onto E neurons (WT, gray; YH-HET, green) and I neurons (WT, gray;
1002 YH-HET, red). The p-values are shown on each graph where $p < 0.05$.

1003

1004 **Figure 4. Heterozygous *Kcnt1*-Y777H expression differentially affects the intrinsic excitability of SST-**

1005 **and PV-expressing GABAergic neurons. (A)** A schematic diagram illustrates the strategy for generating

1006 fluorescently labeled GABAergic subtype-specific neurons. YH-HET mice were crossed to VIP-, SST-, or

1007 PV-Cre mice, and the resulting P0 WT and YH-HET littermate pups were used to isolate and culture

1008 cortical neurons. At DIV 1, neurons were infected with AAV-*CamKII*-GFP to label glutamatergic neurons,

1009 and AAV-*hSyn*-DIO-mCherry to label Cre-expressing neurons. At DIV 13–17, whole-cell, patch-clamp

1010 electrophysiology was performed on $mCherry^+/GFP^-$ neurons. **(B_1-B_3)** On the left, representative

1011 responses to step currents are shown for VIP-, SST-, and PV-expressing WT (black) and YH-HET (colors)

1012 neurons (top to bottom). For each neuron type, the superimposed dark traces illustrate the input

1013 resistance (in response to a depolarizing step) and the rheobase (the first trace with an AP in response

1014 to a hyperpolarizing step), and the light trace shows the first step current response to induce repetitive

1015 AP firing across the step. Above the superimposed traces, the first AP of each rheobase trace is shown

1016 (same vertical scale, increased horizontal scale). On the right, bar graphs show quantification of the

1017 membrane properties and AP parameters for each neuron type (VIP, SST, and PV, top to bottom) for WT

1018 (grey) and YH-HET (colors) groups, with individual neuron measurements overlaid in scatter plots. The p-

1019 values are shown above each graph where $p < 0.05$. **(C_1-C_3)** For VIP-, SST-, and PV-expressing neurons

1020 (left to right), representative traces are shown at low, medium, and high current steps, and the line

1021 graphs below show the number of APs (mean ± SEM) per current injection step in WT (black) and YH-

1022 HET (colors) neurons. Statistical significance was tested using Generalized Linear Mixed Models, and p-

1023 values are shown above each graph where $p < 0.05$.

1024

1025 **Figure 5. The *Kcnt1*-Y777H variant increases KCNT1-mediated currents across subthreshold voltages in**

1026 **SST- and PV-expressing GABAergic neurons. (A_1-A_3)** Representative traces in control (top), 10 µM

1027 VU170 (middle), and the difference current (bottom) calculated by subtracting the membrane current
1028 response to voltage steps (-80 to +50 mV) from a holding potential of -70 mV in VU170 from the
1029 response in control external solution in VIP-, SST-, and PV-expressing, WT (black) and YH-HET (colors)
1030 neurons. To include all of the representative traces in the figures, and prevent overlap of the traces, the
1031 large inward sodium currents were removed from each set of traces using the masking tool in Adobe
1032 Illustrator. **(B_1-B_3)** Summary data shows the KCNT1 current (mean ± SEM) for each voltage step in VIP-,
1033 SST-, and PV-expressing, WT (black and gray) and YH-HET (colors) neurons. The p-values are shown on
1034 each graph where $p < 0.05$, and the n values are the number of neurons recorded for each group. **(C_1-C_3)**
1035 Plots of the K_{Na} current (mean ± SEM) for each voltage step from -80 to 0 mV in WT (black and gray) and
1036 YH-HET (colors) neurons to illustrate the values that are too small to be seen on the graphs in B_1-B_3. The
1037 shaded red areas in C_2 and C_3 indicate the subthreshold voltage range with significantly higher K_{Na}
1038 currents ($p < 0.05$) in YH-HET relative to WT neurons. Statistical significance for I-V plots was tested
1039 using Generalized Linear Mixed Models with genotype and voltage step as fixed effects followed by
1040 pairwise comparisons at each level.
1041
1042 **Figure 6. Compartmental models of KCNT1 GOF in SST, but not PV, neurons are consistent with**
1043 **experimental data. (A)** Activation curves for VIP, SST, and PV neurons used to model the KCNT1 channel
1044 in each neuron type. **(B)** Representative traces of the response of an outside-out membrane patch
1045 pulled from an SST neuron in control external solution (top) and after application of 10 µm VU170
1046 (bottom). **(C)** Representative trace of the VU170-sensitive current in an outside-out patch pulled from an
1047 SST neuron with a single exponential fit (red curve) overlaid and summary data showing the time
1048 constant (mean ± SEM) obtained from these fits. **(D)** Simulated traces showing the KCNT1-mediated
1049 current in model neurons at three levels of Na^+-sensitivity (Con-40 mM, GOF-35 mM, and GOF-30 mM).
1050 **(E_1, F_1, and G_1)** Simulated traces from model VIP (E_1; purple), SST (F_1; blue), and PV (G_1; yellow) neurons

1051 in response to 500-ms current injections at three levels of Na^+-sensitivity [control (Con), and two levels
1052 of KCNT1 GOF]. Representative traces are shown at increasing current steps from bottom to top for
1053 each level. **(E_2, F_2, and G_2)** Summary data from 10 model VIP (E_2; purple), SST (F_2; blue), and PV (G_2;
1054 yellow) neurons showing (from left to right) the number of APs at different current steps (F-I plot), the
1055 input resistance, and rheobase. The bar graphs (mean ± SEM) are overlaid with scatter plots of individual
1056 neuron measurements. Statistical significance was tested using a Repeated Measures ANOVA. Asterisks
1057 indicate where $p < 0.05$ (*), $p \leq 0.01$ (**), and $p \leq 0.001$ (***).
1058
1059 **Figure 7. The persistent Na^+ current is increased by the *Kcnt1*-Y777H variant in PV, but not SST,**
1060 **neurons. (A)** Representative traces of WT (left) and YH-HET (right) SST neurons in response to slow
1061 voltage ramp in control (dark gray) and 7 seconds after application of 0.5 nM TTX (light gray) with the
1062 difference current (I_{NaP}) plotted on the same scale. **(B)** I_{NaP} I-V curves of WT (gray) and YH-HET (blue) SST
1063 neurons constructed from averaging the ramp-evoked difference current (mean ± SEM) at 5-mV
1064 intervals (left), and a bar graph with overlaid scatter plot showing the peak negative value for each
1065 neuron (right). **(C)** Representative traces of WT (left) and YH-HET (right) PV neurons in response to slow
1066 voltage ramp in control (dark gray) and 7 seconds after application of 0.5 nM TTX (light gray) with the
1067 difference current (I_{NaP}) plotted on the same scale. The upper traces and difference currents are plotted
1068 on different scales. **(D)** I_{NaP} I-V curves of WT (gray) and YH-HET (orange) PV neurons constructed from
1069 averaging the ramp-evoked difference current (mean ± SEM) at 5-mV intervals (left), and a bar graph
1070 with overlaid scatter plot showing the peak negative value for each neuron (right). **(E)** Simulated traces
1071 from a model PV neuron in response to 500-ms current injections with control levels of KCNT1 (black
1072 traces) and KCNT1 GOF (Na^+ EC_{50} = 35 mM) with a 2-fold increase in I_{NaP} (orange traces). Representative
1073 traces are shown at increasing current steps from bottom to top for each level. **(F)** F-I plot shows the
1074 increase in AP firing (left), and a bar graph with overlaid scatter plot of individual neuron values shows

1075 the decrease in rheobase associated with modeling KCNT1 GOF (Na^+ EC_{50} = 35 mM) together with the
1076 increase in I_{NaP}. For modeling data, statistical significance was tested using a Repeated Measures ANOVA.
1077 Asterisks indicate where $p < 0.05$ (*), $p \leq 0.01$ (**), and $p \leq 0.001$ (***).
1078
1079 **Figure 8. YH-HET SST neurons show increased chemical and electrical coupling and receive increased**
1080 **excitatory input. (A and B)** Evoked postsynaptic currents (PSCs) were recorded from SST neuron pairs by
1081 stimulating each neuron at 0.1 Hz and recording the response onto the partner. **(A)** A bar graph shows
1082 the connection probability (mean + SEM) between SST neurons (WT, gray; YH-HET, blue; numbers on
1083 bars represent connected pair number/recorded pair number). **(B)** On the left, example traces of evoked
1084 IPSCs [individual IPSCs (light) overlaid by averaged IPSCs (dark)], and on the right, a graph of connection
1085 strength between SST neurons (WT, gray; YH-HET, blue; individual measurements and summary violin
1086 plots). **(C_1)** A schematic illustrates representative responses (presynaptic, black; postsynaptic, red)
1087 between chemically coupled (upper two panels) and electrically coupled (lower two panels) SST neurons
1088 following 100-pA (left two panels) and AP (right two panels) stimulation. **(C_2)** Summary data of four
1089 possible connection motifs (not coupled, chemical: one-way, chemical: two-way, and electrical) tested
1090 among WT (gray box) and YH-HET (blue box) SST neuron pairs (20 pairs/group). **(D)** On the left, example
1091 traces of spontaneous EPSCs (sEPSCs) recorded onto SST neurons (WT, black; YH-HET, blue). On the right,
1092 a graph shows individual neuron measurements and summary violin plots of the sEPSC frequency onto
1093 SST neurons (WT, gray; YH-HET, blue). All significant p-values are displayed at the top of each graph.
1094
1095 **Figure 9. Acute cortical slice recordings confirm the reduced intrinsic excitability of YH-HET SST**
1096 **neurons. (A)** An inverted monochrome image illustrates the recording scheme from GFP-expressing
1097 neurons in acute slices from P21–P30 GIN mice that express GFP in a subset of SST-positive neurons. **(B)**
1098 Representative responses to current steps are shown for WT (black) and YH-HET (blue) to three,

1099 equivalent 1 s current steps. **(C)** Plot of the action potential frequency (mean ± SEM) per current
1100 injection step shows that YH-HET GFP-expressing neurons (blue) fire fewer action potentials than those
1101 of WT (grey) across a range of current inputs. **(D)** Bar graphs show quantification of the membrane
1102 properties and AP parameters for WT (grey) and YH-HET (colors) GFP-expressing neuron groups, with
1103 individual neuron measurements overlaid in scatter plots.
1104
1105 **Supplemental Figure 2-1. The magnitudes of the K_{Na} current increases in YH-HET glutamatergic and**
1106 **NFS GABAergic neurons are intermediate to those of WT and YH-HOM neurons.** Bar graphs (top three)
1107 illustrate differences in K_{Na} current (mean ± SEM) between YH-HET [dark color; WT littermates (black)]
1108 and YH-HOM [light color; WT littermates (gray)] neurons for voltage steps where significant increases
1109 were previously observed (red asterisks where $p < 0.05$) in glutamatergic, and FS and NFS GABAergic,
1110 YH-HOM neurons. Line graphs (bottom three) illustrate differences in K_{Na} current (mean ± SEM) between
1111 YH-HET [dark color; WT littermates (black)] and YH-HOM [light color; WT littermates (gray)] neurons
1112 across negative voltage steps (-80 to -20 mV; red asterisks where $p < 0.05$ in YH-HOM compared with
1113 WT) in glutamatergic, and FS and NFS GABAergic, neurons.
1114
1115 **Supplemental Figure 4-1. Cre recombinase-expressing, cortical GABAergic neuron subpopulations**
1116 **retain characteristic electrophysiological features in culture.** Cortical neurons isolated and cultured
1117 from P0 pups (*Kcnt1*$^{+/+}$) from VIP-, SST-, or PV-Cre mouse lines were infected with AAV-*CamKII*-GFP to
1118 label glutamatergic neurons, and AAV-*hSyn*-DIO-mCherry to label Cre-expressing neurons, at DIV 1. **(A)**
1119 Images show GFP^{+} glutamatergic neurons and mCherry^{+} VIP-, SST-, or PV-expressing neurons (left to
1120 right) at DIV 14 (VIP and SST) or DIV 16 (PV). The scale bars represent 50 µm. **(B)** Representative
1121 responses to step currents are shown for VIP (purple), SST (blue), and PV (orange) neurons (left to right).
1122 For each neuron type, the superimposed dark traces illustrate the input resistance (in response to a

1123 depolarizing step) and the rheobase (the first trace with an AP in response to a hyperpolarizing step),
1124 and the light trace shows the first step current response to induce repetitive AP firing across the step.
1125 **(C)** On the left, the first AP of each rheobase trace is shown for VIP (purple), SST (blue), and PV (orange)
1126 neurons. On the right, bar graphs show quantification of the membrane properties and AP parameters
1127 for each neuron type (VIP, SST, and PV, left to right), with individual neuron measurements overlaid in
1128 scatter plots.
1129
1130 **Supplemental Figure 4-2. YH-HET SST neurons have increased soma size compared with those of WT.**
1131 Cortical neurons were isolated and cultured from P0 pup progeny (WT and YH-HET) of YH-HET mice
1132 crossed to SST-Cre mice. Neurons were infected with AAV-*CamKII*-GFP to label glutamatergic neurons,
1133 and AAV-*hSyn*-DIO-mCherry to label Cre-expressing neurons, at DIV 1, and immunostained using anti-
1134 Neu-N antibodies at DIV 16. **(A)** Top two images show mCherry$^+$ SST-expressing neurons as a
1135 subpopulation of Neu-N$^+$ cortical neurons, and bottom two images show GFP$^-$, mCherry$^+$ SST-expressing
1136 neurons intermingled with GFP$^+$ glutamatergic neurons. The scale bars represent 50 µm. **(B)** A graph
1137 shows individual neuron measurements and summary violin plots of the mCherry$^+$ neuron soma size
1138 (WT, gray; YH-HET, blue) with the p-value displayed at the top.
1139
1140 **Supplemental Figure 4-3. YH-HET and WT PV neurons show similar neurophysiological responses to**
1141 **increased temperature.** YH-HET mice were crossed to PV-Cre mice, and the resulting P0 WT and YH-HET
1142 littermate pups were used to isolate and culture cortical neurons. At DIV 1, neurons were infected with
1143 AAV-*CamKII*-GFP to label glutamatergic neurons, and AAV-*hSyn*-DIO-mCherry to label Cre-expressing
1144 neurons. At DIV 16 and 17, whole-cell, patch-clamp electrophysiology was performed on glutamatergic
1145 (mCherry$^-$/GFP$^+$), GABAergic (mCherry$^-$/GFP$^-$), or PV (mCherry$^+$/GFP$^-$) neurons at room temperature
1146 (~22°C). Then, the external solution was warmed to 35°C, and the measurements were repeated. **(A)**

1147 Before-after plots of glutamatergic and GABAergic WT neurons (n=16) show alterations in all parameters
1148 measured with increased temperature, excluding the resting membrane potential (V_{rest}) and membrane
1149 capacitance (C_m). **(B)** Before-after plots show highly similar responses to temperature increases between
1150 WT (n=11) and YH-HET (n=10) PV neurons for rheobase, AP amp, and maximal firing frequency (MFR).
1151 Empty circles represent individual neurons, and filled-in circles represent the averages for each group.
1152 Lines connect the before and after measurements for each neuron.
1153
1154 **Supplemental Figure 5-1. The *Kcnt1*-Y777H variant increases K_{Na} currents measured with TTX**
1155 **subtraction across subthreshold voltages in SST-expressing GABAergic neurons. (A_1-A_3)** Representative
1156 traces in control (top), 0.5 µM TTX (middle), and the difference current (bottom) calculated by
1157 subtracting the membrane current response to voltage steps (-80 to +50 mV) from a holding potential of
1158 -70 mV in TTX from the response in control external solution in VIP-, SST-, and PV-expressing, WT (black)
1159 and YH-HET (colors) neurons. To include all of the representative traces in the figures, and prevent
1160 overlap of the traces, the large transient inward sodium currents were removed from each set of traces
1161 using the masking tool in Adobe Illustrator. **(B_1-B_3)** Summary data shows the K_{Na} current (mean ± SEM)
1162 for each voltage step in VIP-, SST-, and PV-expressing, WT (black and gray) and YH-HET (colors) neurons.
1163 The p-values are shown on each graph where $p < 0.05$, and the n values are the number of neurons
1164 recorded for each group. **(C_1-C_3)** Plots of the K_{Na} current (mean ± SEM) for each voltage step from -80 to
1165 0 mV in WT (black and gray) and YH-HET (colors) neurons to illustrate the values that are too small to be
1166 seen on the graphs in B_1-B_3. The shaded red area in C_2 indicates the subthreshold voltage range with
1167 significantly higher K_{Na} currents in YH-HET relative to WT neurons. Statistical significance for I-V plots
1168 was tested using Generalized Linear Mixed Models with genotype and voltage step as fixed effects
1169 followed by pairwise comparisons at each level.
1170

1171 **Supplemental Figure 5-2. Isolation of K_{Na} currents from neurons lacking KCNT1 and KCNT2 channels**
1172 **illustrates the specificity of VU170- vs. TTX-subtraction methods.** Voltage steps were applied to
1173 voltage-clamped neurons isolated and cultured from *Kcnt1*$^{-/-}$; *Kcnt2*$^{-/-}$ double knockout mice to compare
1174 the delayed outward currents before and after the addition of either 10 µM VU170 or 0.5 µM TTX. **(A)** A
1175 summary plot shows the VU-sensitive (red) and TTX-sensitive (grey) difference currents (mean ± SEM)
1176 for each voltage step, which were calculated by subtracting the membrane current response to voltage
1177 steps (-80 to +50 mV) from a holding potential of -70 mV in VU170 or TTX from the response in control
1178 external solution. **(B)** A summary plot of the VU-sensitive (red) and TTX-sensitive (grey) difference
1179 currents (mean ± SEM) for each voltage step from -80 to 0 mV to illustrate the values that are too small
1180 to be seen on the graph in (A).
1181
1182 **Supplemental Figure 6-1. Model VIP and glutamatergic neurons with insertion of SST-like, KCNT1 GOF**
1183 **kinetics show reduced excitability. (A_1)** Simulated traces from model VIP neurons, using VIP KCNT1
1184 activation curve parameters (purple) or SST KCNT activation curve parameters (blue), in response to
1185 500-ms current injections at two levels of Na^+-sensitivity (Con-40 mM and GOF-30 mM). Representative
1186 traces are shown at increasing current steps from bottom to top for each level. **(A_2)** Summary data from
1187 10 model VIP neurons, with VIP KCNT1 parameters (VIP-Con and VIP-GOF) or SST KCNT1 parameters
1188 (SST-GOF) showing (from left to right) the number of APs at different current steps (F-I plot), the input
1189 resistance, and rheobase. The bar graphs (mean ± SEM) are overlaid with scatter plots of individual
1190 neuron measurements. **(B_1)** Simulated traces from model glutamatergic neurons, using glutamatergic
1191 KCNT1 activation curve parameters (green) or SST KCNT activation curve parameters (blue), in response
1192 to 500-ms current injections at two levels of Na^+-sensitivity (Con-40 mM and GOF-30 mM).
1193 Representative traces are shown at increasing current steps from bottom to top for each level. **(B_2)**
1194 Summary data from 10 model glutamatergic neurons, with glutamatergic KCNT1 parameters (Glut-Con

1195 and Glut-GOF) or SST KCNT1 parameters (SST-GOF) showing (from left to right) the number of APs at
1196 different current steps (F-I plot), the input resistance, and rheobase. The bar graphs (mean ± SEM) are
1197 overlaid with scatter plots of individual neuron measurements. Statistical significance was tested using a
1198 Repeated Measures ANOVA. Asterisks indicate where $p < 0.05$ (*), $p \leq 0.01$ (**), and $p \leq 0.001$ (***).
1199
1200 **Supplemental Figure 6-2. Model neurons show differential responses to KCNT1 GOF. (A)** Bar graphs
1201 (mean ± SEM) with overlaid dot plots show the effects of two levels of KCNT1 GOF (Na^+ EC_{50} = 35 or 30
1202 mM) relative to those of control (EC_{50} = 40 mM) on input resistance, rheobase, and AP firing rate at 1.5 ×
1203 rheobase for GABAergic subtypes (10 model neurons/group). **(B)** Bar graphs (mean ± SEM) with overlaid
1204 dot plots show the effects KCNT1 GOF (Na^+ EC_{50} = 30 mM) on VIP GABAergic or glutamatergic model
1205 neurons (10/group) with their respective KCNT1 activation curve parameters (VIP-GOF and Glut-GOF) or
1206 SST KCNT1 parameters (SST-GOF) relative to those of control (EC_{50} = 40 mM) on input resistance,
1207 rheobase, and AP firing rate at 1.5 × rheobase.
1208
1209 **Supplemental Figure 7-1. The rate of K_{Na} current block after TTX application is slow relative to I_{NaP}**
1210 **block in GABAergic neurons.** Plots show the time course over which I_{NaP} and K_{Na} currents are blocked
1211 following 0.5 µM TTX application. Neurons of the labeled type in each panel were voltage clamped and
1212 subjected to a slow voltage ramp protocol (20 mV/s over 5 s). TTX (0.5 µM) was applied at time 0 and
1213 K_{Na} currents and I_{NaP} were measured on each successive sweep. The K_{Na} current was measured as the
1214 normalized difference between each trace and the mean of the pre-TTX current between +20 and +30
1215 mV. I_{NaP} was measured as the normalized difference between each trace and the mean of the pre-TTX
1216 current at the 10 mV bracketing the local peak inward current. Once the minimum value was reached
1217 for I_{NaP}, all subsequent values were considered zero.
1218

1219 **Supplemental Figure 7-2. Model PV neurons show differential responses to KCNT1 GOF with increased**

1220 **I_{NaP}.** Bar graphs (mean ± SEM) with overlaid dot plots show the effects of two levels of KCNT1 GOF (Na^+

1221 EC_{50} = 35 or 30 mM), with or without additional I_{NaP}, relative to those of control (EC_{50} = 40 mM) on input

1222 resistance, rheobase, and AP firing rate at 1.5 × rheobase for PV neurons (10/group).

1223

1224

1225

1226 **Figure 1- Supplemental Table. Electrophysiological parameters of current clamp recordings from**
1227 **neuronal cultures.**
1228
1229

	Glutamatergic			**FS GABAergic**			**NFS GABAergic**		
	WT	YH-HET		WT	YH-HET		WT	YH-HET	
	N = 9	N = 9		N = 9	N = 9		N = 9	N = 9	
	n = 27	n = 30	p-value	n = 27	n = 29	p-value	n = 26	n = 22	p-value
V_{rest} (mV)	-57.9±1.6	-57.0±1.7	0.61	-53.8±1.8	-52.8±1.8	0.60	-56.3±1.8	-54.4±1.9	0.34
R_{in} (MΩ)	177±17	182±16	0.80	95±9	105±10	0.40	171±16	146±14	0.19
Tau (ms)	32.9±3.8	39.3±4.3	0.14	17.3±2.0	16.7±1.9	0.75	24.9±2.9	22.2±2.7	0.37
C_m (pF)	198±15	215±16	0.23	183±14	163±12	0.15	143±11	164±13	0.09
Rheo (pA)	171±19	148±16	0.25	400±45	415±47	0.78	196±22	297±36	**0.005**
AP_{thresh} (mV)	-28.2±1.5	28.3±1.5	0.93	-25.7±1.6	-25.8±1.6	0.95	-28.2±1.6	-24.4±1.7	**0.012**
AP_{amp} (mV)	77.8±2.0	77.5±1.5	0.51	70.9±1.8	67.8±1.7	0.15	71.5±1.8	68.7±1.9	0.28
AP_{hw} (ms)	2.19±0.12	2.20±0.12	0.95	0.89±0.05	0.91±0.05	0.85	1.36±0.08	1.11±0.07	**0.01**
AHP (mV)	11.8±0.6	11.8±0.6	0.96	27.5±1.3	26.9±1.4	0.78	19.3±1.0	22.6±1.2	**0.034**
AP_{mfr} (Hz)	22.4±2.3	22.4±2.4	0.99	68.8±6.2	71.4±6.6	0.53	35.0±3.8	31.8±3.5	0.25

1230 For an explanation of the parameters, see Methods. R_{in} = input resistance, Tau = membrane time
1231 constant, Rheo = rheobase current, C_m = membrane capacitance, AP = action potential, thresh =
1232 threshold, amp = amplitude, hw = half width, AHP = afterhyperpolarization, and mfr = maximum firing
1233 rate. Values shown are estimated marginal means ± the standard error as determined by implementing
1234 a Generalized Linear Mixed Model. P values less than 0.05 are in red, bold type. For each subgroup, N
1235 values are the number of mouse pups, and n values are the number of neurons.

1236

1237

1238

1239

1240

1241 **Figure 4- Supplemental Table. Electrophysiological parameters of current clamp recordings from**
1242 **neuronal cultures of three major GABAergic subtypes.**
1243
1244
1245

	SST$^+$ GABAergic			**VIP$^+$ GABAergic**			**PV$^+$ GABAergic**		
	WT	YH-HET		WT	YH-HET		WT	YH-HET	
	N = 4	N = 5		N = 3	N = 4		N = 3	N = 4	
	n = 45	n = 46	p-value	n = 50	n = 48	p-value	n = 23	n = 25	p-value
R_{in} (MΩ)	133±18	95±13	**0.001**	243±10	249±11	0.645	67±4	66±3	0.850
Tau (ms)	16.9±1.1	13.5±0.8	**0.012**	35.1±2.4	33.1±2.3	0.384	6.7±0.5	6.0±0.4	0.302
C_m (pF)	135±13	152±15	**0.032**	148±6	134±6	0.055	103±5	90±4	0.050
Rheo (pA)	232±41	319±56	**0.001**	149±12	157±13	0.344	546±33	441±24	**0.031**
AP_{thresh} (mV)	-36.4±0.8	-35.2±0.8	0.113	-30.9±0.4	-31.0±0.4	0.850	-34.2±1.8	-35.5±1.9	0.308
AP_{amp} (mV)	79.9±1.5	80.2±1.5	0.850	75.6±0.9	75.5±0.9	0.943	77.6±1.0	82.7±1.0	**0.002**
AP_{hw} (ms)	0.91±0.02	0.86±0.02	0.142	1.09±0.04	1.09±0.04	0.916	0.73±0.03	0.69±0.02	0.180
AHP (mV)	23.0±0.7	23.5±0.7	0.554	17.2±0.9	17.4±0.9	0.860	26.6±0.6	25.3±0.5	0.150
AP_{mfr} (Hz)	57.6±5.1	55.7±4.9	0.432	35.5±2.8	35.9±2.8	0.857	69.4±4.9	79.0±5.3	0.068

1246

1247 For an explanation of the parameters, see Methods. R_{in} = input resistance, Tau = membrane time
1248 constant, Rheo = rheobase current, C_m = membrane capacitance, AP = action potential, thresh =
1249 threshold, amp = amplitude, hw = half width, AHP = afterhyperpolarization, and mfr = maximum firing
1250 rate. Values shown are estimated marginal means ± the standard error as determined by implementing
1251 a Generalized Linear Mixed Model. P values less than 0.05 are in red, bold type. For each subgroup, N
1252 values are the number of mouse pups, and n values are the number of neurons.

1253
1254
1255
1256
1257
1258
1259
1260
1261
1262
1263

1264

1265

1266 **Figure 6- Supplemental Table. Electrophysiological parameters using compartmental model neurons.**

Model neuron	Input Resistance (MΩ)	p-value vs 40 mM	Rheobase (pA)	p-value vs 40 mM	AP rate at 1.5x Rheobase (Hz)	p-value vs 40 mM
VIP-40 mM	266.5 ± 28.2		78.7 ± 3.7		7.0 ± 0.7	
VIP-35 mM	266.2 ± 28.1	0.193	79.1 ± 3.6	0.177	7.0 ± 0.7	0.999
VIP-30 mM	264.8 ± 28.0	0.012	80.4 ± 3.5	0.014	6.9 ± 0.7	0.527
VIP-30 mM + SST	260.2 ± 27.8	<0.001	86.3 ± 3.8	<0.001	6.5 ± 0.8	0.011
SST-40 mM	210.3 ± 23.0		127.5 ± 8.5		17.3 ± 2.1	
SST-35 mM	199.9 ± 22.1	0.009	156.3 ± 11.7	<0.001	11.9 ± 2.0	0.025
SST-30 mM	187.1 ± 21.2	0.001	180.0 ± 12.3	<0.001	7.1 ± 1.9	0.003
PV-40 mM	105.8 ± 7.7		258.0 ± 7.5		18.3 ± 1.3	
PV-35 mM	105.5 ± 7.7	0.140	264.5 ± 7.9	0.004	16.8 ± 1.4	0.033
PV-30 mM	103.3 ± 7.5	<0.001	273.0 ± 9.5	0.004	12.4 ± 2.0	0.004
PV-35 mM + I_{NaP}	104.6 ± 7.5	<0.001	238.5 6.3	<0.001	21.1 ± 1.3	<0.001
PV-30 mM + I_{NaP}	103.4 ± 7.4	0.009	250.5 ± 6.9	0.002	20.1 ± 1.5	0.012
Glut-40 mM	147.1 ± 12.0		117.0 ± 10.4		2.46 ± 0.3	
Glut-30 mM	146.4 ± 12.1	0.017	121.5 ± 10.0	<0.001	2.36 ± 0.4	0.593
Glut-30 mM + SST	140.4 ± 11.9	0.001	146.0 ± 9.7	<0.001	1.54 ± 0.3	0.012

1267

1268

1269

1270 For an explanation of the parameters, see Methods. AP = action potential. For each subgroup, 10 model
1271 neurons were used and simulations were repeated with the EC_{50} (in mM) for Na^+ for the KCNT1
1272 conductance set at the indicated levels. "+ SST" refers to the activation curve parameters (V_{50} and slope)
1273 for the KCNT1 conductance in that neuron type being replaced with those measured in SST neurons.
1274 Values shown are means ± the standard error. The statistical test is a repeated measures ANOVA.

1275

1276

1277

1278

1279

1280

REFERENCES

Alcami, P., & Pereda, A. E. (2019). Beyond plasticity: the dynamic impact of electrical synapses on neural circuits. *Nat Rev Neurosci*, *20*(5), 253-271. https://doi.org/10.1038/s41583-019-0133-5

Amitai, Y., Gibson, J. R., Beierlein, M., Patrick, S. L., Ho, A. M., Connors, B. W., & Golomb, D. (2002). The spatial dimensions of electrically coupled networks of interneurons in the neocortex. *J Neurosci*, *22*(10), 4142-4152. https://doi.org/10.1523/JNEUROSCI.22-10-04142.2002

Avermann, M., Tomm, C., Mateo, C., Gerstner, W., & Petersen, C. C. (2012). Microcircuits of excitatory and inhibitory neurons in layer 2/3 of mouse barrel cortex. *J Neurophysiol*, *107*(11), 3116-3134. https://doi.org/10.1152/jn.00917.2011

Barcia, G., Fleming, M. R., Deligniere, A., Gazula, V. R., Brown, M. R., Langouet, M., Chen, H., Kronengold, J., Abhyankar, A., Cilio, R., Nitschke, P., Kaminska, A., Boddaert, N., Casanova, J. L., Desguerre, I., Munnich, A., Dulac, O., Kaczmarek, L. K., Colleaux, L., & Nabbout, R. (2012). De novo gain-of-function KCNT1 channel mutations cause malignant migrating partial seizures of infancy. *Nat Genet*, *44*(11), 1255-1259. https://doi.org/10.1038/ng.2441

Berg, A. P., Sen, N., & Bayliss, D. A. (2007). TrpC3/C7 and Slo2.1 are molecular targets for metabotropic glutamate receptor signaling in rat striatal cholinergic interneurons. *J Neurosci*, *27*(33), 8845-8856. https://doi.org/10.1523/JNEUROSCI.0551-07.2007

Bhattacharjee, A., Gan, L., & Kaczmarek, L. K. (2002). Localization of the Slack potassium channel in the rat central nervous system. *J Comp Neurol*, *454*(3), 241-254. https://doi.org/10.1002/cne.10439

Bonardi, C. M., Heyne, H. O., Fiannacca, M., Fitzgerald, M. P., Gardella, E., Gunning, B., Olofsson, K., Lesca, G., Verbeek, N., Stamberger, H., Striano, P., Zara, F., Mancardi, M. M., Nava, C., Syrbe, S., Buono, S., Baulac, S., Coppola, A., Weckhuysen, S., . . . Rubboli, G. (2021). KCNT1-related epilepsies and epileptic encephalopathies: phenotypic and mutational spectrum. *Brain*, *144*(12), 3635-3650. https://doi.org/10.1093/brain/awab219

Budelli, G., Hage, T. A., Wei, A., Rojas, P., Jong, Y. J., O'Malley, K., & Salkoff, L. (2009). Na+-activated K+ channels express a large delayed outward current in neurons during normal physiology. *Nat Neurosci*, *12*(6), 745-750. https://doi.org/10.1038/nn.2313

Casale, A. E., Foust, A. J., Bal, T., & McCormick, D. A. (2015). Cortical Interneuron Subtypes Vary in Their Axonal Action Potential Properties. *J Neurosci*, *35*(47), 15555-15567. https://doi.org/10.1523/JNEUROSCI.1467-13.2015

Chen, H., Kronengold, J., Yan, Y., Gazula, V. R., Brown, M. R., Ma, L., Ferreira, G., Yang, Y., Bhattacharjee, A., Sigworth, F. J., Salkoff, L., & Kaczmarek, L. K. (2009). The N-terminal domain of Slack determines the formation and trafficking of Slick/Slack heteromeric sodium-activated potassium channels. *J Neurosci*, *29*(17), 5654-5665. https://doi.org/10.1523/JNEUROSCI.5978-08.2009

Cole, B. A., Pilati, N., & Lippiat, J. D. (2021). Epilepsy-causing KCNT1 variants increase K_{Na}1.1 channel activity by disrupting the activation gate. *bioRxiv*, 2021.2009.2016.460601. https://doi.org/10.1101/2021.09.16.460601

Connors, B. W. (2017). Synchrony and so much more: Diverse roles for electrical synapses in neural circuits. *Dev Neurobiol*, *77*(5), 610-624. https://doi.org/10.1002/dneu.22493

Davis, G. W. (2013). Homeostatic signaling and the stabilization of neural function. *Neuron*, *80*(3), 718-728. https://doi.org/10.1016/j.neuron.2013.09.044

Debanne, D., Inglebert, Y., & Russier, M. (2019). Plasticity of intrinsic neuronal excitability. *Curr Opin Neurobiol*, *54*, 73-82. https://doi.org/10.1016/j.conb.2018.09.001

Debanne, D., & Russier, M. (2019). The contribution of ion channels in input-output plasticity. *Neurobiol Learn Mem*, *166*, 107095. https://doi.org/10.1016/j.nlm.2019.107095

Dilena, R., DiFrancesco, J. C., Soldovieri, M. V., Giacobbe, A., Ambrosino, P., Mosca, I., Galli, M. A., Guez, S., Fumagalli, M., Miceli, F., Cattaneo, D., Darra, F., Gennaro, E., Zara, F., Striano, P., Castellotti, B., Gellera, C., Varesio, C., Veggiotti, P., & Taglialatela, M. (2018). Early Treatment with Quinidine in 2 Patients with Epilepsy of Infancy with Migrating Focal Seizures (EIMFS) Due to Gain-of-Function KCNT1 Mutations: Functional Studies, Clinical Responses, and Critical Issues for Personalized Therapy. *Neurotherapeutics*, *15*(4), 1112-1126. https://doi.org/10.1007/s13311-018-0657-9

Dudok, B., Klein, P. M., & Soltesz, I. (2022). Toward Understanding the Diverse Roles of Perisomatic Interneurons in Epilepsy. *Epilepsy Curr*, *22*(1), 54-60. https://doi.org/10.1177/15357597211053687

Edelstein, A. D., Tsuchida, M. A., Amodaj, N., Pinkard, H., Vale, R. D., & Stuurman, N. (2014). Advanced methods of microscope control using muManager software. *J Biol Methods*, *1*(2). https://doi.org/10.14440/jbm.2014.36

Evely, K. M., Pryce, K. D., Bausch, A. E., Lukowski, R., Ruth, P., Haj-Dahmane, S., & Bhattacharjee, A. (2017). Slack K(Na) Channels Influence Dorsal Horn Synapses and Nociceptive Behavior. *Mol Pain*, *13*, 1744806917714342. https://doi.org/10.1177/1744806917714342

Favero, M., Sotuyo, N. P., Lopez, E., Kearney, J. A., & Goldberg, E. M. (2018). A Transient Developmental Window of Fast-Spiking Interneuron Dysfunction in a Mouse Model of Dravet Syndrome. *J Neurosci*, *38*(36), 7912-7927. https://doi.org/10.1523/JNEUROSCI.0193-18.2018

Gertler, T. S., Cherian, S., DeKeyser, J. M., Kearney, J. A., & George, A. L., Jr. (2022). K(Na)1.1 gain-of-function preferentially dampens excitability of murine parvalbumin-positive interneurons. *Neurobiol Dis*, *168*, 105713. https://doi.org/10.1016/j.nbd.2022.105713

Gertler, T. S., Thompson, C. H., Vanoye, C. G., Millichap, J. J., & George, A. L., Jr. (2019). Functional consequences of a KCNT1 variant associated with status dystonicus and early-onset infantile encephalopathy. *Ann Clin Transl Neurol*, *6*(9), 1606-1615. https://doi.org/10.1002/acn3.50847

Gibson, J. R., Beierlein, M., & Connors, B. W. (1999). Two networks of electrically coupled inhibitory neurons in neocortex. *Nature*, *402*(6757), 75-79. https://doi.org/10.1038/47035

Gibson, J. R., Beierlein, M., & Connors, B. W. (2005). Functional properties of electrical synapses between inhibitory interneurons of neocortical layer 4. *J Neurophysiol*, *93*(1), 467-480. https://doi.org/10.1152/jn.00520.2004

Hage, T. A., & Salkoff, L. (2012). Sodium-activated potassium channels are functionally coupled to persistent sodium currents. *J Neurosci*, *32*(8), 2714-2721. https://doi.org/10.1523/JNEUROSCI.5088-11.2012

Halabisky, B., Parada, I., Buckmaster, P. S., & Prince, D. A. (2010). Excitatory input onto hilar somatostatin interneurons is increased in a chronic model of epilepsy. *J Neurophysiol*, *104*(4), 2214-2223. https://doi.org/10.1152/jn.00147.2010

Hedrich, U. B., Liautard, C., Kirschenbaum, D., Pofahl, M., Lavigne, J., Liu, Y., Theiss, S., Slotta, J., Escayg, A., Dihne, M., Beck, H., Mantegazza, M., & Lerche, H. (2014). Impaired action potential initiation in GABAergic interneurons causes hyperexcitable networks in an epileptic mouse model carrying a human Na(V)1.1 mutation. *J Neurosci*, *34*(45), 14874-14889. https://doi.org/10.1523/JNEUROSCI.0721-14.2014

Heron, S. E., Smith, K. R., Bahlo, M., Nobili, L., Kahana, E., Licchetta, L., Oliver, K. L., Mazarib, A., Afawi, Z., Korczyn, A., Plazzi, G., Petrou, S., Berkovic, S. F., Scheffer, I. E., & Dibbens, L. M. (2012). Missense mutations in the sodium-gated potassium channel gene KCNT1 cause severe autosomal dominant nocturnal frontal lobe epilepsy. *Nat Genet*, *44*(11), 1188-1190. https://doi.org/10.1038/ng.2440

Hinckley, C. A., Zhu, Z., Chu, J. H., Gubbels, C., Danker, T., Cherry, J. J., Whelan, C. D., Engle, S. J., & Nguyen, V. (2023). Functional evaluation of epilepsy associated KCNT1 variants in multiple

1375 cellular systems reveals a predominant gain of function impact on channel properties. *Epilepsia*.
1376 https://doi.org/10.1111/epi.17648
1377 Hu, H., & Agmon, A. (2015). Properties of precise firing synchrony between synaptically coupled cortical
1378 interneurons depend on their mode of coupling. *J Neurophysiol*, *114*(1), 624-637.
1379 https://doi.org/10.1152/jn.00304.2015
1380 Issa, N. P., Nunn, K. C., Wu, S., Haider, H. A., & Tao, J. X. (2023). Putative roles for homeostatic plasticity
1381 in epileptogenesis. *Epilepsia*, *64*(3), 539-552. https://doi.org/10.1111/epi.17500
1382 Joiner, W. J., Tang, M. D., Wang, L. Y., Dworetzky, S. I., Boissard, C. G., Gan, L., Gribkoff, V. K., &
1383 Kaczmarek, L. K. (1998). Formation of intermediate-conductance calcium-activated potassium
1384 channels by interaction of Slack and Slo subunits. *Nat Neurosci*, *1*(6), 462-469.
1385 https://doi.org/10.1038/2176
1386 Kim, G. E., Kronengold, J., Barcia, G., Quraishi, I. H., Martin, H. C., Blair, E., Taylor, J. C., Dulac, O.,
1387 Colleaux, L., Nabbout, R., & Kaczmarek, L. K. (2014). Human slack potassium channel mutations
1388 increase positive cooperativity between individual channels. *Cell Rep*, *9*(5), 1661-1672.
1389 https://doi.org/10.1016/j.celrep.2014.11.015
1390 Kuchenbuch, M., Nabbout, R., Yochum, M., Sauleau, P., Modolo, J., Wendling, F., & Benquet, P. (2021).
1391 In silico model reveals the key role of GABA in KCNT1-epilepsy in infancy with migrating focal
1392 seizures. *Epilepsia*, *62*(3), 683-697. https://doi.org/10.1111/epi.16834
1393 Lane, B. J., Samarth, P., Ransdell, J. L., Nair, S. S., & Schulz, D. J. (2016). Synergistic plasticity of intrinsic
1394 conductance and electrical coupling restores synchrony in an intact motor network. *Elife*, *5*.
1395 https://doi.org/10.7554/eLife.16879
1396 Large, A. M., Kunz, N. A., Mielo, S. L., & Oswald, A. M. (2016). Inhibition by Somatostatin Interneurons in
1397 Olfactory Cortex. *Front Neural Circuits*, *10*, 62. https://doi.org/10.3389/fncir.2016.00062
1398 Lignani, G., Baldelli, P., & Marra, V. (2020). Homeostatic Plasticity in Epilepsy. *Front Cell Neurosci*, *14*,
1399 197. https://doi.org/10.3389/fncel.2020.00197
1400 Liu, Y., Zhang, F. F., Song, Y., Wang, R., Zhang, Q., Shen, Z. S., Zhang, F. F., Zhong, D. Y., Wang, X. H., Guo,
1401 Q., Tang, Q. Y., & Zhang, Z. (2022). The Slack Channel Deletion Causes Mechanical Pain
1402 Hypersensitivity in Mice. *Front Mol Neurosci*, *15*, 811441.
1403 https://doi.org/10.3389/fnmol.2022.811441
1404 Lu, R., Bausch, A. E., Kallenborn-Gerhardt, W., Stoetzer, C., Debruin, N., Ruth, P., Geisslinger, G., Leffler,
1405 A., Lukowski, R., & Schmidtko, A. (2015). Slack channels expressed in sensory neurons control
1406 neuropathic pain in mice. *J Neurosci*, *35*(3), 1125-1135.
1407 https://doi.org/10.1523/JNEUROSCI.2423-14.2015
1408 Ma, Y., Hu, H., Berrebi, A. S., Mathers, P. H., & Agmon, A. (2006). Distinct subtypes of somatostatin-
1409 containing neocortical interneurons revealed in transgenic mice. *J Neurosci*, *26*(19), 5069-5082.
1410 https://doi.org/10.1523/JNEUROSCI.0661-06.2006
1411 Magloire, V., Mercier, M. S., Kullmann, D. M., & Pavlov, I. (2019). GABAergic Interneurons in Seizures:
1412 Investigating Causality With Optogenetics. *Neuroscientist*, *25*(4), 344-358.
1413 https://doi.org/10.1177/1073858418805002
1414 Makinson, C. D., Dutt, K., Lin, F., Papale, L. A., Shankar, A., Barela, A. J., Liu, R., Goldin, A. L., & Escayg, A.
1415 (2016). An Scn1a epilepsy mutation in Scn8a alters seizure susceptibility and behavior. *Exp*
1416 *Neurol*, *275 Pt 1*(0 1), 46-58. https://doi.org/10.1016/j.expneurol.2015.09.008
1417 Marder, E., & Goaillard, J. M. (2006). Variability, compensation and homeostasis in neuron and network
1418 function. *Nat Rev Neurosci*, *7*(7), 563-574. https://doi.org/10.1038/nrn1949
1419 Markram, H., Muller, E., Ramaswamy, S., Reimann, M. W., Abdellah, M., Sanchez, C. A., Ailamaki, A.,
1420 Alonso-Nanclares, L., Antille, N., Arsever, S., Kahou, G. A., Berger, T. K., Bilgili, A., Buncic, N.,
1421 Chalimourda, A., Chindemi, G., Courcol, J. D., Delalondre, F., Delattre, V., . . . Schurmann, F.

(2015). Reconstruction and Simulation of Neocortical Microcircuitry. *Cell*, *163*(2), 456-492. https://doi.org/10.1016/j.cell.2015.09.029

Martinez-Espinosa, P. L., Wu, J., Yang, C., Gonzalez-Perez, V., Zhou, H., Liang, H., Xia, X. M., & Lingle, C. J. (2015). Knockout of Slo2.2 enhances itch, abolishes KNa current, and increases action potential firing frequency in DRG neurons. *Elife*, *4*. https://doi.org/10.7554/eLife.10013

McTague, A., Nair, U., Malhotra, S., Meyer, E., Trump, N., Gazina, E. V., Papandreou, A., Ngoh, A., Ackermann, S., Ambegaonkar, G., Appleton, R., Desurkar, A., Eltze, C., Kneen, R., Kumar, A. V., Lascelles, K., Montgomery, T., Ramesh, V., Samanta, R., . . . Kurian, M. A. (2018). Clinical and molecular characterization of KCNT1-related severe early-onset epilepsy. *Neurology*, *90*(1), e55-e66. https://doi.org/10.1212/WNL.0000000000004762

Mikati, M. A., Jiang, Y. H., Carboni, M., Shashi, V., Petrovski, S., Spillmann, R., Milligan, C. J., Li, M., Grefe, A., McConkie, A., Berkovic, S., Scheffer, I., Mullen, S., Bonner, M., Petrou, S., & Goldstein, D. (2015). Quinidine in the treatment of KCNT1-positive epilepsies. *Ann Neurol*, *78*(6), 995-999. https://doi.org/10.1002/ana.24520

Milligan, C. J., Li, M., Gazina, E. V., Heron, S. E., Nair, U., Trager, C., Reid, C. A., Venkat, A., Younkin, D. P., Dlugos, D. J., Petrovski, S., Goldstein, D. B., Dibbens, L. M., Scheffer, I. E., Berkovic, S. F., & Petrou, S. (2014). KCNT1 gain of function in 2 epilepsy phenotypes is reversed by quinidine. *Ann Neurol*, *75*(4), 581-590. https://doi.org/10.1002/ana.24128

Oliva, A. A., Jr., Jiang, M., Lam, T., Smith, K. L., & Swann, J. W. (2000). Novel hippocampal interneuronal subtypes identified using transgenic mice that express green fluorescent protein in GABAergic interneurons. *J Neurosci*, *20*(9), 3354-3368. https://doi.org/10.1523/JNEUROSCI.20-09-03354.2000

Parker, P. R., Cruikshank, S. J., & Connors, B. W. (2009). Stability of electrical coupling despite massive developmental changes of intrinsic neuronal physiology. *J Neurosci*, *29*(31), 9761-9770. https://doi.org/10.1523/JNEUROSCI.4568-08.2009

Pratt, K. G., & Aizenman, C. D. (2007). Homeostatic regulation of intrinsic excitability and synaptic transmission in a developing visual circuit. *J Neurosci*, *27*(31), 8268-8277. https://doi.org/10.1523/JNEUROSCI.1738-07.2007

Quraishi, I. H., Stern, S., Mangan, K. P., Zhang, Y., Ali, S. R., Mercier, M. R., Marchetto, M. C., McLachlan, M. J., Jones, E. M., Gage, F. H., & Kaczmarek, L. K. (2019). An Epilepsy-Associated KCNT1 Mutation Enhances Excitability of Human iPSC-Derived Neurons by Increasing Slack KNa Currents. *J Neurosci*, *39*(37), 7438-7449. https://doi.org/10.1523/JNEUROSCI.1628-18.2019

Reijntjes, D. O. J., Lee, J. H., Park, S., Schubert, N. M. A., van Tuinen, M., Vijayakumar, S., Jones, T. A., Jones, S. M., Gratton, M. A., Xia, X. M., Yamoah, E. N., & Pyott, S. J. (2019). Sodium-activated potassium channels shape peripheral auditory function and activity of the primary auditory neurons in mice. *Sci Rep*, *9*(1), 2573. https://doi.org/10.1038/s41598-019-39119-z

Rizzi, S., Knaus, H. G., & Schwarzer, C. (2016). Differential distribution of the sodium-activated potassium channels slick and slack in mouse brain. *J Comp Neurol*, *524*(10), 2093-2116. https://doi.org/10.1002/cne.23934

Rizzo, F., Ambrosino, P., Guacci, A., Chetta, M., Marchese, G., Rocco, T., Soldovieri, M. V., Manocchio, L., Mosca, I., Casara, G., Vecchi, M., Taglialatela, M., Coppola, G., & Weisz, A. (2016). Characterization of two de novoKCNT1 mutations in children with malignant migrating partial seizures in infancy. *Mol Cell Neurosci*, *72*, 54-63. https://doi.org/10.1016/j.mcn.2016.01.004

Rudy, B., Fishell, G., Lee, S., & Hjerling-Leffler, J. (2011). Three groups of interneurons account for nearly 100% of neocortical GABAergic neurons. *Dev Neurobiol*, *71*(1), 45-61. https://doi.org/10.1002/dneu.20853

1468 Rush, A. M., Dib-Hajj, S. D., Liu, S., Cummins, T. R., Black, J. A., & Waxman, S. G. (2006). A single sodium
1469 channel mutation produces hyper- or hypoexcitability in different types of neurons. *Proc Natl*
1470 *Acad Sci U S A*, *103*(21), 8245-8250. https://doi.org/10.1073/pnas.0602813103
1471 Schindelin, J., Arganda-Carreras, I., Frise, E., Kaynig, V., Longair, M., Pietzsch, T., Preibisch, S., Rueden, C.,
1472 Saalfeld, S., Schmid, B., Tinevez, J. Y., White, D. J., Hartenstein, V., Eliceiri, K., Tomancak, P., &
1473 Cardona, A. (2012). Fiji: an open-source platform for biological-image analysis. *Nat Methods*,
1474 *9*(7), 676-682. https://doi.org/10.1038/nmeth.2019
1475 Shore, A. N., Colombo, S., Tobin, W. F., Petri, S., Cullen, E. R., Dominguez, S., Bostick, C. D., Beaumont, M.
1476 A., Williams, D., Khodagholy, D., Yang, M., Lutz, C. M., Peng, Y., Gelinas, J. N., Goldstein, D. B.,
1477 Boland, M. J., Frankel, W. N., & Weston, M. C. (2020). Reduced GABAergic neuron excitability,
1478 altered synaptic connectivity, and seizures in a KCNT1 gain-of-function mouse model of
1479 childhood epilepsy. *Cell Rep*.
1480 Soh, H., Park, S., Ryan, K., Springer, K., Maheshwari, A., & Tzingounis, A. V. (2018). Deletion of KCNQ2/3
1481 potassium channels from PV+ interneurons leads to homeostatic potentiation of excitatory
1482 transmission. *Elife*, *7*. https://doi.org/10.7554/eLife.38617
1483 Spitznagel, B. D., Mishra, N. M., Qunies, A. M., Prael, F. J., 3rd, Du, Y., Kozek, K. A., Lazarenko, R. M.,
1484 Denton, J. S., Emmitte, K. A., & Weaver, C. D. (2020). VU0606170, a Selective Slack Channels
1485 Inhibitor, Decreases Calcium Oscillations in Cultured Cortical Neurons. *ACS Chem Neurosci*,
1486 *11*(21), 3658-3671. https://doi.org/10.1021/acschemneuro.0c00583
1487 Staley, K. (2015). Molecular mechanisms of epilepsy. *Nat Neurosci*, *18*(3), 367-372.
1488 https://doi.org/10.1038/nn.3947
1489 Studtmann, C., Ladislav, M., Topolski, M. A., Safari, M., & Swanger, S. A. (2022). Na(V)1.1
1490 haploinsufficiency impairs glutamatergic and GABAergic neuron function in the thalamus.
1491 *Neurobiol Dis*, *167*, 105672. https://doi.org/10.1016/j.nbd.2022.105672
1492 Tai, C., Abe, Y., Westenbroek, R. E., Scheuer, T., & Catterall, W. A. (2014). Impaired excitability of
1493 somatostatin- and parvalbumin-expressing cortical interneurons in a mouse model of Dravet
1494 syndrome. *Proc Natl Acad Sci U S A*, *111*(30), E3139-3148.
1495 https://doi.org/10.1073/pnas.1411131111
1496 Tang, Q. Y., Zhang, F. F., Xu, J., Wang, R., Chen, J., Logothetis, D. E., & Zhang, Z. (2016). Epilepsy-Related
1497 Slack Channel Mutants Lead to Channel Over-Activity by Two Different Mechanisms. *Cell Rep*,
1498 *14*(1), 129-139. https://doi.org/10.1016/j.celrep.2015.12.019
1499 Taniguchi, H., He, M., Wu, P., Kim, S., Paik, R., Sugino, K., Kvitsiani, D., Fu, Y., Lu, J., Lin, Y., Miyoshi, G.,
1500 Shima, Y., Fishell, G., Nelson, S. B., & Huang, Z. J. (2011). A resource of Cre driver lines for
1501 genetic targeting of GABAergic neurons in cerebral cortex. *Neuron*, *71*(6), 995-1013.
1502 https://doi.org/10.1016/j.neuron.2011.07.026
1503 Ting, J. T., Daigle, T. L., Chen, Q., & Feng, G. (2014). Acute brain slice methods for adult and aging
1504 animals: application of targeted patch clamp analysis and optogenetics. *Methods Mol Biol*, *1183*,
1505 221-242. https://doi.org/10.1007/978-1-4939-1096-0_14
1506 Tran, C. H., Vaiana, M., Nakuci, J., Somarowthu, A., Goff, K. M., Goldstein, N., Murthy, P., Muldoon, S. F.,
1507 & Goldberg, E. M. (2020). Interneuron Desynchronization Precedes Seizures in a Mouse Model
1508 of Dravet Syndrome. *J Neurosci*, *40*(13), 2764-2775. https://doi.org/10.1523/JNEUROSCI.2370-
1509 19.2020
1510 Tremblay, R., Lee, S., & Rudy, B. (2016). GABAergic Interneurons in the Neocortex: From Cellular
1511 Properties to Circuits. *Neuron*, *91*(2), 260-292. https://doi.org/10.1016/j.neuron.2016.06.033
1512 Turrigiano, G. (2011). Too many cooks? Intrinsic and synaptic homeostatic mechanisms in cortical circuit
1513 refinement. *Annu Rev Neurosci*, *34*, 89-103. https://doi.org/10.1146/annurev-neuro-060909-
1514 153238

1515 Turrigiano, G. (2012). Homeostatic synaptic plasticity: local and global mechanisms for stabilizing
1516 neuronal function. *Cold Spring Harb Perspect Biol*, *4*(1), a005736.
1517 https://doi.org/10.1101/cshperspect.a005736
1518 Urban-Ciecko, J., & Barth, A. L. (2016). Somatostatin-expressing neurons in cortical networks. *Nat Rev*
1519 *Neurosci*, *17*(7), 401-409. https://doi.org/10.1038/nrn.2016.53
1520 Varghese, N., Moscoso, B., Chavez, A., Springer, K., Ortiz, E., Soh, H., Santaniello, S., Maheshwari, A., &
1521 Tzingounis, A. V. (2023). KCNQ2/3 Gain-of-Function Variants and Cell Excitability: Differential
1522 Effects in CA1 versus L2/3 Pyramidal Neurons. *J Neurosci*, *43*(38), 6479-6494.
1523 https://doi.org/10.1523/JNEUROSCI.0980-23.2023
1524 Wengert, E. R., Miralles, R. M., Wedgwood, K. C. A., Wagley, P. K., Strohm, S. M., Panchal, P. S., Idrissi, A.
1525 M., Wenker, I. C., Thompson, J. A., Gaykema, R. P., & Patel, M. K. (2021). Somatostatin-Positive
1526 Interneurons Contribute to Seizures in SCN8A Epileptic Encephalopathy. *J Neurosci*, *41*(44),
1527 9257-9273. https://doi.org/10.1523/JNEUROSCI.0718-21.2021
1528 Wu, J., Quraishi, I. H., Zhang, Y., Bromwich, M., & Kaczmarek, L. K. (2024). Disease-causing Slack
1529 potassium channel mutations produce opposite effects on excitability of excitatory and
1530 inhibitory neurons. *Cell Rep*, *43*(3), 113904. https://doi.org/10.1016/j.celrep.2024.113904
1531 Yang, J., & Prescott, S. A. (2023). Homeostatic regulation of neuronal function: importance of
1532 degeneracy and pleiotropy. *Front Cell Neurosci*, *17*, 1184563.
1533 https://doi.org/10.3389/fncel.2023.1184563
1534 Yu, F. H., Mantegazza, M., Westenbroek, R. E., Robbins, C. A., Kalume, F., Burton, K. A., Spain, W. J.,
1535 McKnight, G. S., Scheuer, T., & Catterall, W. A. (2006). Reduced sodium current in GABAergic
1536 interneurons in a mouse model of severe myoclonic epilepsy in infancy. *Nat Neurosci*, *9*(9),
1537 1142-1149. https://doi.org/10.1038/nn1754
1538 Zhang, J., Chen, X., Eaton, M., Wu, J., Ma, Z., Lai, S., Park, A., Ahmad, T. S., Que, Z., Lee, J. H., Xiao, T., Li,
1539 Y., Wang, Y., Olivero-Acosta, M. I., Schaber, J. A., Jayant, K., Yuan, C., Huang, Z., Lanman, N.
1540 A., . . . Yang, Y. (2021). Severe deficiency of the voltage-gated sodium channel Na(V)1.2 elevates
1541 neuronal excitability in adult mice. *Cell Rep*, *36*(5), 109495.
1542 https://doi.org/10.1016/j.celrep.2021.109495
1543 Zhang, Q., Gao, S. H., Shen, Z. S., Wang, Y., Hu, S. W., Duan, G. B., Liu, Y., Zhong, D. Y., Liu, J., Sun, M. H.,
1544 Zhang, X., Cao, T. Y., Cao, J. L., Tang, Q. Y., & Zhang, Z. (2022). The Slack Channel Regulates
1545 Anxiety-Like Behaviors via Basolateral Amygdala Glutamatergic Projections to Ventral
1546 Hippocampus. *J Neurosci*, *42*(14), 3049-3064. https://doi.org/10.1523/JNEUROSCI.2027-21.2022

1547

Figure 1

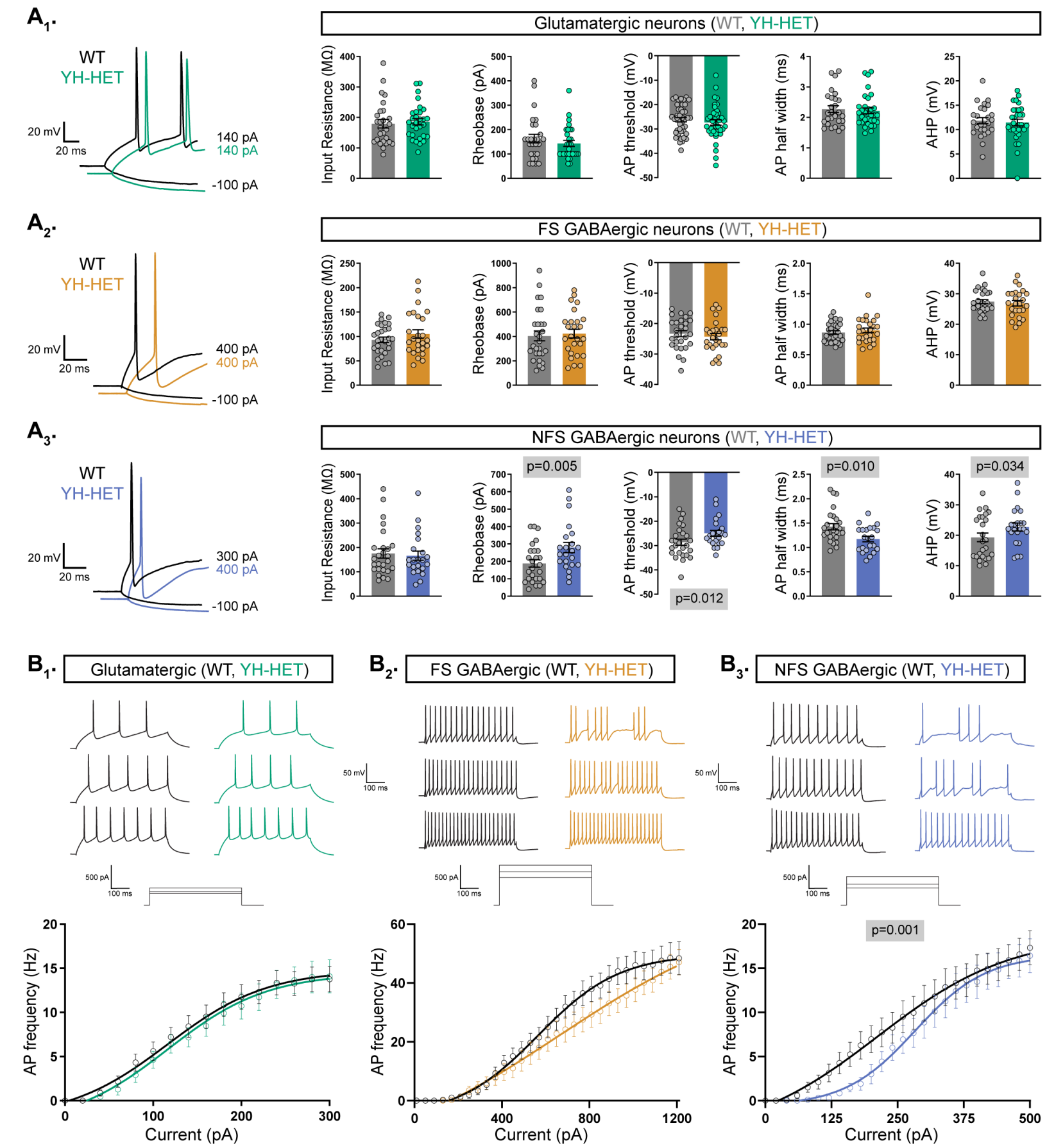
A1.
Glutamatergic neurons (WT, YH-HET)
WT
YH-HET
20 mV
20 ms
140 pA
140 pA
-100 pA
Input Resistance (MΩ)
Rheobase (pA)
AP threshold (mV)
AP half width (ms)
AHP (mV)
A2.
FS GABAergic neurons (WT, YH-HET)
WT
YH-HET
20 mV
20 ms
400 pA
400 pA
-100 pA
A3.
NFS GABAergic neurons (WT, YH-HET)
WT
YH-HET
20 mV
20 ms
300 pA
400 pA
-100 pA
p=0.005
p=0.012
p=0.010
p=0.034
B1.
Glutamatergic (WT, YH-HET)
B2.
FS GABAergic (WT, YH-HET)
B3.
NFS GABAergic (WT, YH-HET)
50 mV
100 ms
500 pA
100 ms
p=0.001
AP frequency (Hz)
Current (pA)

Figure 2

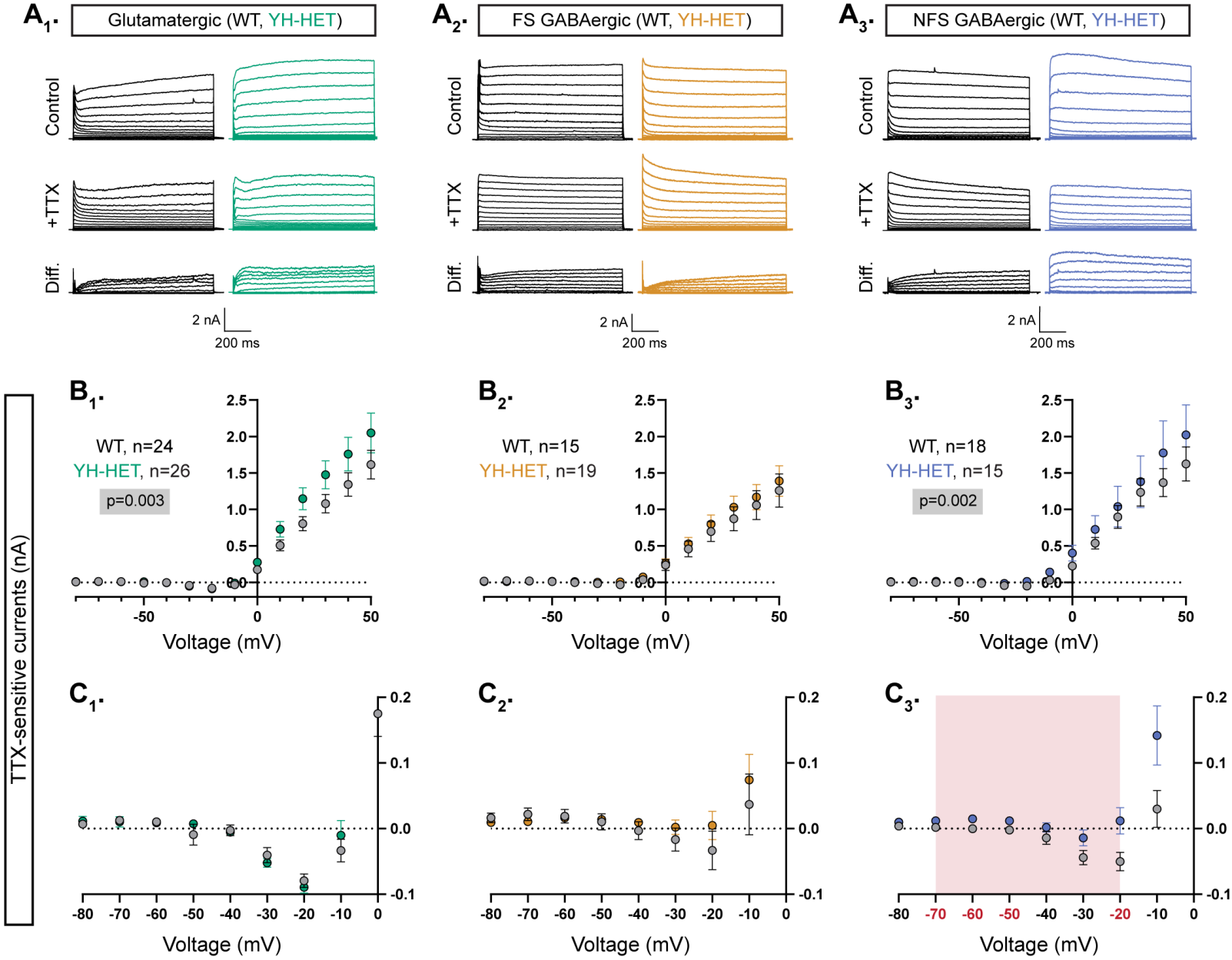
A1.
Glutamatergic (WT, YH-HET)
A2.
FS GABAergic (WT, YH-HET)
A3.
NFS GABAergic (WT, YH-HET)
Control
+TTX
Diff.
2 nA
200 ms
TTX-sensitive currents (nA)
B1.
WT, n=24
YH-HET, n=26
p=0.003
B2.
WT, n=15
YH-HET, n=19
B3.
WT, n=18
YH-HET, n=15
p=0.002
Voltage (mV)
C1.
C2.
C3.

Figure 3

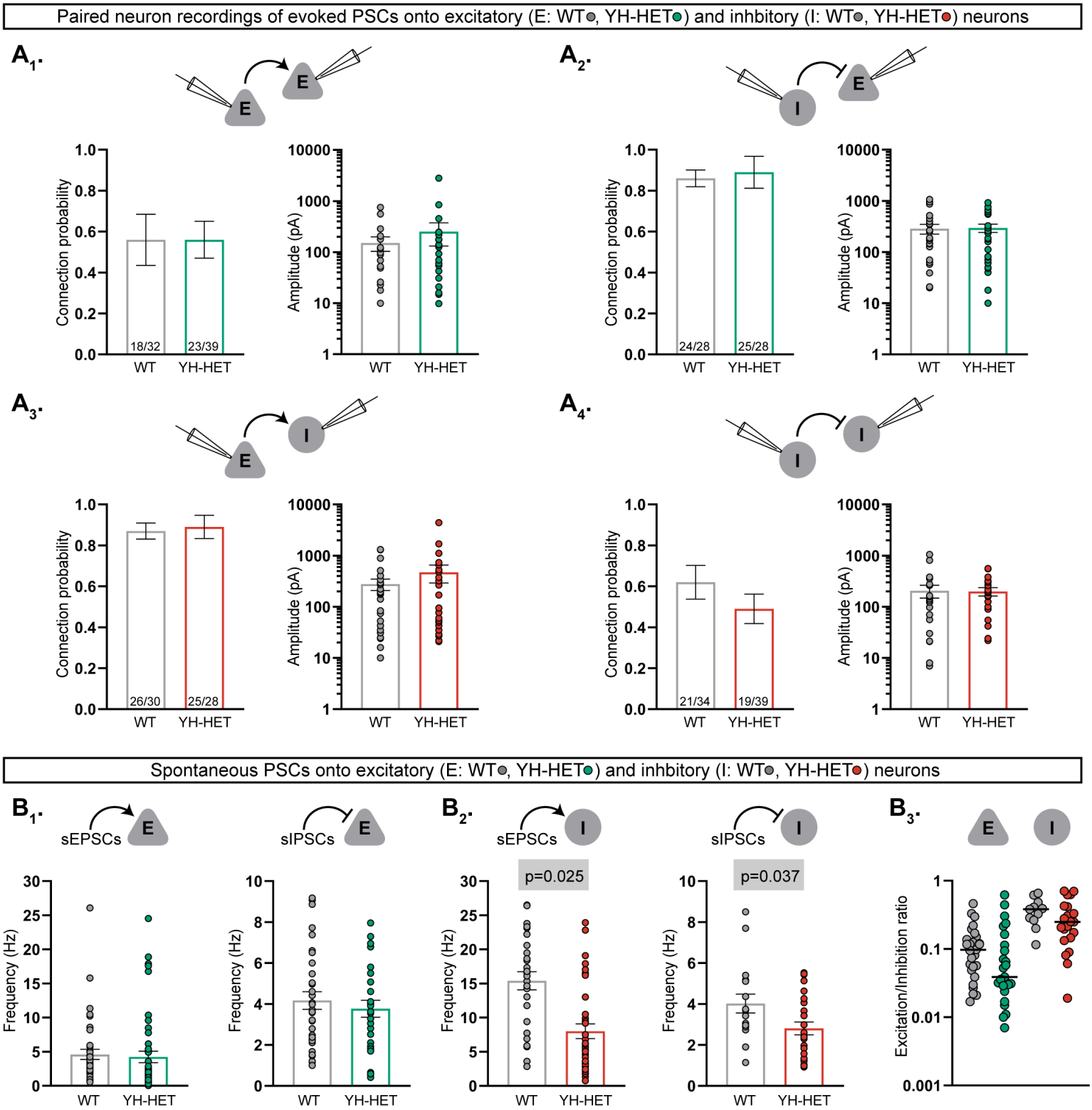
Paired neuron recordings of evoked PSCs onto excitatory (E: WT, YH-HET) and inhbitory (I: WT, YH-HET) neurons
A1.
A2.
A3.
A4.
E
I
Connection probability
Amplitude (pA)
18/32
23/39
24/28
25/28
26/30
25/28
21/34
19/39
WT
YH-HET
Spontaneous PSCs onto excitatory (E: WT, YH-HET) and inhbitory (I: WT, YH-HET) neurons
B1.
B2.
B3.
sEPSCs
sIPSCs
Frequency (Hz)
p=0.025
p=0.037
Excitation/Inhibition ratio

Figure 4

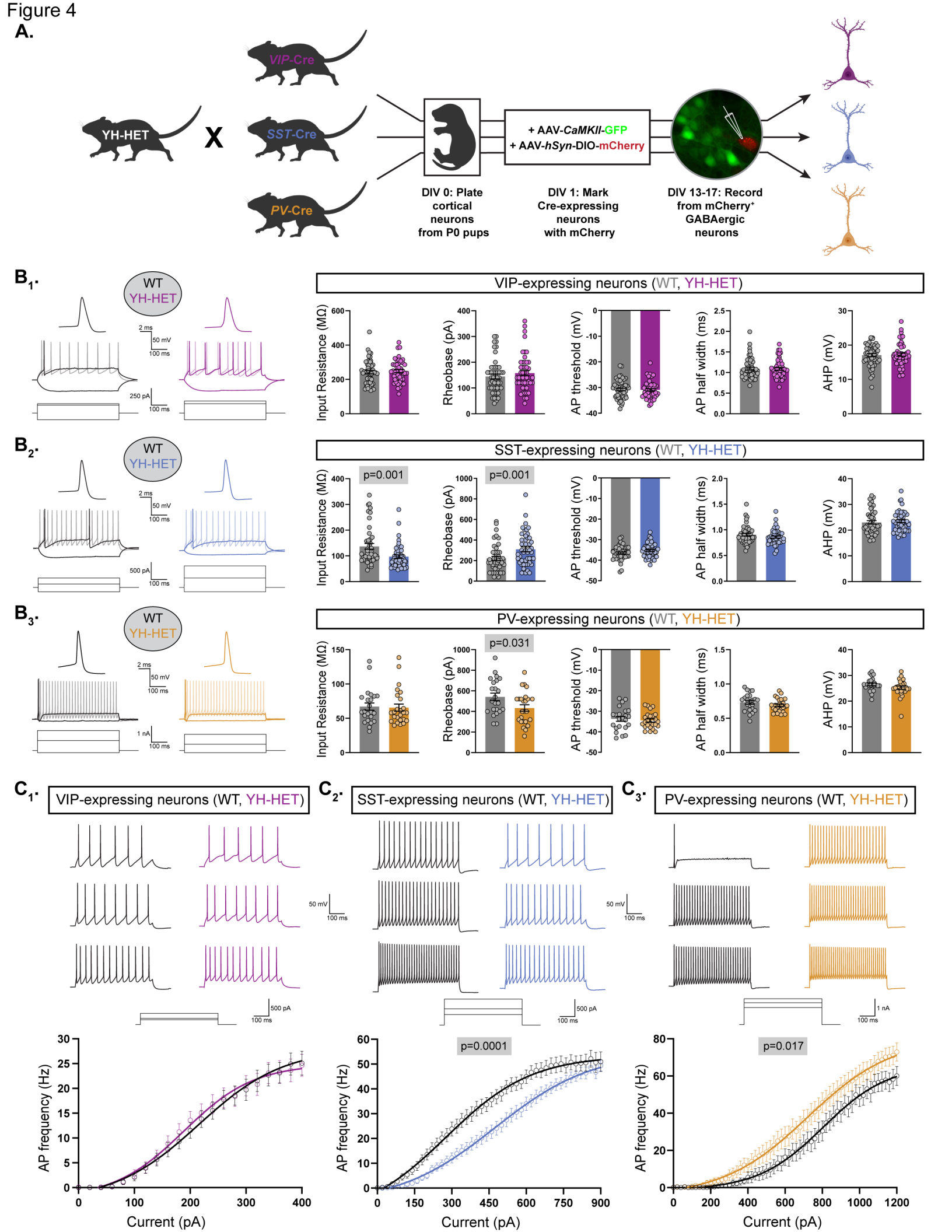
A.
YH-HET
X
VIP-Cre
SST-Cre
PV-Cre
+ AAV-CaMKII-GFP
+ AAV-hSyn-DIO-mCherry
DIV 0: Plate cortical neurons from P0 pups
DIV 1: Mark Cre-expressing neurons with mCherry
DIV 13-17: Record from mCherry+ GABAergic neurons
B1.
WT
YH-HET
VIP-expressing neurons (WT, YH-HET)
Input Resistance (MΩ)
Rheobase (pA)
AP threshold (mV)
AP half width (ms)
AHP (mV)
B2.
SST-expressing neurons (WT, YH-HET)
p=0.001
p=0.001
B3.
PV-expressing neurons (WT, YH-HET)
p=0.031
C1.
VIP-expressing neurons (WT, YH-HET)
C2.
SST-expressing neurons (WT, YH-HET)
C3.
PV-expressing neurons (WT, YH-HET)
AP frequency (Hz)
Current (pA)
p=0.0001
p=0.017

Figure 5

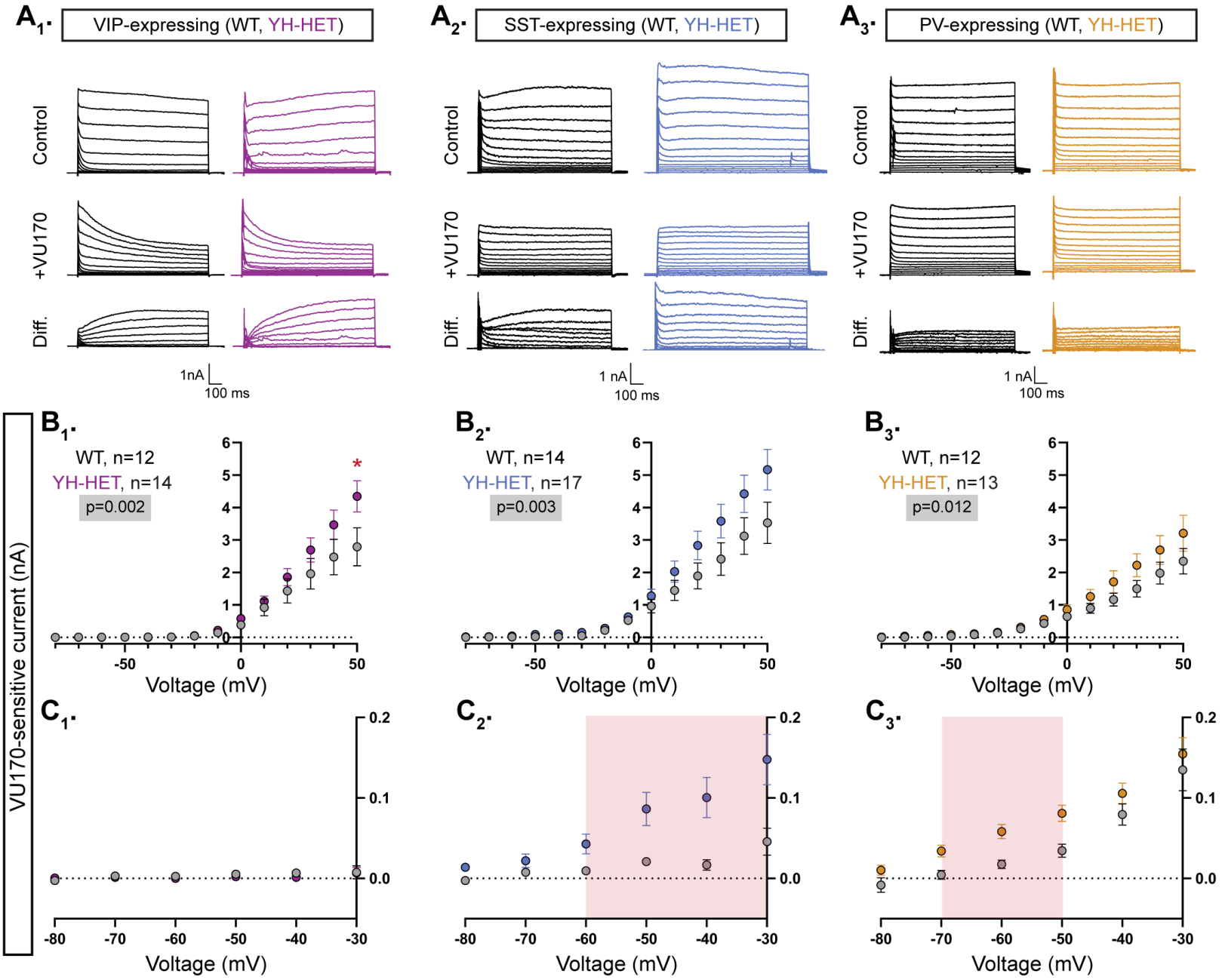
A1.
VIP-expressing (WT, YH-HET)
A2.
SST-expressing (WT, YH-HET)
A3.
PV-expressing (WT, YH-HET)
Control
+VU170
Diff.
1nA
100 ms
1 nA
100 ms
VU170-sensitive current (nA)
B1.
WT, n=12
YH-HET, n=14
p=0.002
B2.
WT, n=14
YH-HET, n=17
p=0.003
B3.
WT, n=12
YH-HET, n=13
p=0.012
Voltage (mV)
C1.
C2.
C3.

Figure 6

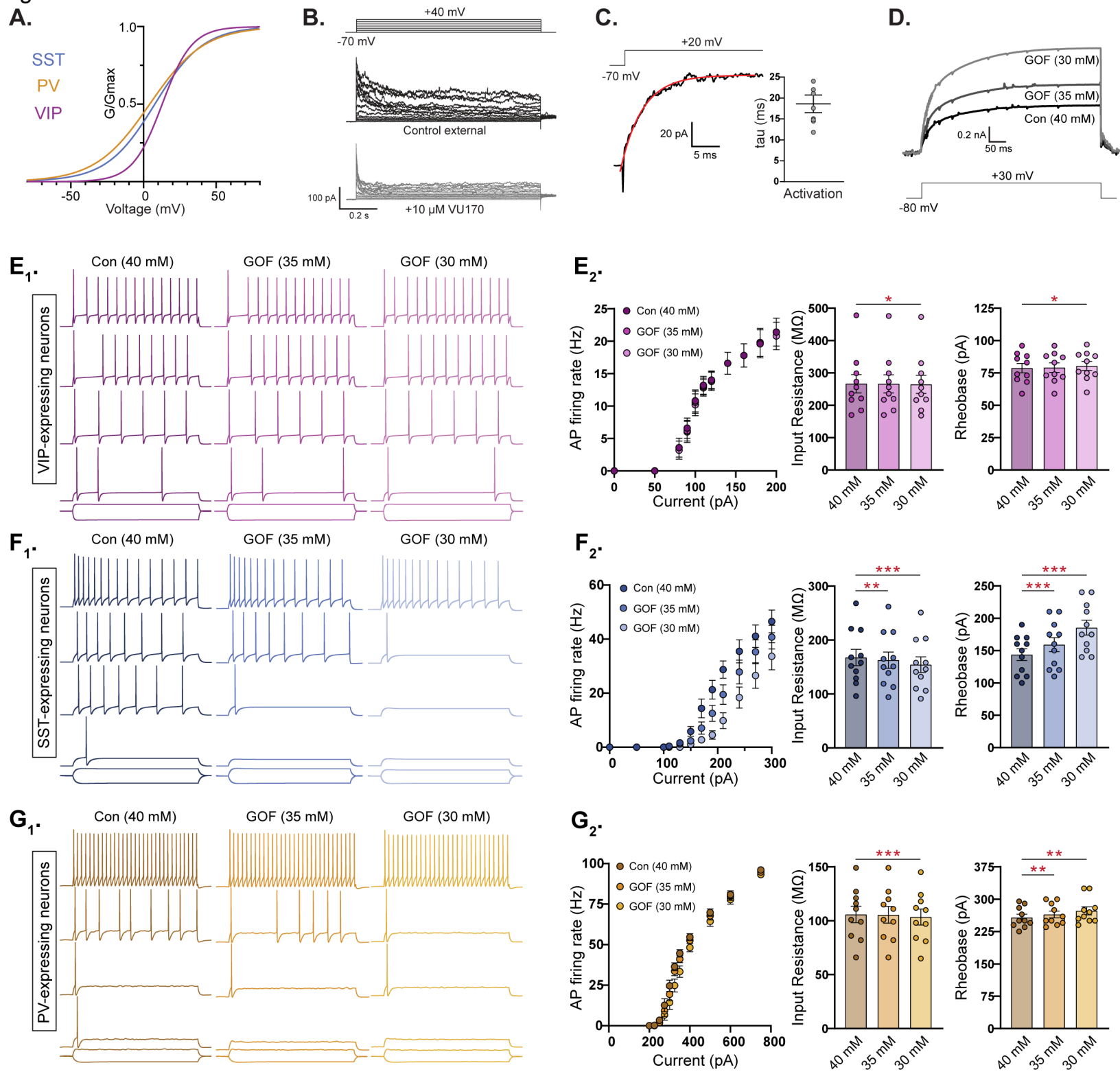
A.
SST
PV
VIP
G/Gmax
1.0
0.5
-50
0
50
Voltage (mV)
B.
+40 mV
-70 mV
Control external
100 pA
0.2 s
+10 μM VU170
C.
+20 mV
-70 mV
20 pA
5 ms
tau (ms)
Activation
D.
GOF (30 mM)
GOF (35 mM)
Con (40 mM)
0.2 nA
50 ms
+30 mV
-80 mV
E1.
Con (40 mM)
GOF (35 mM)
GOF (30 mM)
VIP-expressing neurons
E2.
AP firing rate (Hz)
Current (pA)
Input Resistance (MΩ)
Rheobase (pA)
40 mM
35 mM
30 mM
F1.
SST-expressing neurons
F2.
G1.
PV-expressing neurons
G2.

Figure 7

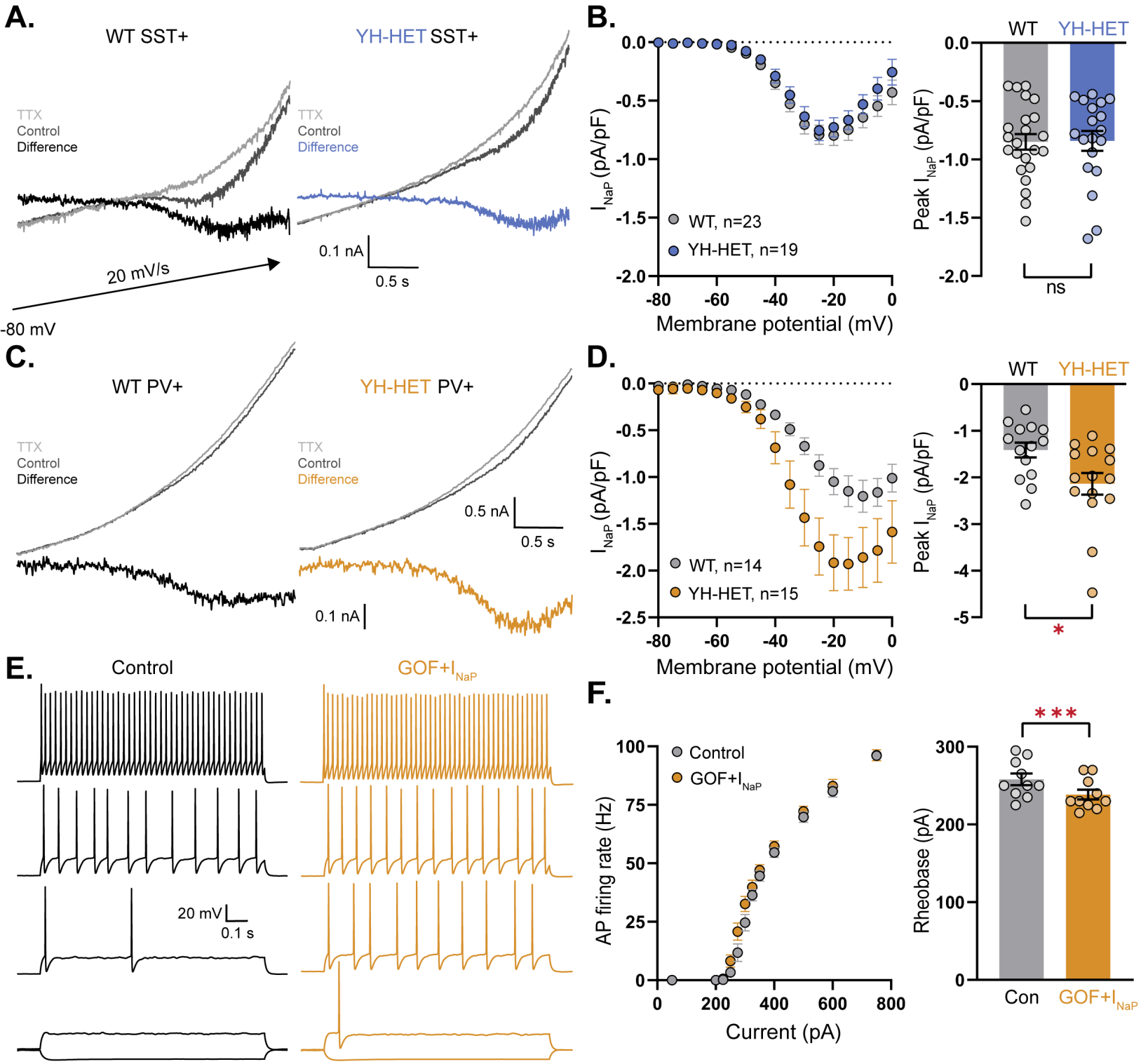
A.
WT SST+
YH-HET SST+
TTX
Control
Difference
20 mV/s
-80 mV
0.1 nA
0.5 s
B.
WT, n=23
YH-HET, n=19
Membrane potential (mV)
Peak I_NaP (pA/pF)
WT
YH-HET
ns
C.
WT PV+
YH-HET PV+
0.5 nA
0.5 s
0.1 nA
D.
WT, n=14
YH-HET, n=15
*
E.
Control
GOF+I_NaP
20 mV
0.1 s
F.
Control
GOF+I_NaP
AP firing rate (Hz)
Current (pA)
Rheobase (pA)
***
Con

Figure 8

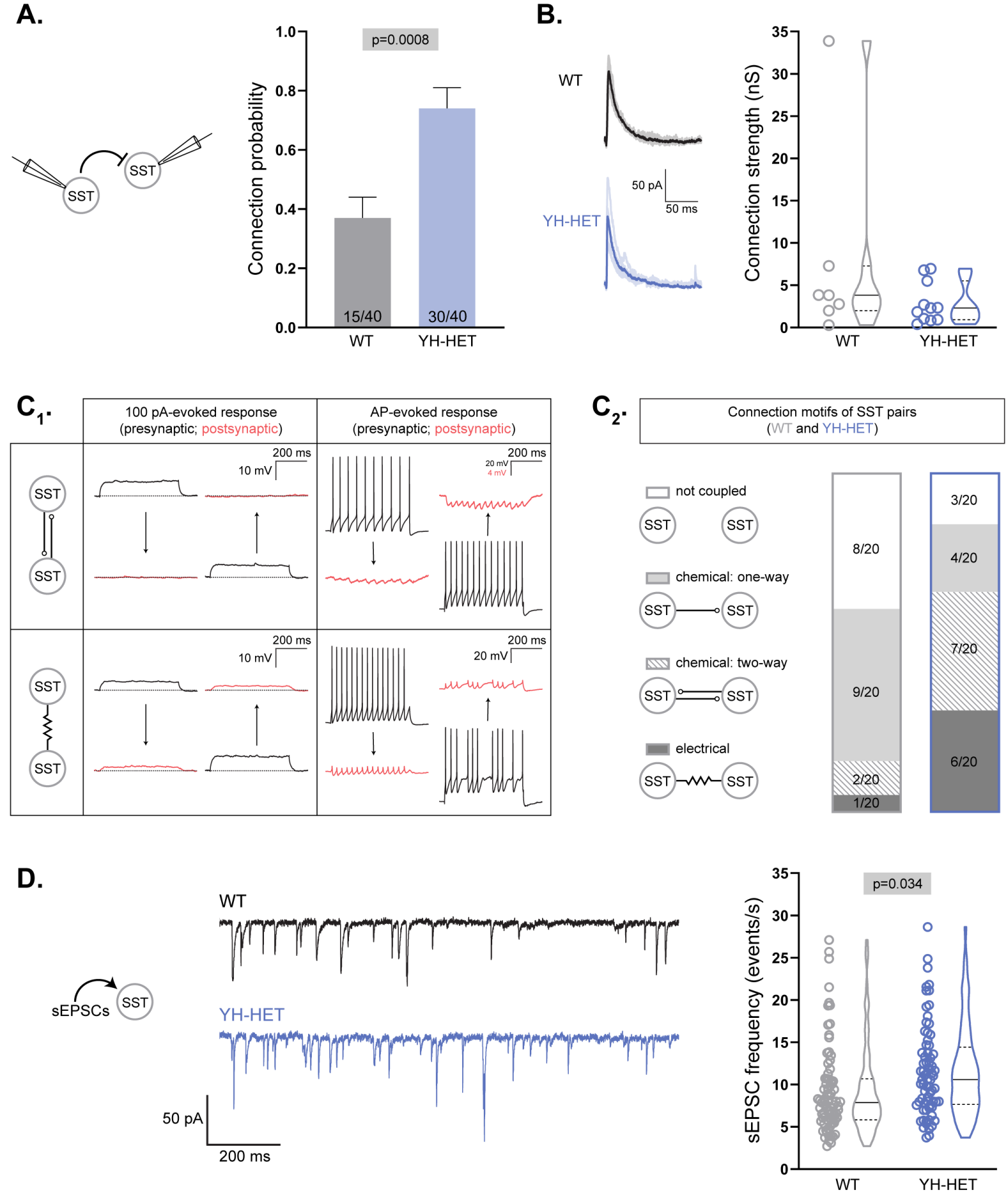
A.
SST
SST
p=0.0008
Connection probability
1.0
0.8
0.6
0.4
0.2
0.0
15/40
30/40
WT
YH-HET
B.
WT
YH-HET
50 pA
50 ms
Connection strength (nS)
35
30
25
20
15
10
5
0
WT
YH-HET
C1.
100 pA-evoked response
(presynaptic; postsynaptic)
AP-evoked response
(presynaptic; postsynaptic)
200 ms
10 mV
20 mV
4 mV
SST
SST
C2.
Connection motifs of SST pairs
(WT and YH-HET)
not coupled
chemical: one-way
chemical: two-way
electrical
8/20
9/20
2/20
1/20
3/20
4/20
7/20
6/20
D.
sEPSCs
SST
WT
YH-HET
50 pA
200 ms
p=0.034
sEPSC frequency (events/s)
35
30
25
20
15
10
5
0
WT
YH-HET

Figure 9

GFP-expressing GIN neurons (WT, YH-HET)

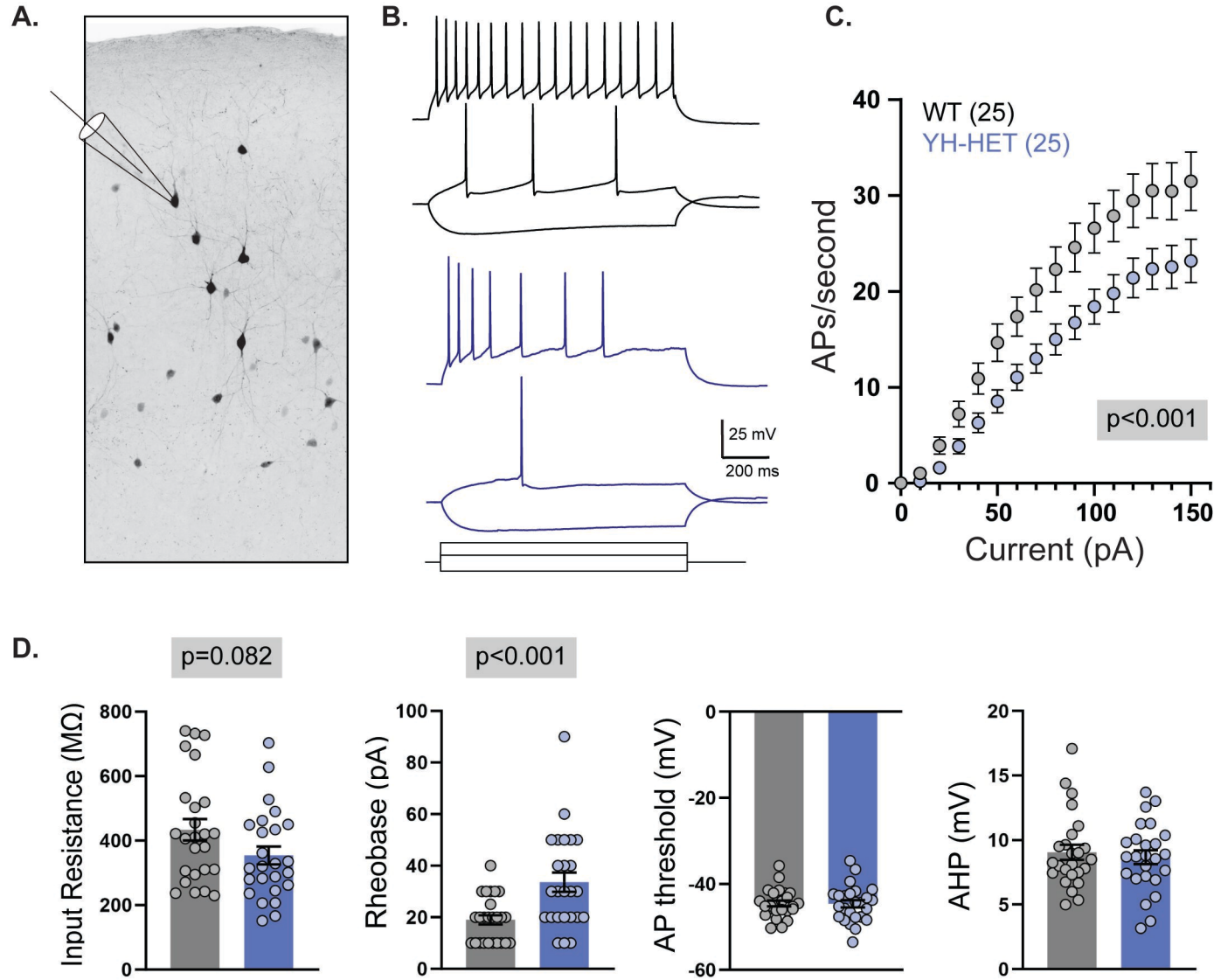

Supplemental Figure 2-1

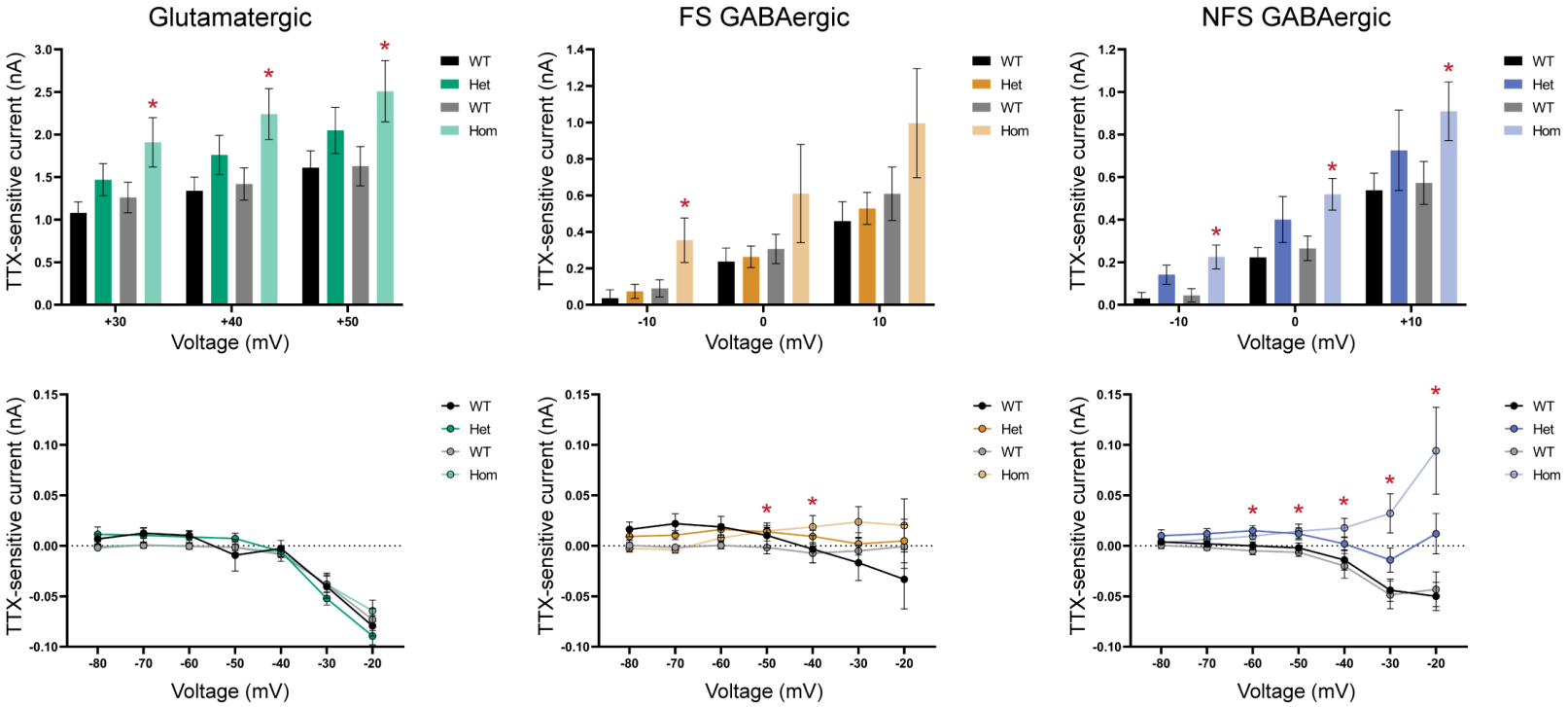

Supplemental Figure 4-1

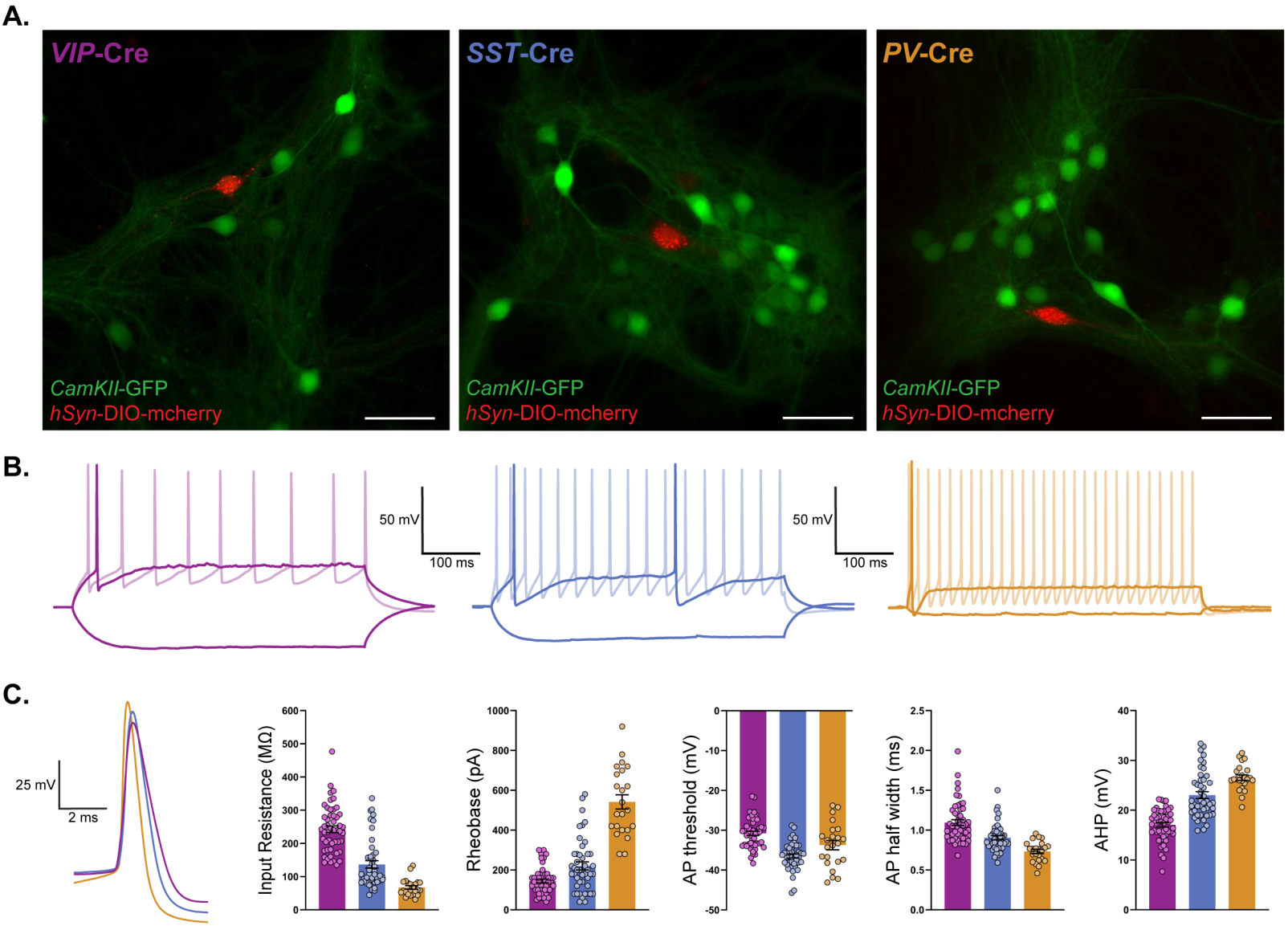

Supplemental Figure 4-2

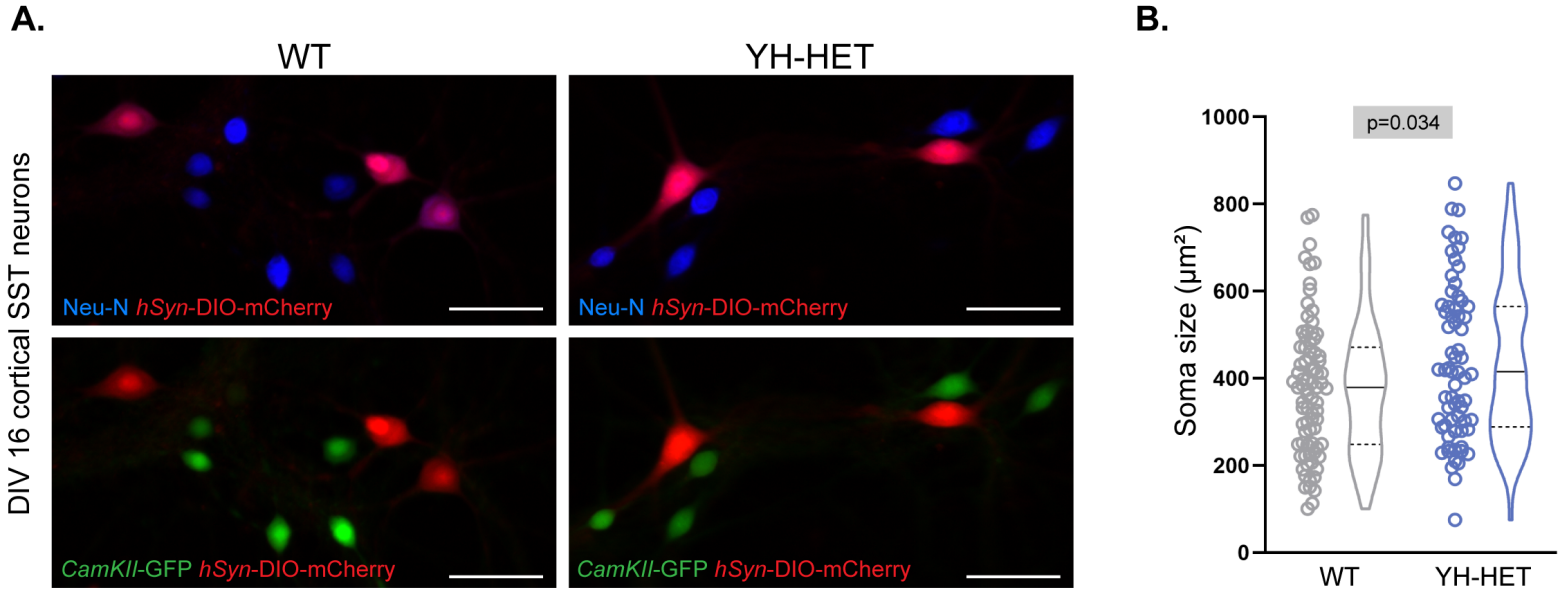

Supplemental Figure 4-3

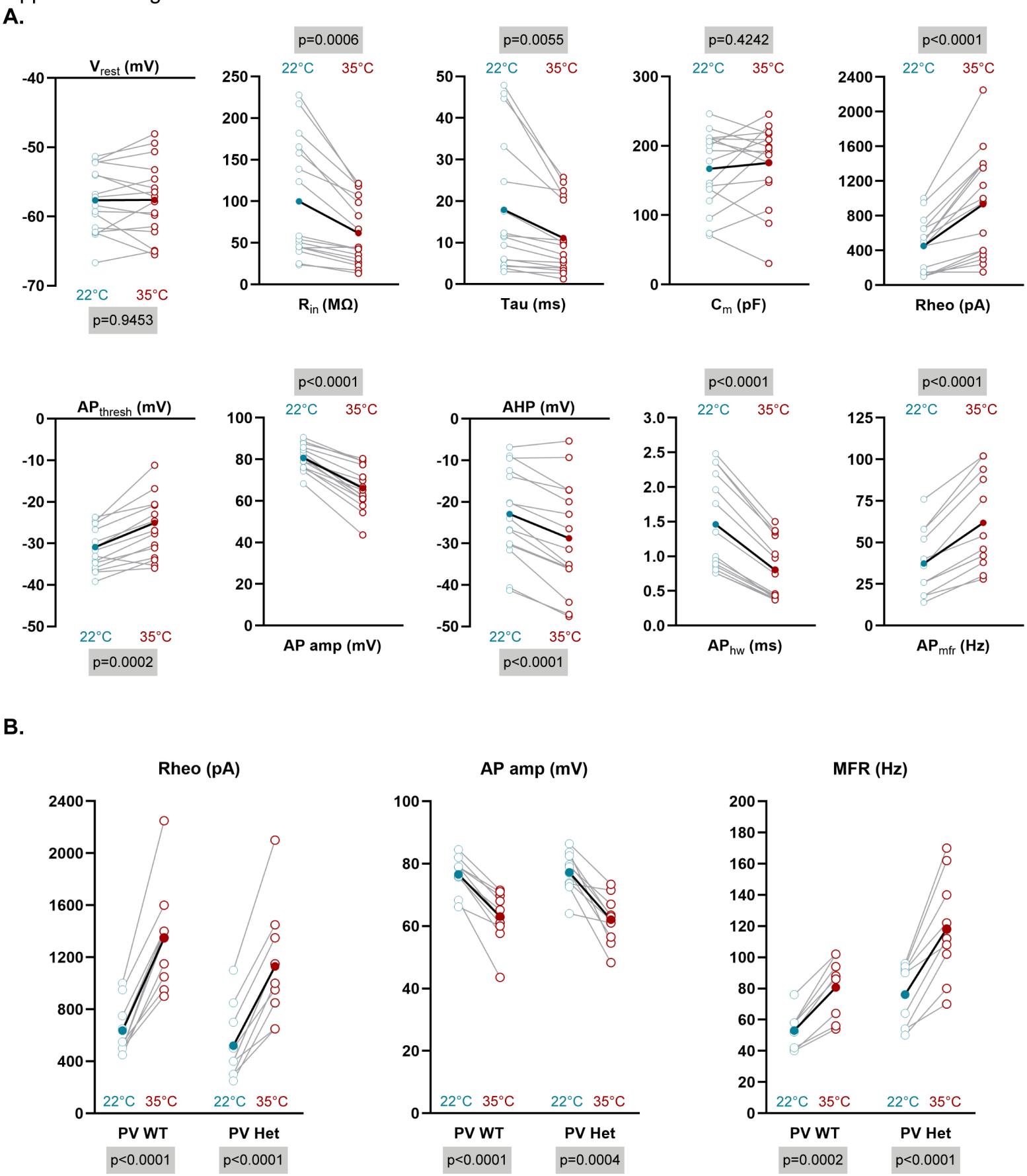

Supplemental Figure 5-1

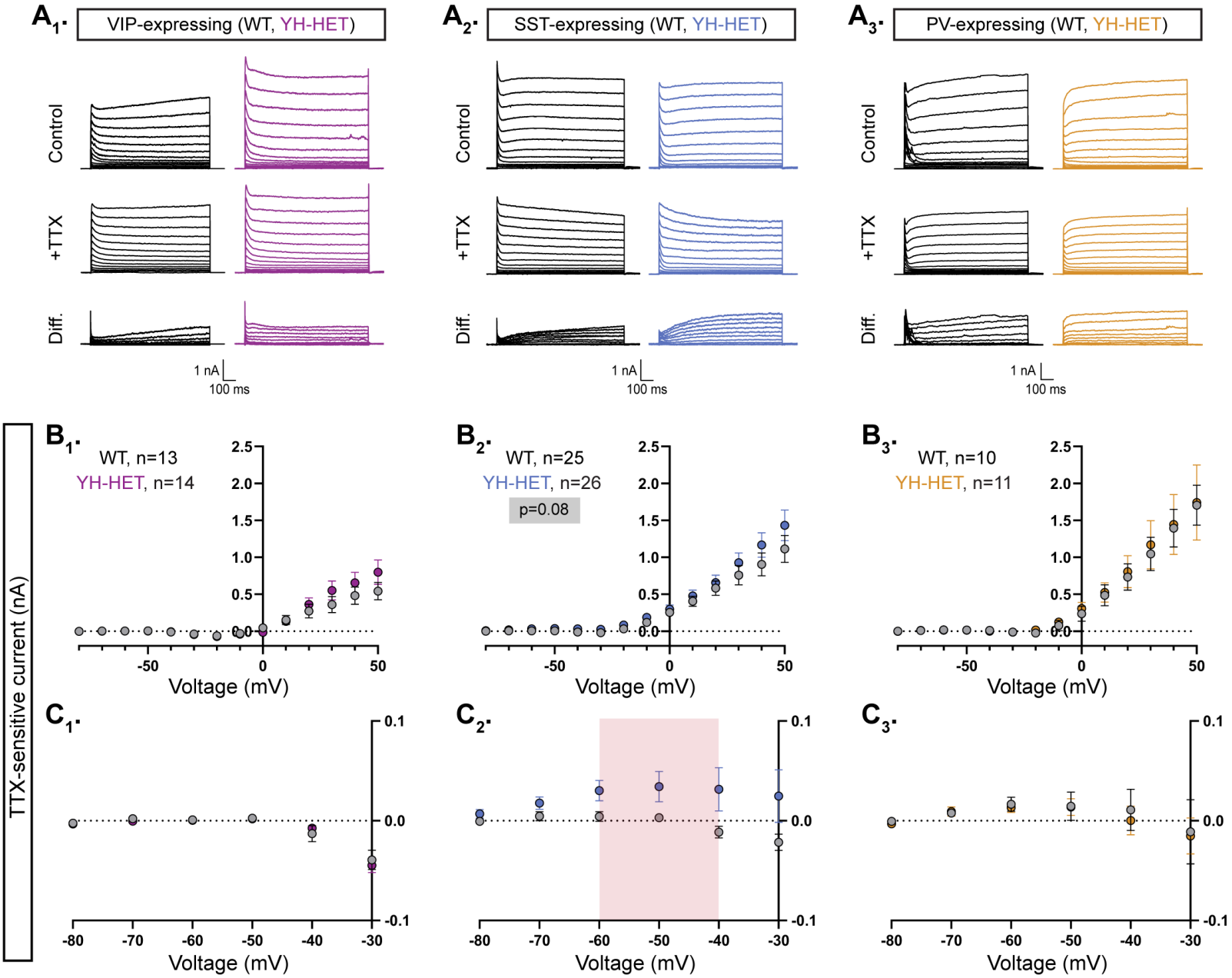

Supplemental Figure 5-2

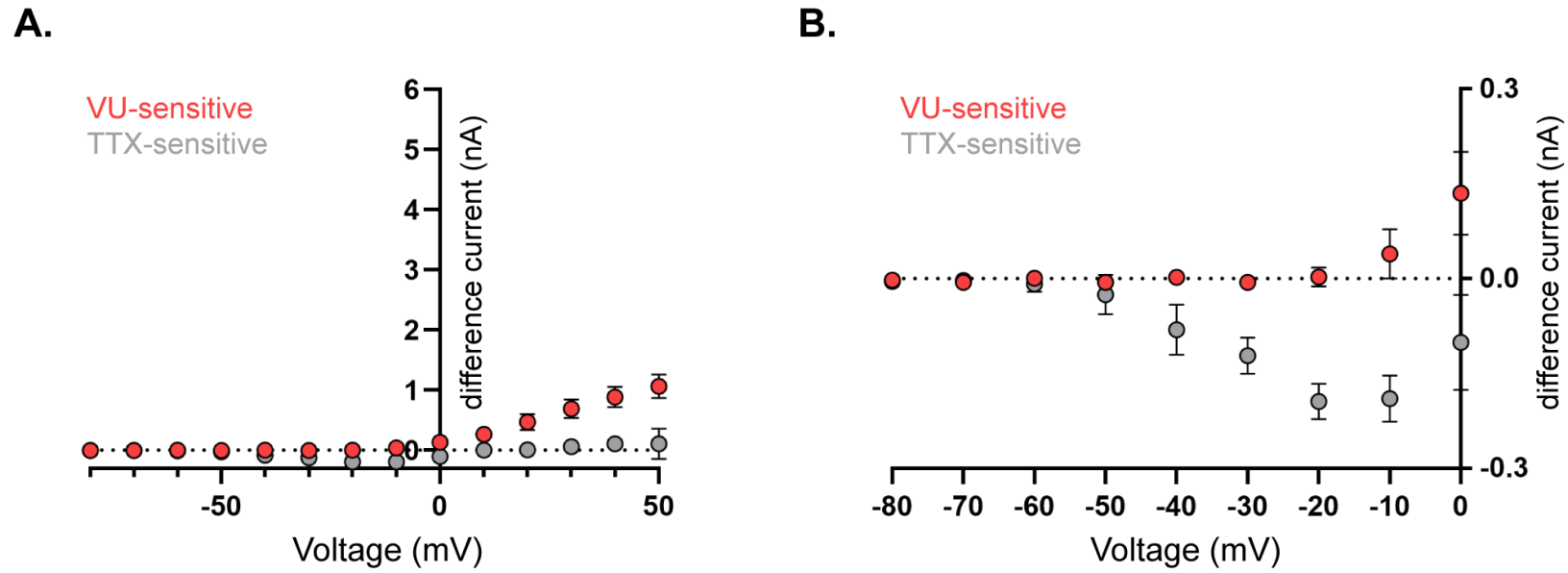

Supplemental Figure 6-1

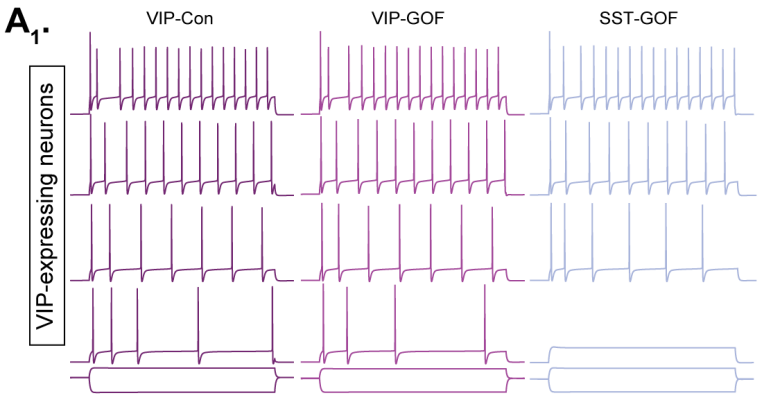

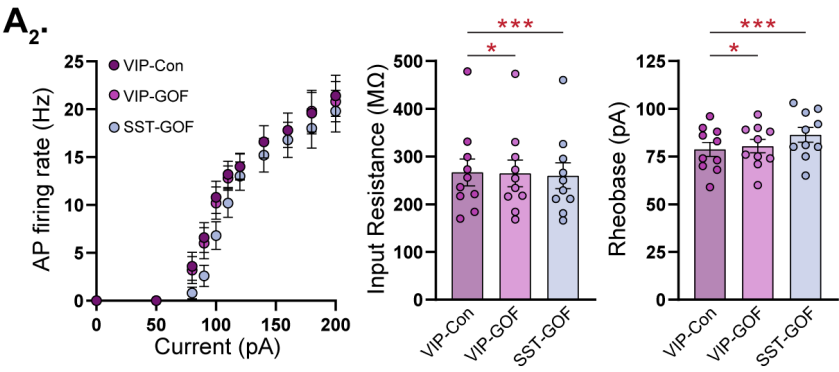

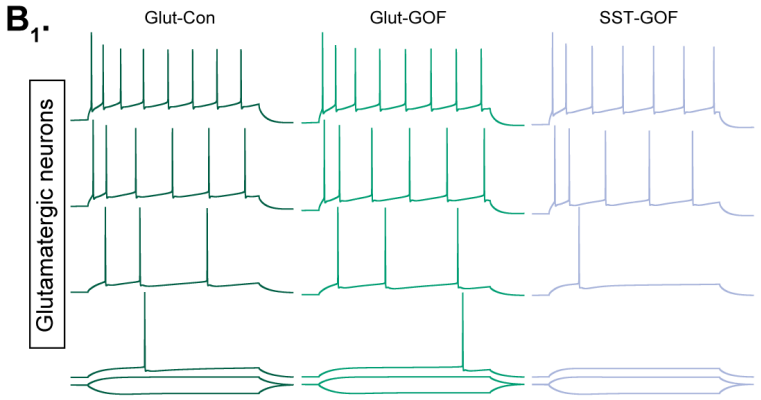

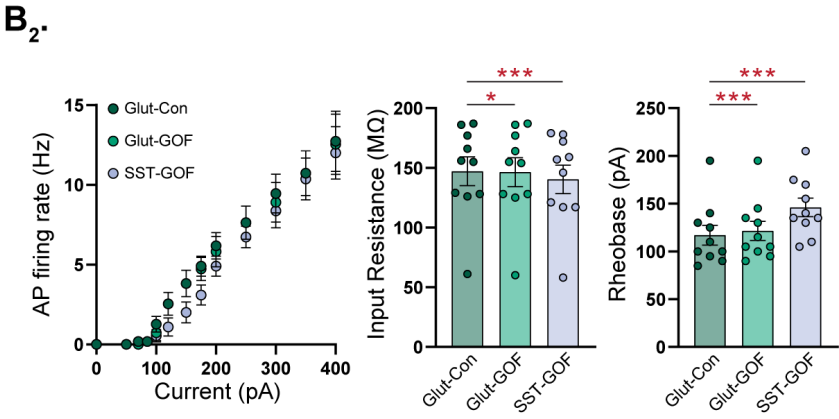

Supplemental Figure 6-2

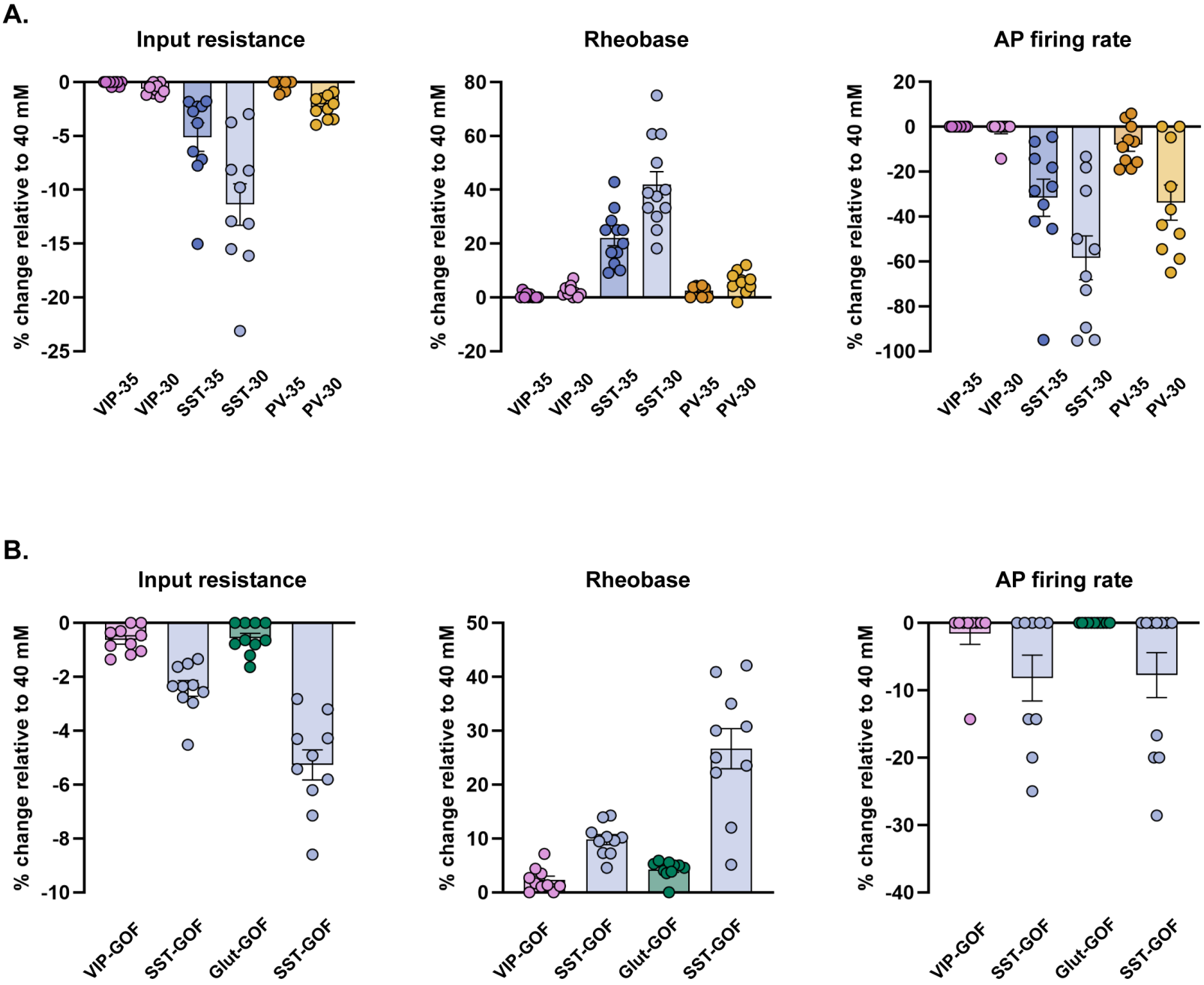

Supplemental Figure 7-1

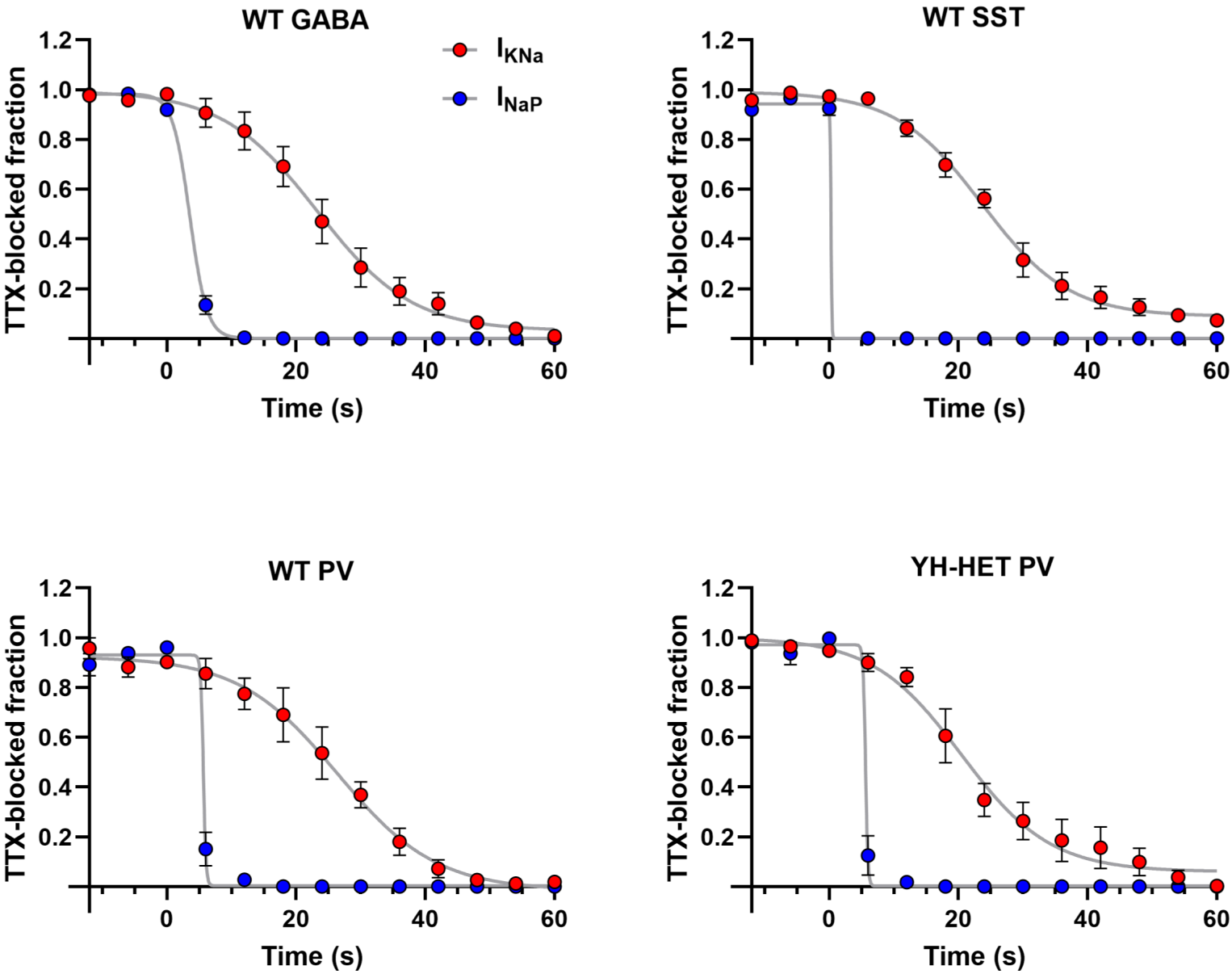
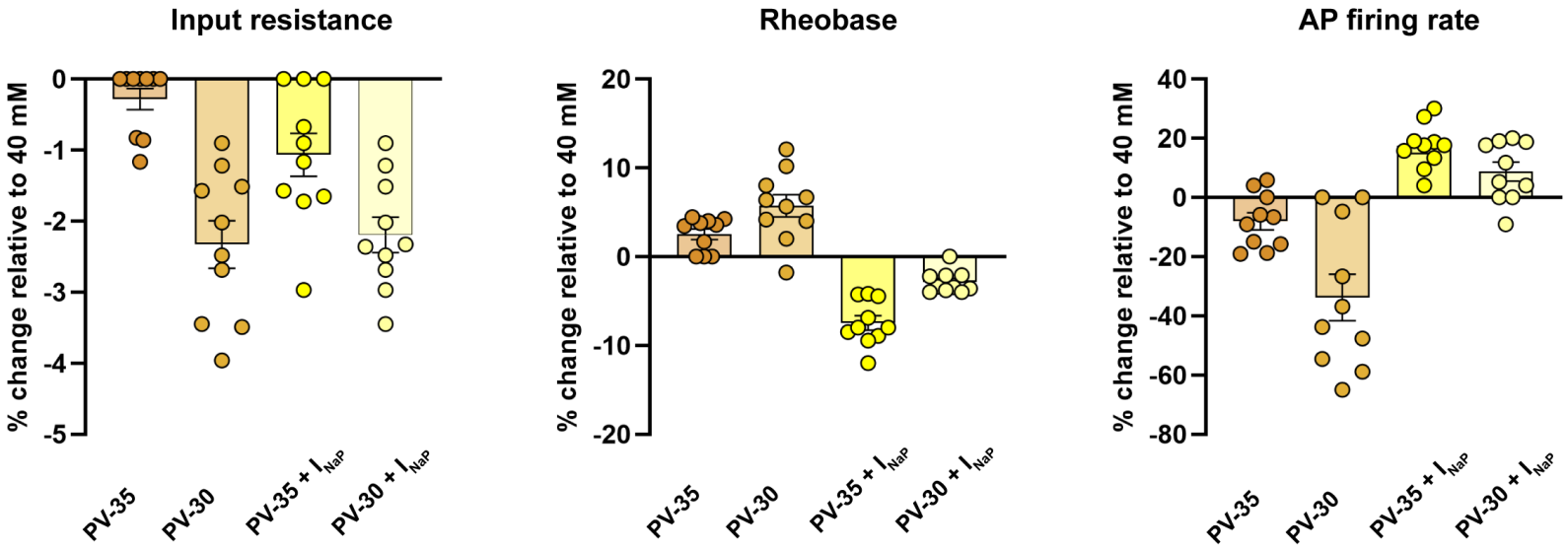
Supplemental Figure 7-2